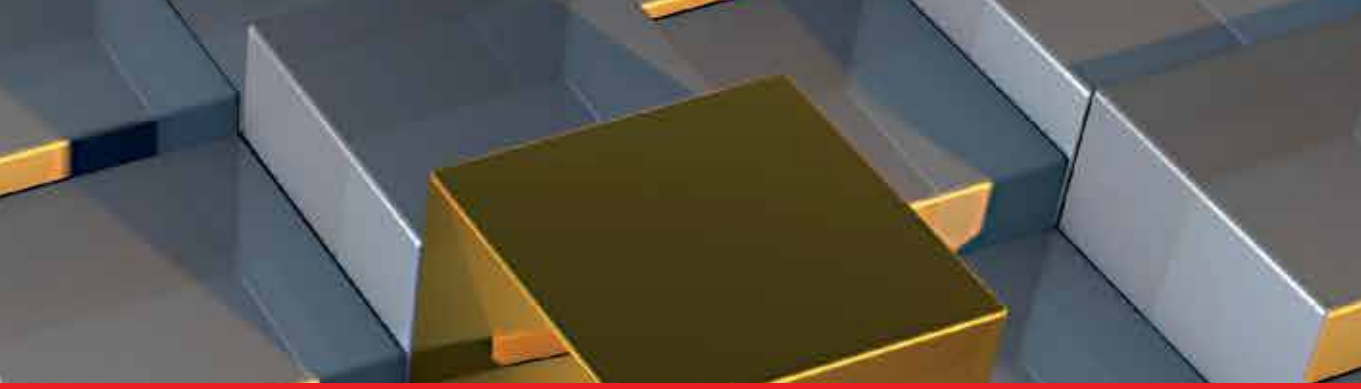

IntechOpen

Superalloys for Industry Applications

Edited by Sinem Cevik

SUPERALLOYS FOR INDUSTRY APPLICATIONS

Edited by **Sinem Cevik**

Superalloys for Industry Applications
http://dx.doi.org/10.5772/65570
Edited by Sinem Cevik

Contributors

Sgk Manikandan, M Kamaraj, D Sivakumar, Facundo Almeraya-Calderon, Manuel Alejandro Lira Martinez, Taboada Jorge, José Cabral, Patricia Zambrano-Robledo, Citlalli Gaona, Francisco Estupiñan, Yongbo Wu, Qiang Wang, Sisi Li, Dong Lu, Nageswara Rao Muktinutalapati, Arivazhagan Natarajan, Arivarasu M, Mohieddine Benghersallah, Sutter Guy, List Gautier, Lavinia Cosmina Ardelean, Lucien Reclaru, Cristina Maria Bortun, Brandusa Ghiban

Notice

First published in London, United Kingdom, 2018 by IntechOpen
eBook (PDF) Published by IntechOpen, 2019
IntechOpen is the global imprint of INTECHOPEN LIMITED, registered in England and Wales, registration number: 11086078, The Shard, 25th floor, 32 London Bridge Street
London, SE19SG – United Kingdom
Printed in Croatia

British Library Cataloguing-in-Publication Data
A catalogue record for this book is available from the British Library

Additional hard and PDF copies can be obtained from orders@intechopen.com

Superalloys for Industry Applications
Edited by Sinem Cevik

p. cm.

Print ISBN 978-1-78923-538-8

Online ISBN 978-1-78923-539-5

eBook (PDF) ISBN 978-1-83881-249-2

Meet the editor

Dr. Sinem Çevik is currently an assistant professor in Metallurgical and Materials Engineering at the Ondokuz Mayis University, Samsun, Turkey. She has a particular interest in the areas of superalloys, welding, solidification cracks, corrosion/oxidation of metals and their alloys, electrochemistry, ceramics, coatings, and thin films. Her PhD studies are related to the evaluation of HAZ microfissures of superalloys. Her MSc thesis on anodic reactions of tungsten was submitted in 2003. She graduated from the Department of Metallurgical and Materials Engineering, METU, Turkey, with a graduation thesis on different welding techniques. She performed research on piezoelectricity of materials at the Penn State University, USA, in 2004. She also joined the MEMS group at the University of the West of Scotland with a project on AlN piezoelectric thin films in 2008. At present, she has published 10 papers, 35 proceedings, and 3 book chapters. She also worked on different international and national projects.

Contents

Preface

Innovations in the aerospace and aircraft industry have thrown light on building the future's engineering architecture in today's globalized world, where technology is an indispensable part of our lives. On the basis of the aviation sector, innovations in the materials used in aircraft parts have to be continuously maintained its actuality. At this point, superalloys have been proceeding in the way to become a material that aerospace and defense industries never replace of any other material when combining its good mechanical properties, easy machinability, and low cost. In spite of their superior properties, these materials suffer from wear, tear, and crack in order to be exposed to the elevated working temperatures and the harsh operating environments in service.

In Within the scope of this book, the superalloys usually used in gas turbine engine parts are reviewed. Improvements of materials used in aircraft gas turbine engines, which constitute 50% of total aircraft weight, must be protected continuously. The utilization of superalloys in the aerospace and defense industries cannot be ignored because of their excellent corrosion and oxidation resistance, high strength, and long creep life at elevated temperatures.

This book provides information on the interaction between the microstructure of alloys and their mechanical properties and also the position of superalloys in the manufacturing industry. Topics cover the minimization of the formation of microsegregation and detrimental phases in the GTA welding of superalloys, oxidation kinetics of nickel-based superalloys used in the manufacture of rings for aircraft engines, a review of the work done over the last two decades to understand the hot corrosion behavior of superalloys used in advanced coal-based power plants, ultrasonic-assisted machining of Inconel 718, dry high-speed turning of Ti-6Al-4V titanium alloy, and laser welding in dentistry.

This book serves as a guide to those interested in superalloys and materials, their properties, techniques of manufacturing, application areas, and so on. Thus, the engineers in the industry, the students in colleges and universities, and the lecturers giving courses at both undergraduate and postgraduate levels can use this book as an international reference.

The book "Superalloys for Industry Applications" consists of contributions by scientists and engineers who are experienced in the production, design, and analysis of materials from all around the world. We hope that this book will be an irreplaceable source of study for manufacturing, degradation mechanisms, and reliability of superalloys.

Sinem Çevik
Ondokuz Mayis University, Turkey

Chapter 1

Laves Phase in Alloy 718 Fusion Zone

S.G.K. Manikandan, D. Sivakumar and M. Kamaraj

Additional information is available at the end of the chapter

http://dx.doi.org/10.5772/intechopen.70325

Abstract

The gas tungsten arc (GTA) welded fusion zone of alloy 718 has been well investigated on the formation of interdendritic Laves phase. This article deals with the various process control methodologies for minimizing the microsegregation and Laves phase such as the enhanced weld cooling rate in GTA welding (GTAW) process and modification in weld metal chemistry. Even though the high energy density welding processes such as electron beam (EB) and laser beam (LB) welding techniques are proven in minimizing the microsegregation and Laves phase, the requirement of conventional GTA welding process still exists in the aerospace industry due to the complex shapes of the components and the inaccessible conditions for executing the welding process. The enhancement in the weld cooling rate and modified weld metal chemistry resulted in the refined fusion zone microstructure and reduced microsegregation. Enhanced weld efficiency on ultimate tensile strength (UTS) and 0.2% YS at 25°C was observed to the tune of 85 to 93% by employing cryogenic cooling in GTA welding process. Similar improvement in weld efficiency at 650°C was observed. However, the evaluated weld efficiencies with cryogenically cooled weld metal were marginally lower than the previous works in EB and LB welds only by 2–3%.

Keywords: Laves phase, alloy 718, GTAW, X-ray diffraction, tensile strength, microsegregation

1. Introduction

Alloy 718 is extensively used in the high-temperature systems of cryogenic rocket engines in Indian launch vehicles. Use of Nb as age hardener in place of Al or Ti in alloy 718 eliminated the problem of strain age cracking, but resulted in the formation of brittle interconnected Laves phase during welding [1] which are the favorable sites for easy crack

initiation and propagation. This affects the aging response, tensile properties, and ductility of the welded components [2]. Hence control on the morphology and continuity of the Laves phase during solidification was found to be essential. Published information on the control of Laves phase formation in alloy 718 welds is limited to autogenous welds of gas tungsten arc welding (GTAW), electron beam welding (EBW) and laser beam welding (LBW) [3], current pulsing with simple square waveform and magnetic arc oscillation in GTAW [4]. It was concluded that the faster cooling rate reduced the level of interdendritic Nb segregation and amount of Laves phase. But high energy density processes cannot be adopted in rocket engines due to the complex shapes and highly inaccessible areas. Zhang and Liu reported that the cooling rate was enhanced with the higher growth rate and steep temperature gradient [5]. Hence pulse current manual GTA welding process is relied upon with limited options such as modified pulse waveform [6] and helium shielding gas to enhance the cooling rate and minimize the segregation. Their effect on formation of Laves phase and microsegregation of niobium in alloy 718 fusion zone has been discussed.

The influence of cryogenic coolants on microstructures was investigated earlier [6, 7]. Hence rapid heat dissipation dynamics using liquid nitrogen was studied in the present work during manual GTA welding process for further enhancing the weld cooling rate. Filler metals with significantly different compositions from that of the base material composition were used to minimize Laves phase in some of the welding applications [8]. This was the driving force for studying the solidification behavior of alloy 718 fusion zone welded with high Mo (16 wt%) filler metal, even though it was well established by various researchers [9, 10]. The present study also describes the influence of hybrid pulsing in the range of 500–2000 Hz on the fusion zone microstructure and interdendritic segregation of alloy 718 welds. The effects of pulse frequency have been analyzed through solidification parameters and related mechanisms on the interdendritic segregation in alloy 718 fusion zone. In view of the above, an attempt has been made in the present study to evaluate the effectiveness of cooling techniques in controlling the formation of Laves phase and the high-temperature mechanical properties in alloy 718 GTA welds.

Primarily, this chapter deals with the control of laves phase formation in the fusion zones of alloy 718 weldments by enhanced weld cooling rate through modified pulse current waveform and shielding gases (Argon and Helium) in GTA welding process and change of weld metal chemistry using solid solution (FM1) and matching composition/age-hardenable (FM2) filler metal. Secondly, the mechanical properties at room temperature and elevated temperatures have been correlated to the Laves phase in the weld fusion zone of alloy 718.

2. Materials and methods

The specimens were prepared from alloy 718 sheets of 2 mm thick (for welding experiments) and 3 mm (for solidification experiments) in 980°C solution treated condition using gas tungsten arc welding process. The solidification experiments were conducted in autogenous mode GTAW with thermocouples welded at the center of the weld and adjacent to the fusion zone in a 5 × 5 array in order to obtain both longitudinal and transverse temperature distribution. The details of the chemical composition for base material and filler metal are given in **Table 1**. The weld

Element	C	Mn	Si	Cr	Fe	Mo	Nb + Ta	Ti	Al	Cu	Ni
Base metal	0.05	0.11	0.1	18.2	19.8	2.8	5	1	0.6	0.03	Bal.
FM1	0.05	2	0.5	16	5	16	-	-	-	-	Bal.
FM2	0.08	0.55	0.4	21	16	3.3	5.5	1.15	0.8	0.3	Bal.

Table 1. Chemical composition of base metal and filler metals (in wt%).

parameters for square butt joints with an optimized heat input value of 0.75–0.77 kJ/mm were employed. The conventional copper heat sink and liquid nitrogen were used for the external cooling. Similarly, modified pulse wave form (constant current, compound current, and hybrid pulsing) with argon and helium shielding gas were employed for the in-process cooling.

Welded samples were subjected to the aging treatment as per AMS 5596 K after 100% X-ray radiography and dye penetrant test. The samples were etched using Kalling's reagent and the weld microstructures and elemental mapping were obtained with field emission gun scanning electron microscope (FE-SEM) with an acceleration voltage of 20 kV. The elemental mapping of Nb in the dendritic and interdendritic zones was carried out in a thermal field emission electron microprobe (EPM JXA-8530F) over the metallographically prepared and unetched specimens with an acceleration voltage of 15 kV.

Electron diffraction studies were carried out with 3 mm diameter and 90 μm thickness discs of the as-welded and the direct-aged fusion zone using Jeol make transmission electron microscope (TEM) equipment. Differential thermal analysis was conducted to finalize the heating rate among the three heating rates of 5, 10, and 20°C/min using SII 6300 EXSTAR with a sample weight of 0.02 ± 0.0005 g in an argon atmosphere at a flow rate of 0.2 l/min. Differential scanning calorimetric analysis was performed on a SETARAM LABSYS 1600 heat flux type DSC instrument to measure eutectic type reaction temperatures with an optimized heating rate of 10°C/min and a cooling rate of 20°C/min. The tensile test of the specimen at 25 and 650°C were conducted at a strain rate of 1×10^{-3} s^{-1} as per ASTM E8 and E21-09, respectively. An air circulating furnace with accuracy in temperature of ±3°C was used for conducting the 650°C tensile test. The fracture morphology was studied using scanning electron microscope.

3. Microstructural characterization of fusion zone

The conventionally cooled GTA welded fusion zone microstructure using argon shielded constant current technique (weld cooling rate: 40°C/s) revealed a mixed dendritic structure consisting of columnar and/or elongated dendritic and equiaxed dendritic structures as shown in **Figure 1(a)**. The fusion zone exhibited coarse columnar dendrites from the fusion line to the middle of the fusion zone due to the experimentally measured longitudinal temperature gradient in the order of −39.26°C/mm along the welding direction.

But the fusion zone of compound current pulse with conventional cooling measured a weld cooling rate of 394°C/s, the corresponding fusion zone exhibited a finer equiaxed dendritic structure as shown in **Figure 1(c)**. The transition from columnar-to-equiaxed (CET) was

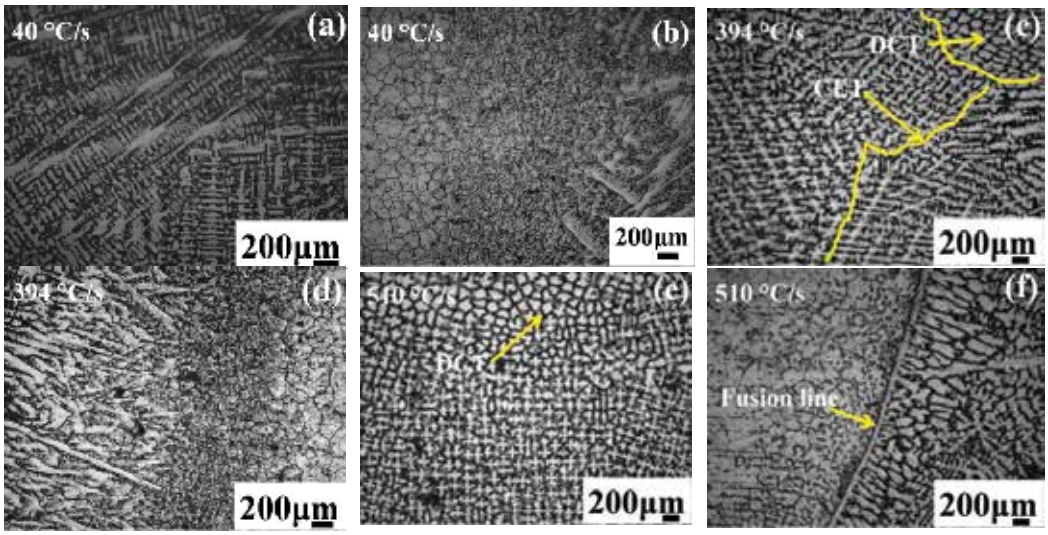

Figure 1. Micrographs of conventionally cooled fusion zones (a, c), heat affected zones (b, d) and cryogenically cooled fusion zone (e), heat affected zone (f) using constant current (40°C/s) and compound current pulse technique (394, 510°C/s), respectively.

shifted away from the center of the fusion zone by the enhanced longitudinal temperature gradient existed ahead of the columnar front of the order of −195.16°C/mm. The base material grains were recrystallized and epitaxial growth was initiated with finer grains which led to the formation of fine columnar dendritic structure near to the heat affected zone as evidenced in **Figure 1(d)**.

Similar observations were made on the microstructures of the cryogenically cooled (liquid nitrogen) GTA welded fusion zone with finer equiaxed dendritic structures than that of the conventional cooling method as shown in **Figure 1(e)** for the same set of welding variables (as used for the weld cooling rate of 394°C/s). The refinement of fusion zone microstructure was due to the imposed cooling rate. The extent of refinement of the fusion zone microstructure was also enhanced till the middle of the fusion zone. Certain regions in the middle of the fusion zone revealed the dendrite to cellular transition as shown in **Figure 1(e)** by the degeneration of side branches through dendrite arm remelting mechanism due to the variation in the morphology parameter (temperature gradient/growth rate—G/R). As presented in **Figures 1(b)**, **(d)**, and (f), and **2(e)** and **(f)**, microfissures were not observed in the heat affected zone of both the conventionally cooled and liquid nitrogen-cooled weldments. The base material grains were coarsened in the lowest weld cooling rate (40°C/s). The grain growth was limited with the enhanced cooling rate as shown in **Figure 2(f)**, especially in the liquid nitrogen-cooled weldments through the reduced transverse temperature gradient by the impingement of cold nitrogen vapor.

The SE micrographs of conventionally cooled fusion zone exhibited a thick and continuous interdendritic Laves network as shown in **Figure 2(a)** due to the increased time at temperature parameter and reduced longitudinal temperature gradient (−39.26°C/mm) which led to a

http://dx.doi.org/10.5772/intechopen.70325

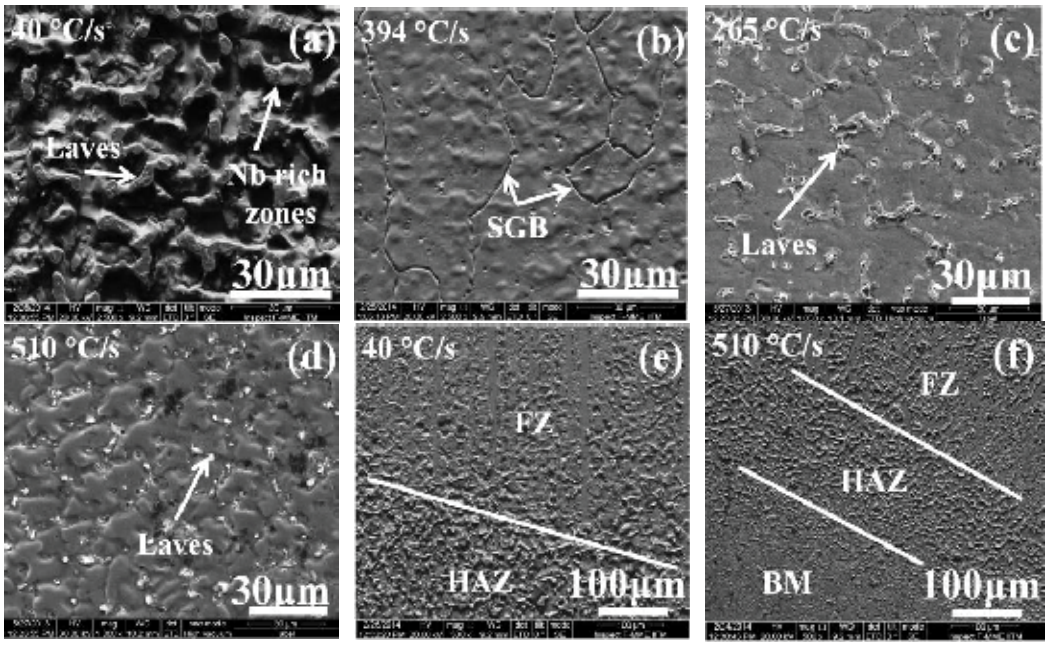

Figure 2. SE micrographs of (a, b) conventionally cooled, (c, d) liquid nitrogen-cooled GTA welded fusion zone and (e, f) respective heat affected zone.

lower weld cooling rate (40°C/s) and higher solidification time resulted an enhanced microsegregation. **Figure 3** details about the quantitative elemental analyses of GTA weld fusion zone for the six weld cooling rates (40, 80, 394, 265, 362, and 510°C/s).

The quantitative elemental analysis exhibited that microsegregation was reduced with increased weld cooling rate. This was revealed by the increase of niobium content in the dendritic regions of both the FM1 and FM2 fusion zone with the weld cooling rate. As shown in **Figure 2(a)**, the Nb rich zones present in the FM2 fusion zone (40°C/s) exhibited relatively higher niobium content in the dendritic region due to the pickup from the adjacent zones. As the iron content increased in the dendrite, more of niobium was rejected into the interdendritic regions due to the limited solubility of Nb which resulted in the increased microsegregation [8]. The fusion zone (394°C/s) microstructure consisted of γ-matrix with clear solidification grain boundaries and discrete Laves particles in the interdendritic regions as in **Figure 2(b)**.

The microsegregation was significantly reduced by employing the in-process cooling method such as compound current pulse and helium shielding gas which enhanced the longitudinal temperature gradient and growth rate. Thus the fusion zone microstructure was refined. The liquid nitrogen-cooled fusion zone microstructures for the constant current (265°C/s) mode revealed finer and disconnected interdendritic Laves particles as shown in **Figure 2(c)**. As the weld cooling rate was increased to 510°C/s by employing the compound current pulse mode, the microstructure of the fusion zone was further refined and resulted with relatively finer Laves particles as shown in **Figure 2(d)**. Since the interdendritic microsegregation was

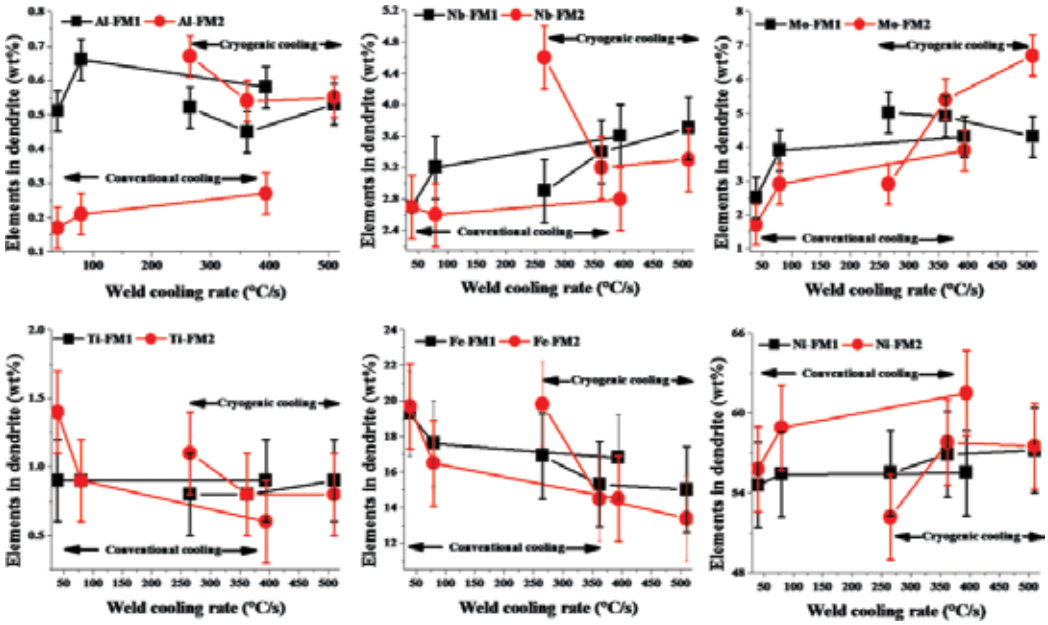

Figure 3. Elemental analysis of alloy 718 fusion zone using FE-SEM/EDS.

reduced, the dendrite was enriched with niobium for the higher weld cooling rates. It was observed that Nb concentration in FM2 fusion zone was comparable to the base material composition at higher weld cooling rate (510°C/s). As the iron content was decreasing (k_{Fe} =0.98 to 0.76 for FM1 and k_{Fe} = 1 to 0.63 for FM2) with the increase in weld cooling rate as given in **Figure 3** which aided in reducing the microsegregation. In addition, an increase in nickel content at higher weld cooling rate (510°C/s) was observed. This helped in retaining the Nb content in the matrix and thereby the concentration of Nb in the dendritic regions was increased.

As discussed previously, the decrease of iron content in the dendrite core with the increased weld cooling rate indicated that the weld dilution levels were reduced for the maximum cooling rate employed in the present study. The present study took advantage of the modified pulse waveform and the helium shielding gas which aided in constricting the arc; thereby, the weld dilution levels were minimized in the present study. Hence the solubility of niobium and molybdenum were increased because of the reduced iron content in γ matrix and the resultant interdendritic segregation was also reduced. In our present study, the distribution trend of elements in the fusion zone was comparable with the previous research work [8]. However, the localized niobium rich zones in FM2 fusion zone modified the elemental distribution trend of niobium at lowest weld cooling rate. The HAZ of both the weldments were free from microfissures and grain boundary liquation as shown in **Figure 2(e)** and **(f)** due to the balanced transverse temperature gradient because of the longitudinal holes on the top of the cooling system with an angle of attack for cooling the HAZ region. The interdendritic phases in the fusion zone were found to be of C14 type Laves phases with hcp crystal structure (a = 0.4831 nm, c = 0.7881 nm) as shown in **Figure 4(a)**. The matrix was found to be

http://dx.doi.org/10.5772/intechopen.70325

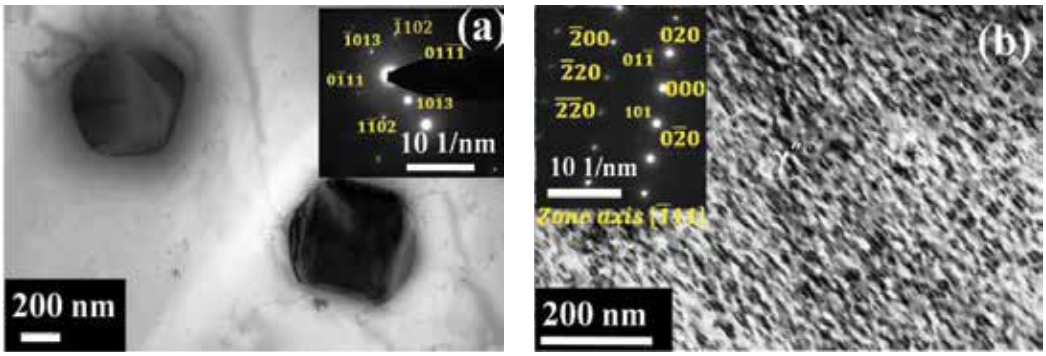

Figure 4. TEM bright field image with SADP pattern of (a) Laves phase in as-welded fusion zone, TEM dark field micrograph of direct-aged fusion zone (b) γ″ precipitates with zone axis [−1 1 1].

polycrystalline in nature with face centered cubic crystal structure (a = 0.3571 nm) for the fusion zone of higher weld cooling rates (394°C/s and above).

The aging response was also confirmed by the TEM dark field images. The respective selected area diffraction pattern is shown in **Figure 4(b)**. Disc-shaped γ″ precipitates and spherical γ′ precipitates were observed. The Laves phase morphology and its crystal structure were not affected by the imposed thermal gradient and enhanced weld cooling rate. The script type morphology of the Laves particles was retained for the employed weld cooling rates.

The partition ratio of the individual elements was calculated from the FE-SEM/EDS data using dendrite microsegregation model. The partition coefficient of niobium in the FM1 fusion zone was increased from 0.54 to 0.72 in the conventionally cooled fusion zone. This could be due to the decrease in iron and chromium contents (**Figure 3**). However, the partition ratio of niobium (0.54–0.97) in the FM2 fusion zone was found to be more than that of the FM1 fusion zone. The fusion zones of lower weld cooling rates exhibited higher Laves phases because of the huge segregation of niobium and molybdenum (k_{Nb} = 0.54) toward liquid. Obviously, a steep concentration gradient was built in the interdendritic liquid by the lower diffusivity and/or mobility parameter of molybdenum through solutal undercooling. This led to a better refinement in microstructure. The BSE micrograph of the liquid nitrogen-cooled FM2 fusion zone revealed the reduced interdendritic segregation as shown in **Figure 5(a)**. The elemental mapping also confirmed the reduced microsegregation of niobium as shown in **Figure 5(b)**. The finer distribution of Laves particles aided in improving the mechanical properties of the liquid nitrogen cooled weldment. However, the characteristic temperatures in DSC analysis were not affected significantly for the liquid nitrogen-cooled FM1 fusion zone from that of the conventionally cooled alloy 718 fusion zone.

In the present study, liquidus temperature (primary γ) of the FM1 fusion zone was not significantly changing from that of the base material for the lower weld cooling rates of 40–362°C/s. But a significant increase in liquidus temperature was observed with the higher employed cooling rates of 394 and 5107°C/s due to the enhanced molybdenum content in the matrix at these cooling rates as shown in **Figure 3**. The partitioning of higher melting point solute (Mo) to γ matrix led to the increase in the solvus temperature of γ matrix. Whereas the liquidus

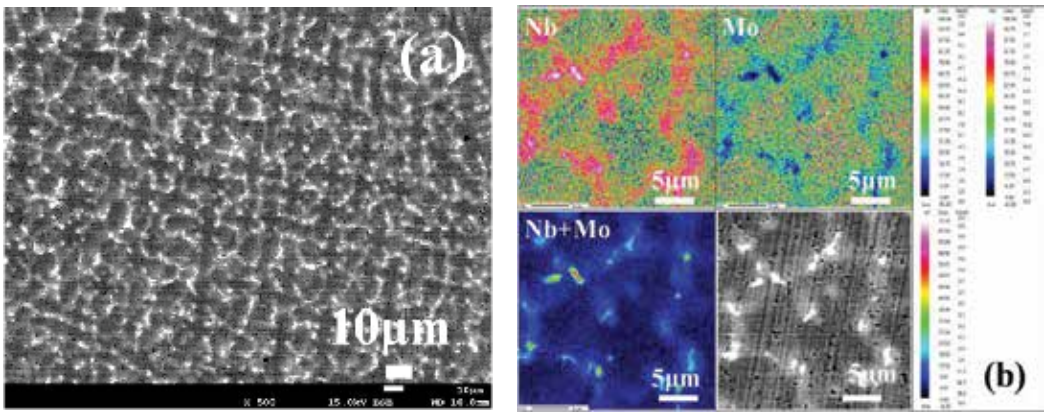

Figure 5. BSE image of FM2 fusion zone for a weld cooling rate of (a) 510°C/s and (b) elemental mapping in EPMA.

temperature of FM2 fusion zone was decreasing as the cooling rate was increased due to the increased solute concentration in the matrix as per the phase diagram, at higher cooling rates, the liquidus temperature of FM2 fusion was comparable to that of the base material. The solidification time for each employed weld cooling rate was calculated using heat transfer experiments and DSC analysis and found reduced from 2.099 to 0.12 s for the enhanced weld cooling rate from 40 to 394°C/s. This was further reduced to 0.011 s for the liquid nitrogen cooling method. The SE micrographs of the fusion zones of hybrid pulsing using argon and helium shielding gases are shown in **Figure 6(a)–(f)**. In the present study, the modified

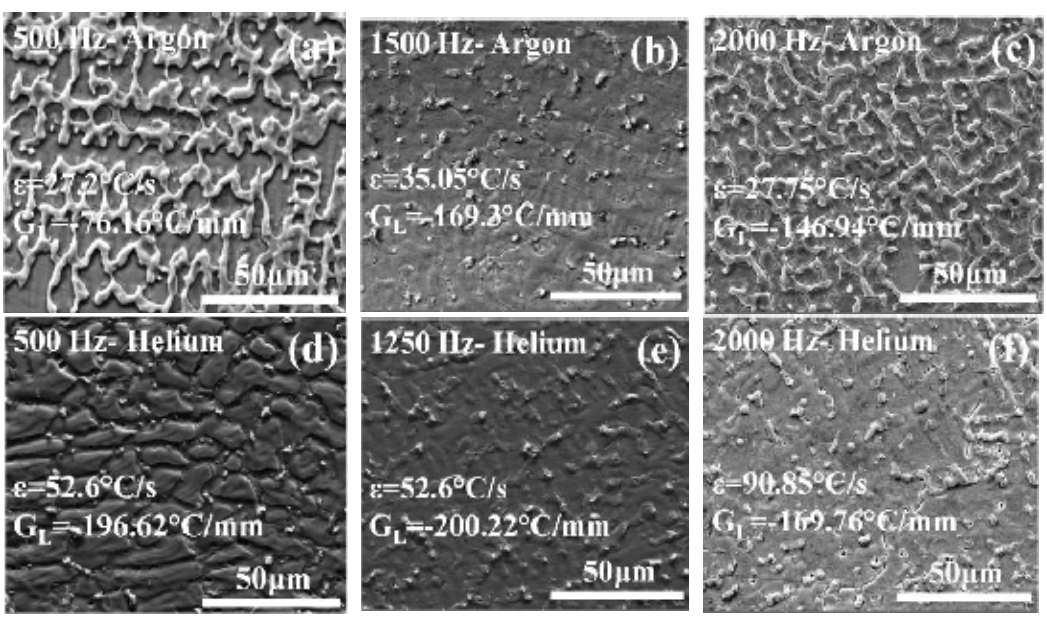

Figure 6. SE micrographs of (a–c) argon and (d–f) helium shielded as-welded fusion zone using hybrid pulse current.

http://dx.doi.org/10.5772/intechopen.70325

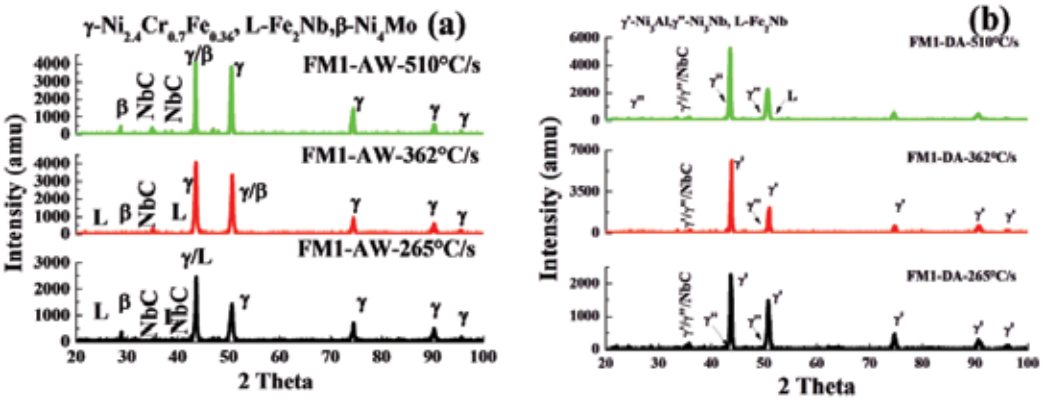

Figure 7. X-ray diffraction patterns of the fusion zone of three different weld cooling rates with FM1 in (a) as-welded and (b) direct-aged conditions.

pulsing increased plasma momentum and electro-magnetic force inside the weld pool and led to the refined microstructure. Thus, the interdendritic Laves phase was reduced.

The fluctuation in radiation had been reduced in the pulse frequency range of 500–2000 Hz and therefore the heat transfer efficiency of the arc was improved. The increased plasma momentum enhanced the arc pressure. In addition, the lower pulse ratio was resulted by the subdivision of peak pulse time with superimposed high frequency pulsing. The combination of the above phenomenon was giving rise to the convective flow. This aided in the equiaxed growth ahead of columnar growth. However, the fluctuations induced by the pulsing current alone were not aiding the fragmentation of dendrites in mushy zone. The solute enrichment at the dendrite root caused the dendrite remelting. Hence, the finer secondary dendritic arms were fractured and/or fragmented easily and further aided by the stirring action and/or by viscous friction caused by the relative movement between liquid and solid metal.

The phases formed in the fusion zone were analyzed using the representative X-ray diffractograms as shown in **Figure 7(a)** and **(b)**. The diffraction peaks indicated the presence of γ matrix, MC type carbides, and Laves phase in the as-welded condition for both the FM1 and FM2 fusion zones. The lattice parameter of γ matrix was calculated using Nelson-Riley method and found an increased lattice constant (0.36113 nm) for FM1 fusion zone due to the increased solute (Mo) content in the dendrite. In addition, FM1 fusion zone exhibited β-Ni4Mo phase in the as-welded condition and got dissolved after direct aging treatment as shown in **Figure 7(a)** and **(b)**. The direct-aged specimens of fusion zone showed the diffraction peaks of γ″/γ′ precipitates, MC type carbides, and Laves phase.

4. Mechanical property characterization of weldments

The hardness distribution in the weld metal was executed through microhardness survey. The experimental conditions are as follows:

- Condition: As welded, Duration: 15 s, Load: 2.942 N.
- Condition: Direct aged, Duration: 15 s, Load: 9.807 N.

The microhardness survey on the welded samples is given in **Table 2**. As inferred from the microhardness survey, the liquid nitrogen cooling method produced softer weldments than that of the conventionally cooling method.

The increased microsegregation and the existence of Laves phases led to the increased hardness in the as-welded condition for the conventionally cooled weld metal. The upper limit of the hardness values for the as-welded and direct-aged conditions mentioned in **Table 2** was corresponding to the lower and higher weld cooling rates, respectively. Moreover, the liquid nitrogen-cooled FM1 (solid solution filler metal) fusion zone well responded for the direct aging process as the fusion zone hardness values were comparable with FM2 (age hardenable filler metal) fusion zone. The results of room temperature (25°C) and high-temperature (650°C) tensile tests conducted on the welded specimen with six levels of weld cooling rate are given in **Figure 8(a)** and **(b)** for the conventional and liquid nitrogen cooling methods.

The room temperature tensile test data revealed that the weld strength properties in direct-aged condition were improved with CCP technique than that of the previous works on the same alloy system [1, 3]. The room temperature ultimate tensile strength (UTS) of the conventionally cooled weldment increased with the enhanced weld cooling rate for both the FM1 (987–1105 MPa) and FM2 (1256–1284 MPa).

The UTS values of conventionally cooled FM1 fusion zone was less than that of the FM2 fusion zone after direct aging at both 25 and 650°C. However, the tensile strength of welds was improved for the weldments cooled with liquid nitrogen. The high-temperature strength values were increased with the enhanced weld cooling rate. The UTS of liquid nitrogen-cooled FM1 fusion zone (1038 MPa) was higher than that of the FM2 fusion zone (1005 MPa) for the same weld cooling rate (510°C/s). This could be due to the reduced grain growth by the retention of molybdenum in the dendrite [11]. The microstructures were refined in FM1

Cooling method	Filler metal	Hardness of fusion zone (Hv)	
		As welded	Direct aged
Conventional	FM1	205–365	363–418
	FM2	238–406	410–454
Liquid nitrogen cooling	FM1	221–269	310–475
	FM2	204–237	309–475
Hybrid pulsing	FM1-Argon	250–375	350–415
	FM1-Helium	260–380	375–418
	FM2-Argon	230–250	330–440
	FM2-Helium	210–280	350–438

Table 2. Hardness of fusion zone.

http://dx.doi.org/10.5772/intechopen.70325

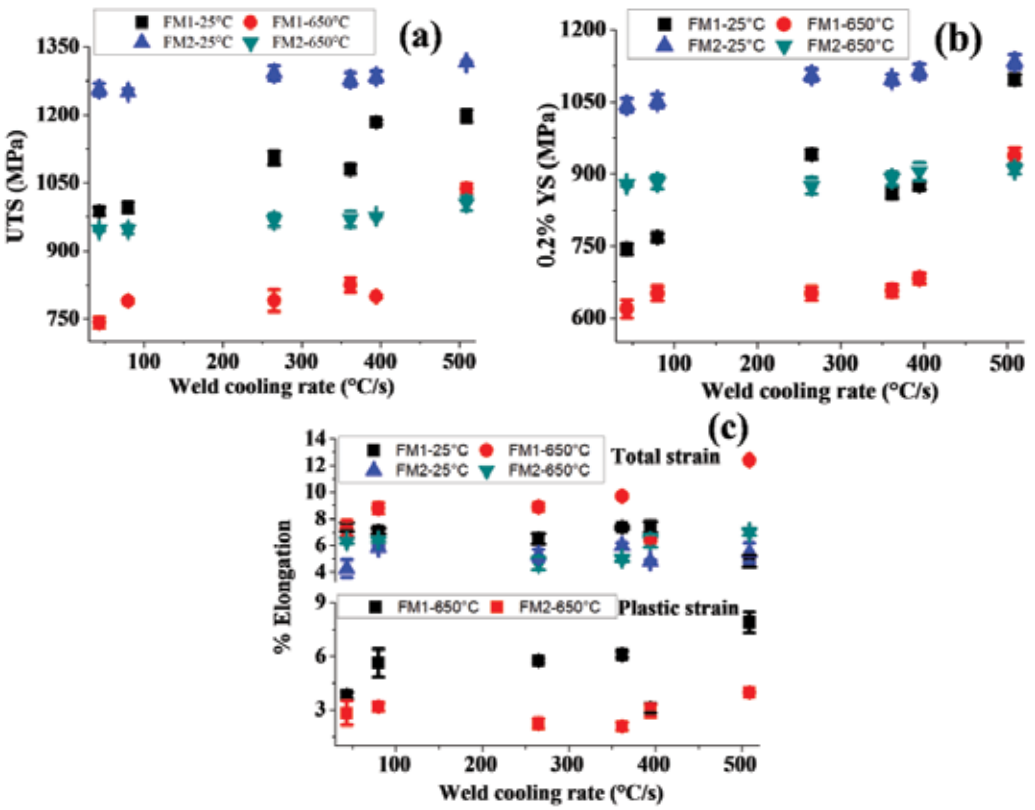

Figure 8. Tensile properties [(a, b) tensile strength and (c) strain] of conventionally and cryogenically cooled FM1 and FM2 weldments at 25 and 650°C.

fusion zone due to the addition of molybdenum which promoted solutal undercooling by the concentration gradient. Hence, the combined effect of thermal and solutal undercooling resulted in a refined microstructure.

The fracture surfaces of the room temperature tensile specimens at 25°C for DA conditions revealed the equiaxed dimple morphology. The fracture surface investigation in SEM indicated a detrimental nature of the Laves phase in fracture process even at 650°C. The fractographs of 650°C tensile tested specimen of FM1 and FM2 are as shown in **Figure 9(a)** and **(b)** for the conventional cooling process.

Among the six fusion zones of different weld cooling rates, the FM1 fusion zone exhibited deep dimple features at 650°C. The fractured surfaces of 650°C testing exhibited a mixed mode (inter and transgranular modes) of fracture with a unique dendritic pattern. The fracture was progressed along the Laves phase. The Laves particles were observed inside the dimple surface for the fusion zones of 40°C/s as shown in **Figure 9(b)**. The microcracks were initiated preferentially by decohesion of laves phase–γ matrix interface under the action of a tensile stress and resulted in a premature failure. The wedge type cracking features were observed in both FM1 and FM2 fusion zones.

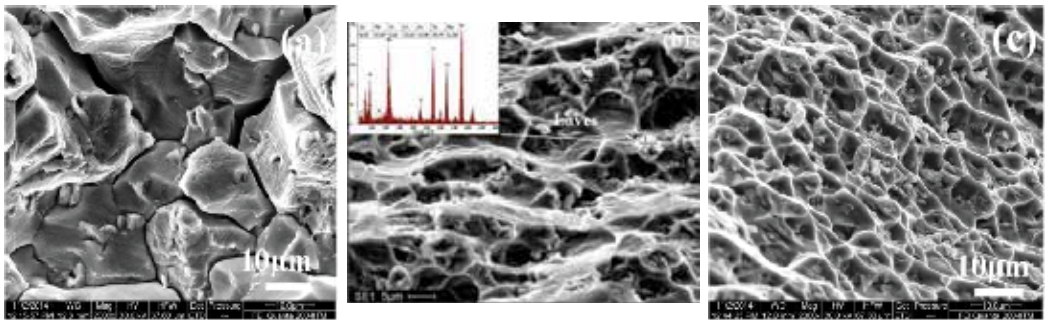

Figure 9. Fractographs of (a, b) conventionally cooled and (c) liquid nitrogen-cooled fusion zones tensile tested at 650°C.

The fractographs of the liquid nitrogen-cooled weldments exhibited transgranular fracture as shown in **Figure 9(c)**. It was proved that the tensile properties of the alloy 718 weldment were reduced at room temperature conditions, especially the weld ductility. Similar results were obtained at room temperature in the present study. In addition, it was observed in the present work that at 650°C tensile properties were also reduced as the Laves particles favored crack initiation and continuous Laves network aided the crack propagation. This led to the easier fracture process. The fracture process was progressed by the nucleation of voids and subsequent growth of macroscopic cracks along the weaker laves-matrix interface even at 650°C. Thus, weld ductility was reduced. As the Laves network was disrupted and refined, equiaxed dendritic microstructure associated with fine and discrete Laves particles enhanced the tensile properties both at 25 and 650°C. The plastic strain of the cryogenically cooled weld metal was higher than that of the conventionally cooled weld metal as shown in **Figure 8(c)**. The liquid nitrogen-cooled fusion zone had increased molybdenum content in the dendrite (4–5 wt%) and molybdenum-bearing phase was observed in the XRD analysis of FM1 fusion zone as shown in **Figure 7(a)**. These phases pinned the grain boundaries and enhanced the plastic strain in liquid nitrogen-cooled weldments.

The room temperature mechanical properties of the hybrid pulsing weldments were evaluated and the maximum tensile strength of 1155 and 1100 MPa for argon and helium shielded FM1 fusion zones at 500 and 2000 Hz, respectively. Similarly, maximum tensile strengths were obtained at 2000 Hz in the argon and helium shielded FM2 (1330 MPa) fusion zones. The maximum yield strength (965 MPa) was obtained in the intermediate pulse frequency (1250 Hz) for the argon shielded FM1 fusion zone and (856 MPa) at 2000 Hz in the helium shielded fusion zone. FM2 fusion zone exhibited a maximum of 1138 MPa yield strength for both argon and helium shielded fusion zone at 1500 and 2000 Hz, respectively. The maximum weld ductility was demonstrated for the helium shielded FM1 weldments than that of the other hybrid pulsing weldments. The high-temperature tensile testing of the transverse welded specimens revealed an ultimate tensile strength values ranging from 989.53 to 1030.15 MPa (±16.79 MPa) and 0.2% yield strength values from a minimum of 843.33 MPa to a maximum of 885 MPa (±17.68 MPa). The ductility of the weld was lower in the range of 3.48–3.6% (±0.14) and a plastic strain of 1–1.26% (±0.05%).

5. Inferences

The interdendritic Laves phase formation during GTA welding of alloy 718 has been investigated using enhanced weld cooling rates and change of weld metal chemistry. The volume fraction of Laves phase was reduced from 45.95 to 8% with the enhanced weld cooling rate by the combination of modified pulse current and helium shielding gas for both FM1 and FM2 fusion zones. This was further reduced to 0.1% while employing cryogenic cooling during GTA welding process. The high energy density processes minimized Laves phase and prone for HAZ microfissures. GTA welding process employed with liquid nitrogen cooling aided in minimizing laves phase and free of HAZ microfissures. Enhanced weld efficiency on UTS and 0.2% YS at 25°C was observed to the tune of 85–93% by employing cryogenic cooling in GTA welding process. Similar improvement in weld efficiency at 650°C was observed. However, the evaluated weld efficiencies with cryogenically cooled weld metal were marginally lower than the previous works in EB and LB welds only by 2–3%. Moreover, it was observed that the Laves network influenced the strength of the weldment at 650°C. The modification of weld metal chemistry with Mo solute element through solid solution filler metal (FM1) promoted solutal undercooling, in addition to the thermal undercooling. Thus, the microstructures were refined and Laves phase formation was reduced. The intermediate pulse frequencies were aiding better Laves phase control for the argon shielded GTA welding process and the same results were obtained with 2000 Hz pulse frequency in the helium shielded process. This could be due to the combined effect of longitudinal temperature gradient while using different shielding gases and shape factor of the pulse wave form.

Author details

S.G.K. Manikandan[1]*, D. Sivakumar[1] and M. Kamaraj[2]

*Address all correspondence to: nehakutty06@gmail.com

1 Indian Space Research Organisation, India

2 Indian Institute of Technology Madras, India

References

[1] Mills WJ. Effect of microstructural variations on the tensile and fracture toughness properties of Inconel 718 weldments. In: Loria PA, editor. Proc. Conf. on 718 alloy. PA: TMS; 1984. pp. 845-858

[2] Reddy GM, Murthy CVS, Srinivasa Rao K, Prasad RK. Mint: Improvement of mechanical properties of Inconel 718 electron beam welds—influence of welding techniquesand postweld heat treatment. International Journal of Advanced Manufacturing Technology. 2009;**43**:671-680

[3] Ram GDJ. Effect of Laves phase on mechanical properties on Inconel 718 welds [Thesis]. Chennai: IIT Madras, Department of Metallurgical and Materials Engineering; 2004

[4] Sivaprasad K, Ganesh Sundararaman S. Mint: Influence of weld cooling rate on microstructure and mechanical properties of alloy 718 weldments. Metallurgical and Materials Transactions A. 2008;**39**(9):2115-2127

[5] Zhang W, Liu L. Mint: Solidification microstructure of directionally solidified superalloy under high thermal gradient. Rare Metals. 2012;**31**(6):541-546

[6] Wang J, Kusumoto K, Nezu K. Mint: Analysis of electrical characteristics for hybrid pulsed micro-tungsten inert gas welding arc. Science and Technology of Welding and Joining. 2004;**9**(4):369-373

[7] Amuda MOH, Mridha S. Mint: Grain refinement and hardness distribution in cryogenically cooled ferritic stainless steel welds. Materials Design. 2013;**47**:365-371

[8] Banovic SW, Du Pont JN, Marder AR. Mint: Dilution and microsegregation in dissimilar metal welds between super austenitic stainless steel and nickel base alloys. Science and Technology of Welding and Joining. 2002;**7**(6):374-383

[9] Knorovsky GA, Cieslak MJ, Headley TJ, Romig Jr. AD, Hammetter WF. Mint: Inconel 718: A solidification diagram. Metallurgical and Materials Transactions A. 1989; **20**(10):2149-2158

[10] Du Pont JN, Robino CV, Micheal JR, Notis MR, Marder AR. Mint: Solidification of Nb-bearing superalloys: Part I. Reaction sequences. Metallurgical and Materials Transactions A. 1998;**29A**:2785-2796

[11] Han D, Liu F, Jia D, Qi F, Yang H, Sun W, Hu Z. Effect of Mo addition on the grain growth of IN718 alloy. Materials Science Forum. 2015;**816**:594-600

Chapter 2

High-Temperature Oxidation of Superalloy C-263 of Rings for Aircraft Engines

Citlalli Gaona Tiburcio, Alejandro Lira Martinez,
Jorge Taboada Solis, Patricia Zambrano Robledo,
Francisco Estupiñán López,
Jose Cabral Miramontes and
Facunda Almeraya Calderón

Additional information is available at the end of the chapter

http://dx.doi.org/10.5772/intechopen.70256

Abstract

The present investigation was conducted to study the oxidation kinetics of nickel-based superalloy 263, used in the manufacture of rings for aircraft engines. For carrying out this study, we first conducted microstructural characterization of the pieces using the techniques of optical microscopy, scanning electronic microscopy, and X-ray diffraction. Subsequently, using the thermogravimetric analysis, the kinetic oxidation of the metal was performed in a temperature range between 700 and 1000°C, using atmospheres of O_2. The results of the micrographs show the formation of a protective oxide film on the surface of the material in different oxidizing agents. Finally, it was found that the kinetics of high-temperature oxidation of the superalloy C-263 obeys the parabolic rate law.

Keywords: superalloys, oxidation, thermogravimetric, aircraft engines

1. Introduction

In order to meet the current demand for the aerospace industry, the production of advanced materials is required that ensure the design and manufacture of a robust product and that meet customer expectations, increased engine performance for fuel efficiency, mechanical strength of the components, and at the same time be lighter and less expensive. Therefore, there is a great interest in the development and study of superalloys that will generate

mechanically resistant aircraft, capable of withstanding corrosive environments at high temperatures. Inside a combustion chamber at duty, on a gas turbine engine of aircraft, very aggressive corrosive agents exist. One of these is sulfur, which can deteriorate the materials and reduce their useful life [1].

Nickel-based superalloys are generally used at temperatures above 540°C in very aggressive environments. Seamless rolled rings are made of superalloy Haynes C-230 or C-263 and used in the combustion chamber of gas turbine engines, which are exposed to corrosive gas mixtures. One of those gases is SO_2. However, because of its machining process, its corrosion-resistant properties may be compromised [2, 3].

Sulfur is generally present as an impurity in fuels and air. When combustion takes place with excess of air to ensure complete combustion of fuel, sulfur reacts with oxygen to form mainly SO_2, which is a corrosive gas. However, sulfidation in oxidizing environments is frequently accelerated by other impurities such as sodium, potassium, and chlorine, making possible the so-called hot corrosion mechanism [4].

Superalloys exposed in SO_2 environments generally form oxides and/or sulfides as corrosion products, which depend strongly on temperature. The highest corrosion rate is normally related to the formation of sulfides [1]. Sulfides provide paths for rapid outward diffusion of metals resulting in rapid corrosion attack. For nickel, the corrosion rate in this environment is around 600°C, and above 800°C, the rate decreases with increasing temperature.

Haynes 263 is a nickel-chromium-tungsten-molybdenum alloy that combines high-temperature strength, resistance to oxidizing environments up to 1149°C for prolonged exposures, premier resistance to nitriding environments, and excellent long-term thermal stability [5].

The manufacturing process for forging rings [6] of superalloys may be used in turboreactors or components of the high-temperature section of a gas turbine such as the combustion chambers of the intermediate-temperature section (**Figure 1**) [7].

Figure 1. Seamless rolled rings for aircraft engines [6].

There are a large number of nickel-based superalloys in the world such as the C-263 which contains multiple phases, depending on the alloying elements. The most prevalent phase in this superalloy is the gamma (γ) phase, with a cubic crystalline structure centered on the faces. Ni-based superalloys are hardened, due to the formation of solid solutions, using a variety of substitution alloying elements in the γ-structure such as molybdenum. In the case of superalloy C-263, aluminum and titanium only make up about 3% of the total composition. However, these components are important for the properties of the materials associated with superalloys, due to the formation of the γ'-phase [8].

In metallic corrosion, the oxidation of alloys at high temperatures can be treated as a special case, which considers the material destruction due to chemical causes, in which solid phases interact either with a liquid agent or a gaseous agent. The latter case involves reducing and oxidizing gases, steam, and even free oxygen. The oxidation is determined by the internal mobility of the solid phases and mainly diffusion in solid state. It is well known that alloying with chromium improves the oxidation resistance of iron at high temperatures [9].

The principal objective in this research was to study the oxidation kinetics of nickel-based superalloy C-263 in a temperature range of 700–1000°C using atmospheres of O_2 for 48 h.

2. Experimental procedure

The material used in this research was Haynes C-263 superalloy. The specimens were sections of 4 × 4 × 2.5 mm. The surface of samples was ground using 2000 grade grit paper, rinsed with distilled water, and degreased with acetone [10].

Figure 2. Thermogravimetric analyzer TA Instruments.

The oxidation test was performed in a thermogravimetric analyzer TA Instruments Hi Res TGA 2950 (**Figure 2**), for 48 h. Experiments were conducted in gaseous atmosphere of O_2–N_2 with a flow of 75 ml/min at an interval of temperatures of 700–1100°C (+2°C). For each specimen a weight gain measurement in an electronic microbalance (sensitivity 10^{-6} g) was set.

The oxidized samples were analyzed in a scanning electron microscopy (SEM; FEI Nova NanoSEM 200) coupled with an energy-dispersive X-ray spectroscopy (EDS) system, in order to understand the oxidation phenomena in terms of scale morphology and oxidation product distribution.

3. Results and discussion

3.1. Chemical analyzer

The chemical composition of superalloy C-263, used in the present study, is given in **Table 1**. The chemical analysis was performed using the technique of X-ray fluorescence.

3.2. Alloy microstructure

The microstructure of the alloys in the study (**Figure 3**) is composed of an austenitic matrix gamma (γ) and twins that are typical in this material, with intermetallic precipitates of gamma prima (γ'). The precipitates in the microstructure are in the form of carbides and some borides, and the grains are regular.

3.3. Thermogravimetric analyzer

The kinetic measurements indicated that, in general, the alloys presented a parabolic behavior, according to

$$(\Delta m/A)^2 = K_p(t - t_o) \quad (1)$$

where $(\Delta m/A)$ is the weight gain per unit area; t and t_o are the final and initial time, respectively; and K_p is the parabolic rate constant [11].

The increase in mass gain, higher as temperature increases, is significantly lower as the exposure time increases. This progressive decrease in the rate of oxidation indicates the formation of a compact and well-adhered oxide. According to Wagner's [12] theory, systems subjected to high temperature and controlled by diffusion processes, through the network of the oxide layer, follow an oxidation kinetics described by a parabolic-type equation.

Chemical composition (% wt.)											
Material	Ni	Cr	Co	Mo	Ti	Fe	Al	Mn	Si	Cu	C
C-263	51.80	20.20	19.90	6.00	2.30	0.69	0.60	0.62	0.40	0.19	0.05

Table 1. Chemical composition of superalloy C-263.

http://dx.doi.org/10.5772/intechopen.70256

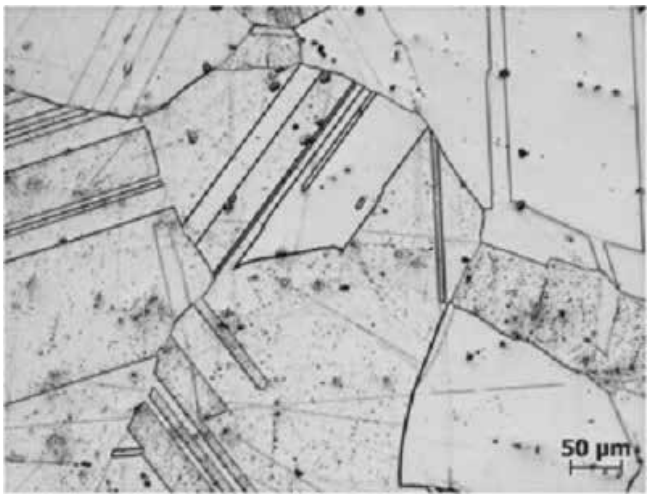

Figure 3. Microstructure of superalloy C-263.

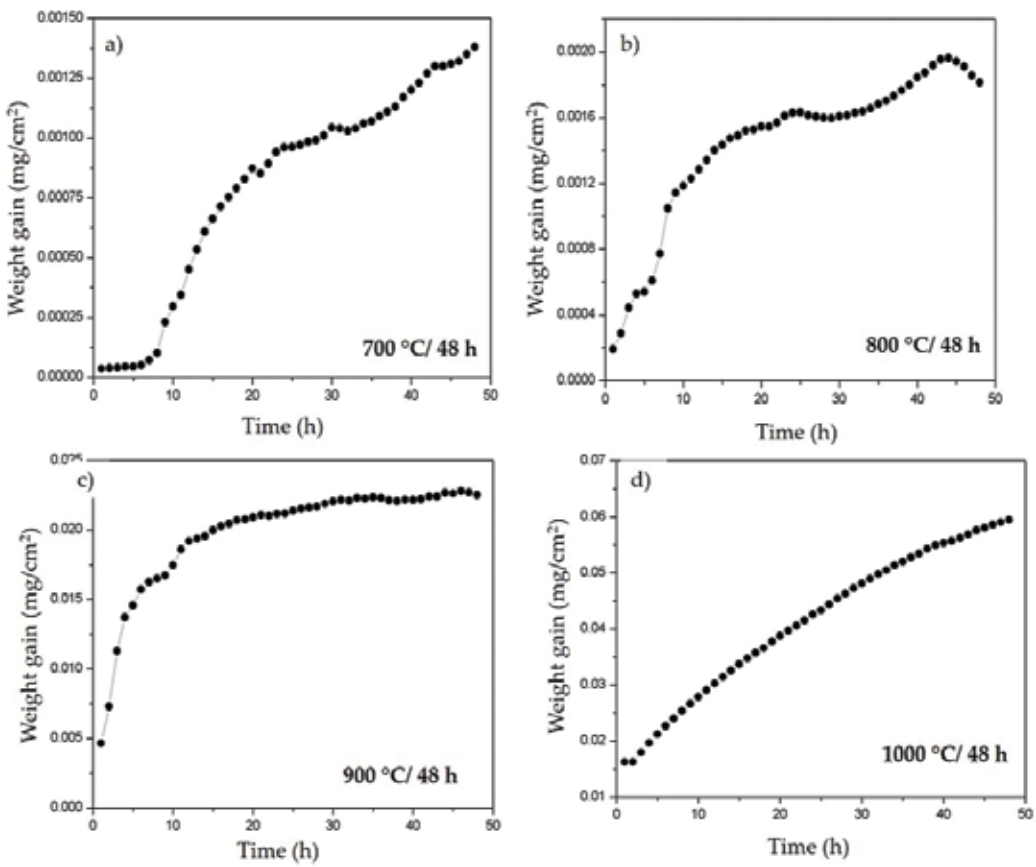

Figure 4. Dependence of the weight gain on the oxidation time in O_2 at (a) 700°C, (b) 800°C, (c) 900°C, and (d) 1000°C for 48 h.

Oxidation kinetics of superalloy C-263 was studied at 700, 800, 900, and 1000°C; **Figure 4** shows the weight change per unit area versus time. Evidently, the oxidation rate increases as the temperature rises. A parabolic behavior was found at all testing temperatures. The kinetic results are in agreement with those reported in the literature in the sense that the kinetic behavior is parabolic [13, 14].

In order to better visualize this behavior, the square of the mass increase per unit area for superalloy C-263 at the temperatures mentioned above has been plotted in **Figure 5**. For all the cases studied, there is a linear relationship between both variables. This fact confirms that the oxidation of superalloy at the four test temperatures follows a parabolic law. The indicated graphs also allow to calculate the parabolic oxidation rate constants (see **Table 2**).

Knowing the parabolic rate constant for each temperature, the activation energy of the oxidation reaction can be calculated from the Arrhenius equation, which relates K_p to the temperature by the expression:

$$K_{p=} K_o e^{\left(-\frac{Q}{RT}\right)} \tag{2}$$

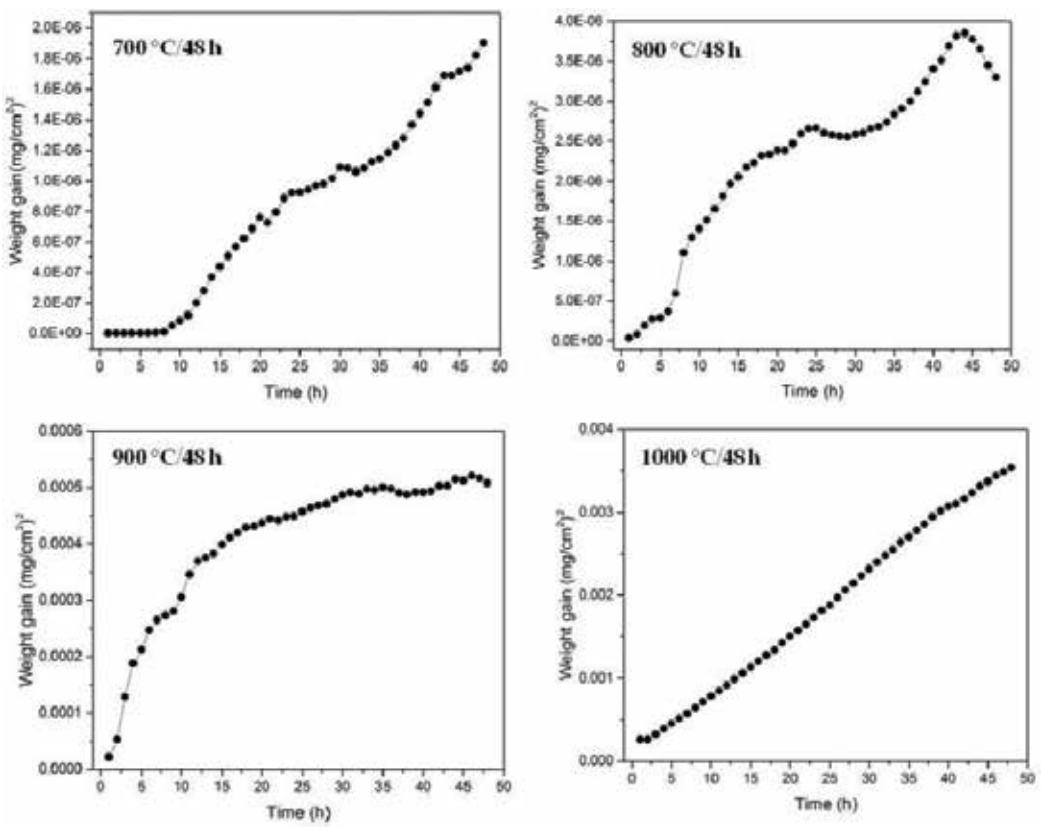

Figure 5. Parabolic oxidation of superalloy C-263.

Temperature (°C)	Parabolic oxidation rate constants (mg^2/cm^4 h)
700	4.18×10^{-8}
800	7.21×10^{-8}
900	7.66×10^{-6}
1000	7.16×10^{-5}

Table 2. Values of the parabolic oxidation rate constant (mg^2/cm^4 h).

where Q is the activation energy; R is the gas constant, in joules or calories; K_o is the rate constant at room temperature; and T is the absolute temperature.

In **Figure 6** the parabolic oxidation rate constant is obtained against the inverse of the temperature. The value of the activation energy Q is 28.37 kcal/mol and is indicative that the oxidation process is diffusion controlled through the layer of oxides formed.

The oxide layer in the superalloy samples at 700, 800, and 1000°C remained adherent to the substrate, but not at 900°C, which, after finishing the test, was probably due to the stresses generated with the thermal contraction.

Garcia-Alonso et al. studied the oxidation kinetics of the MA 956 superalloy in the temperature range of 800–1200°C for up to 200 h exposure. During oxidation the alloy develops a fine, compact, and very well-adhered alpha-alumina layer, the thickness of which increases with increasing

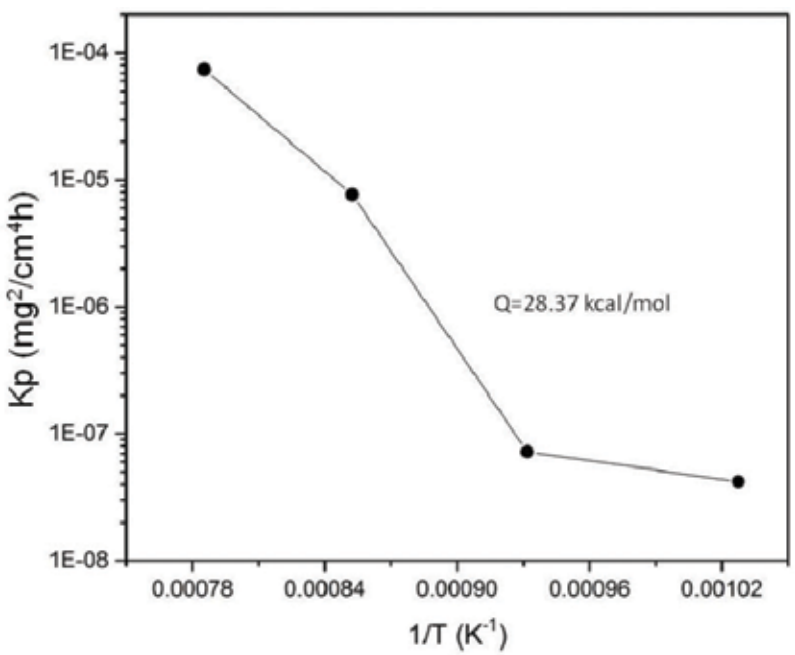

Figure 6. Constant of the oxidation rate of superalloy C-263 as a function of temperature.

time and temperature. The oxidation kinetics obeys a subparabolic-type behavior, and the oxidation process would be controlled by alpha-alumina and below 900°C by 7-alumina.

Other authors have studied the behavior of high-temperature oxidation of nickel-based superalloys in different temperature ranges, where the kinetics of oxidation obeys the parabolic law by the addition of elements such as aluminum, titanium, niobium, or yttrium [15, 16].

The Encinas-Oropesa study targeted at characterizing the oxidation behavior of a new nickel-based disk alloy (RR1000) at intermediate temperatures (700–800°C for exposures up to 200 h). The mass gain data obtained have been used to derive oxidation reaction rate parameters, using established methodologies, with parabolic rate constants varying between 1.4×10^{-5} $mg^2/cm^4/h$ at 700°C and 8.4×10^{-4} $mg^2/cm^4/h$ at 800°C [17].

3.4. Scanning electron microscopy (SEM)

The results obtained by SEM on the oxidized specimens revealed different morphologies depending upon the temperature of testing.

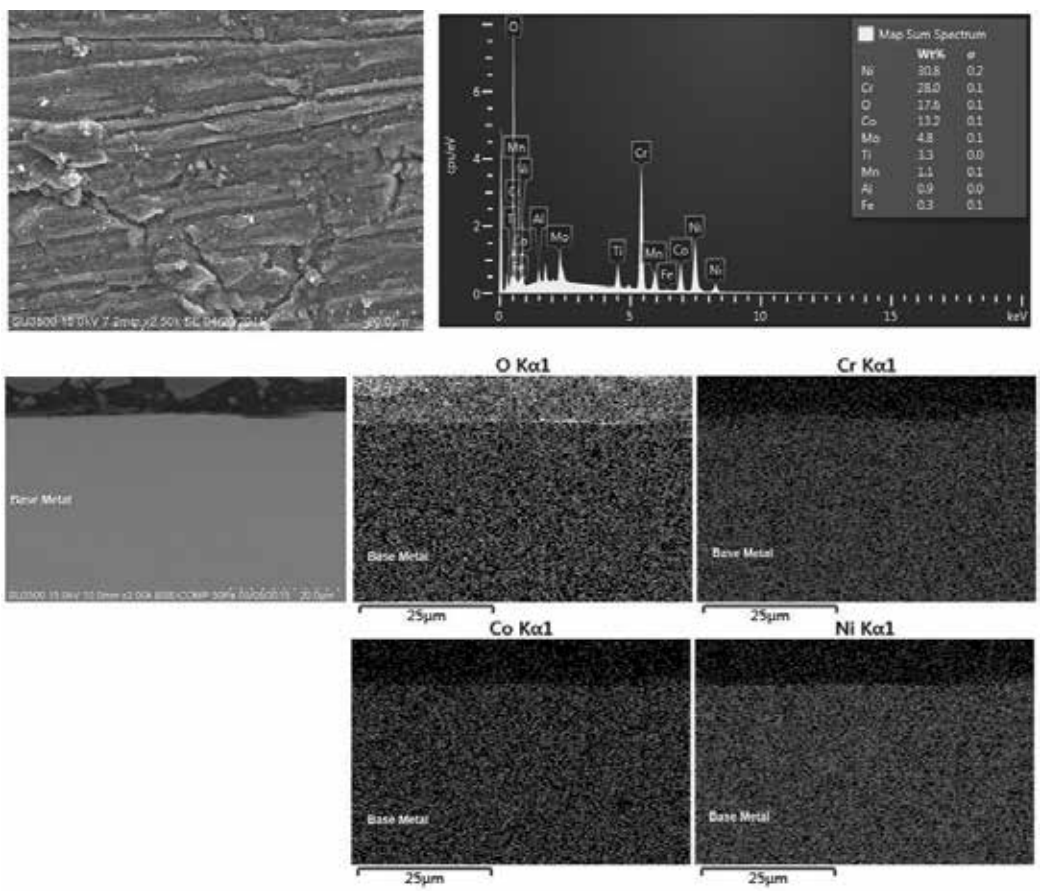

Figure 7. Superalloy C-263 at 700°C for 48 h, superficial morphology, cross section, and X-ray map for O, Ni, Co, and Cr.

http://dx.doi.org/10.5772/intechopen.70256

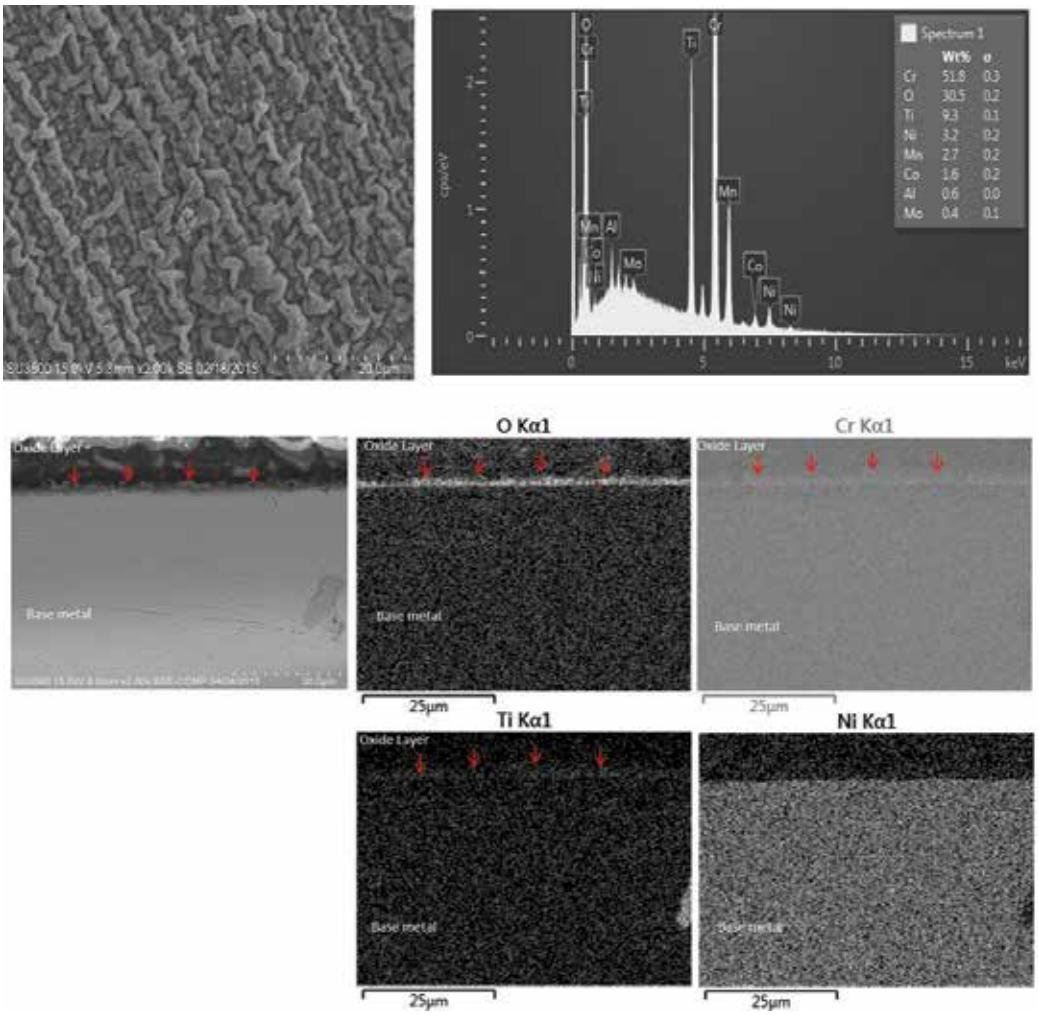

Figure 8. Superalloy C-263 at 800°C for 48 h, superficial morphology, cross section, and X-ray map for O, Ni, Ti, and Cr.

The superficial morphology at 700°C presents fine-grained oxides and brittle banded agglomerates (**Figure 7**). Cross-sectional analysis of the samples by SEM/EDS on the layer formed on all alloys suggested the formation of titanium- and chromium-rich oxides.

At 800°C morphology with banded agglomerates, rich in chromium and titanium, is observed; these same elements develop a thin and not very homogeneous layer of chromium oxide and titanium (see X-ray map; **Figure 8**).

Observing the morphology obtained from the superalloy C-263 heat treated at 900°C for 48 h (1000 X), a surface totally covered by a great amount of particles with different sizes and defined morphologies can be noted, although they are more evident those that have form of bars, with larger particle size. **Figure 9** shows the formation of an abundant oxide

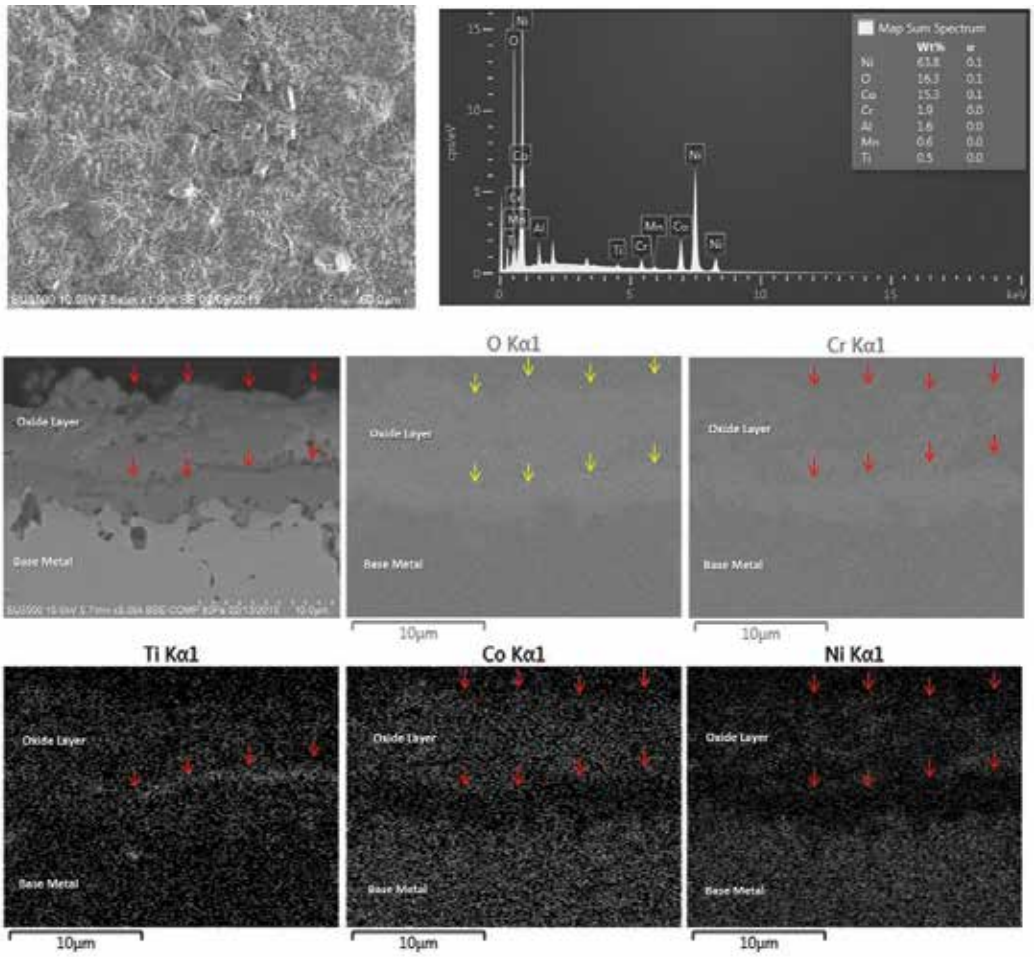

Figure 9. Superalloy C-263 at 900°C for 48 h, superficial morphology, cross section, and X-ray map for O, Ni, Co, Ti, and Cr.

layer, in which two layers of oxide, internal and external, can be observed. The inner layer consists mainly of chromium oxide, and the outer layer is formed by an oxide of cobalt and nickel. Between both layers there is an oxide of titanium.

The presence of chromium in this type of superalloys not only improves the mechanical properties by hardening at high temperatures but also stabilizes the phase. Oxidation studies in superalloys with the presence of aluminum and chromium have shown a high tendency of formation of continuous and protective films above 900°C [18–20].

When this superalloy C-263 was treated at 1000°C for 48 h, different morphologies and particle sizes are observed. On the one hand, defined grains with particle sizes between 5 and 10 μm and in some areas the formation of smaller particle agglomerates covering the grains

http://dx.doi.org/10.5772/intechopen.70256

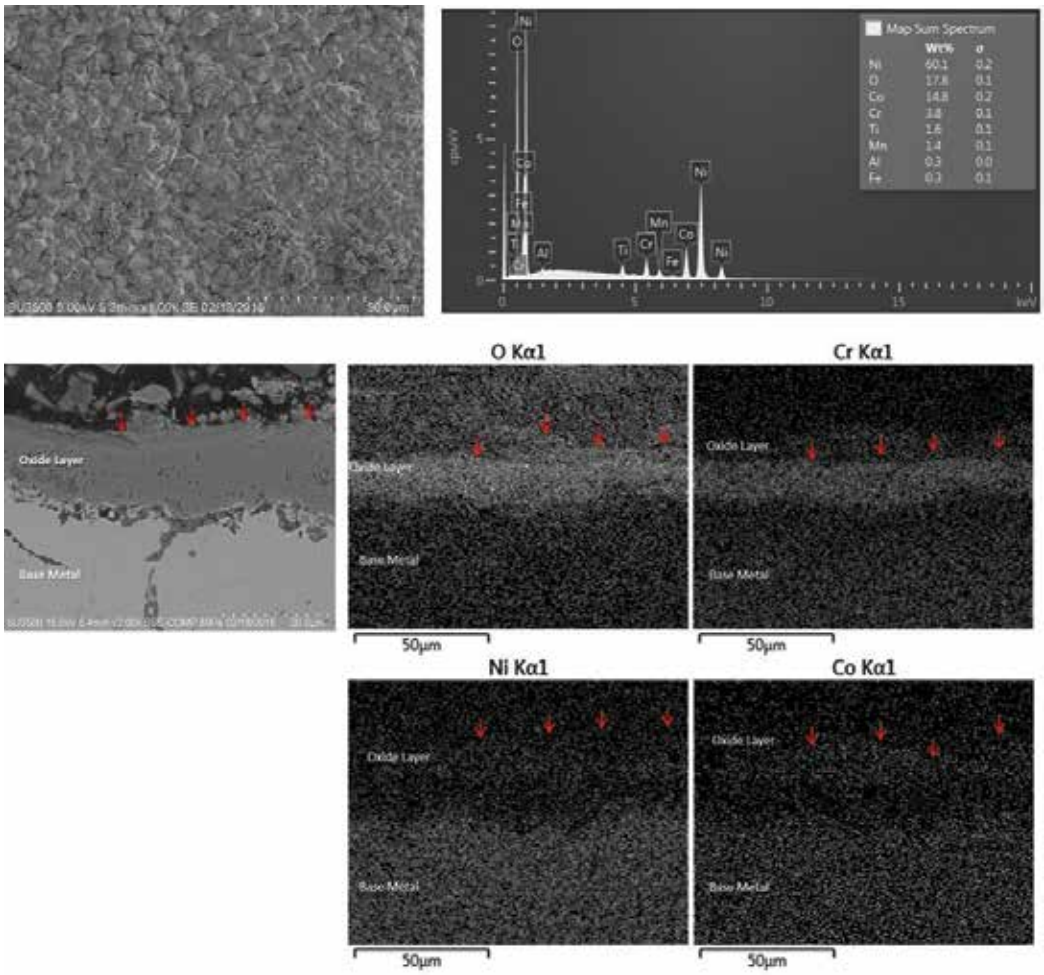

Figure 10. Superalloy C-263 at 1000°C for 48 h, superficial morphology, cross section, and X-ray map for O, Ni, Co, Ti, and Cr.

are observed. In X-ray map can be observed, the formation of an abundant oxide layer, in which two layers of oxide, internal and external, is observed; the inner layer is made up mostly of chromium oxide, and the outer layer is formed by a cobalt and nickel oxide (see **Figure 10**; 1000 X).

By SEM-EDS at 800, 900, and 1000°C, the formation of a larger amount of Cr oxide, Ti, and Ni on the surface of superalloy was observed. It was determined that while the temperature of the thermal treatment increased, the amount of the oxide is increased.

The growth rate of Cr_2O_3 scales at high temperatures is greatly reduced by the presence of elements as nickel, titanium, and cobalt [21].

4. Conclusions

- The kinetics of high-temperature oxidation of the superalloy C-263 obeys the parabolic rate law for temperatures 700, 800, and 1000°C.
- Cross-sectional analysis, by SEM/EDS, of the layer formed on all samples suggested the formation of titanium- and chromium-rich oxides and in some cases cobalt and nickel oxide after 900°C.
- The present investigation found that at 700°C, there is almost no oxide on the surface of the superalloy, only seen a little agglomerates of Mn, Cr, and Ni as major components of the superalloy matrix.

Author details

Citlalli Gaona Tiburcio[1], Alejandro Lira Martinez[2], Jorge Taboada Solis[1], Patricia Zambrano Robledo[1], Francisco Estupiñán López[1], Jose Cabral Miramontes[1] and Facunda Almeraya Calderón[1]*

*Address all correspondence to: falmeraya.uanl.ciiia@gmail.com

1 Universidad Autónoma de Nuevo León (UANL), Facultad de Ingeniería Mecánica y Eléctrica (FIME), Centro de Investigación e Innovación en Ingeniería Aeronáutica (CIIIA), Av. Universidad s/n. Ciudad Universitaria. San Nicolás de los Garza, Nuevo León, México

2 Universidad Autónoma de Ciudad Juárez, Instituto de Ingeniería y Tecnología, Cd Juárez, Chihuahua, México

References

[1] Lai GY. High Temperature Corrosion and Materials Applications. 1st ed. USA: ASM International; 2007. p. 345

[2] Rolls R. The Jet Engine. 1st ed. UK: Rolls Royce Technical Publican; 1996. p. 126

[3] Klause H. Jet Engines: Fundamentals of Theory, Design and Operation. 1st ed. Stuttgart, Germany: Motorbooks International Publishers; 2003. p. 345

[4] Stringer J. Hot corrosion in gas turbines. Corrosion. 1972;**28**(5):161

[5] Haynes. Haynes 263 Alloys. 03-02-2015. Available from: http://wwwhayesintl.pdf/h3000.pdf

[6] FRISA. Manufacture Process [Internet]. 02-01-2015. Available from: htto://www.frisa.com/process/manufacturing-process

[7] Pollock T, Tin S. Nickel-based superalloys for advanced turbine engines: Chemistry, microstructure and properties. Journal of Propulsion and Power. 2006;**28**(2):161-374

[8] Pettit F, Meier G. Oxidation and hot corrosion of superalloys. TMS. 1984;**1**:651-687

[9] Seybolt AU. Observations on the Fe-Cr-O System J. Electrochem. Soc. 1960;**107**(3):147-156

[10] ASTM E3-11. Standard Guide for Preparation of Metallographic Specimens. 100 Barrr Harbor Dirve, PO box C700, West Conshohocken, PA, 19428-2959, USA: ASTM International

[11] Saucedo-Acuña RA, Almeraya-Calderón F, De la Torre SD, Martínez-Villafañe A. ICC, editor. Proceedings of the 15th International Corrosion Congress; Granada, España. España: ICC; 2002. p. 570

[12] Wagner C. Atom Movements. ASM; 1951. p. 153

[13] Nakamura Y. Metallurgical Transactions. 1974;**5**:909

[14] Golightly FA, Wood GC, Stott FH. Oxidation Metals. 1980;**14**(3):217

[15] Weng F, Yu H, Chen C. Corrosion Science. 2013;**75**:58-66

[16] Taylor MP, Evans HE, Stekovic S. Surface and Interface Analysis. 2015;**47**(3):362-370

[17] Encinas OA, Simms NJ, Nicholls JR, Hardy MC. Journal Materials at High Temperature. 2009;**26**(3):241-249

[18] Reed RC. The Superalloys Fundamentals and Applications. 1st ed. UK: Cambridge University Press; 2006. p. 390

[19] Moussa SO, Morsi K. Journal of Alloys and Compounds. 2006;**426**(1-2):136-143

[20] Szacalos P, Lundberg M, Pettersson R. Corrosion Science. 2006;**48**(7):1679-1695

[21] Martínez-Villafañe A, Chacón NJ, Gaona TC, Almeraya CF, et al. Materials Science Engineering A. 2003;**A263**:15-19

Chapter 3

Hot Corrosion of Superalloys in Boilers for Ultra-Supercritical Power Plants

Nageswara Rao Muktinutalapati,
Arivazhagan Natarajan and Moganraj Arivarasu

Additional information is available at the end of the chapter

http://dx.doi.org/10.5772/intechopen.76083

Abstract

The coal-based power plants have been plagued by twin problems—low thermal efficiency and emission of high level of pollutants into the environment. Over the last few decades, attention was paid by researchers worldwide to overcome these problems and to design, build, and operate coal-based plants with improving efficiency levels and reducing emission levels. Operating the power plants with higher levels of steam temperature and pressure was adopted as the direction toward achieving the needed improvements. The requirement to operate the plants with increasingly higher levels of temperature and pressure made it necessary to design the components with superalloys. Hot corrosion then becomes a major design consideration, particularly for superheaters and reheaters. Thus, it becomes important to study the hot corrosion behavior of candidate superalloys. The present chapter attempts to review the work done over the last two decades to understand the hot corrosion behavior of superalloys in the context of their use in advanced coal-based power plants.

Keywords: ultra-supercritical coal fired power plants, nickel-based superalloys, hot corrosion, fireside corrosion, sulfidation

1. Introduction

Ultra-supercritical (USC) power plants are expected to overcome two challenges—(i) an increase in demand for electricity and (ii) a significant reduction in the enhanced greenhouse effect due to CO_2 emission from the fossil fuel. By increasing the operating temperature and pressure of the steam systems, an increase in the power plant efficiency and a major reduction

in the CO_2 emission from the power plants based on firing pulverized coal can be realized [1]. The goal of the latest designs in power plants is to generate 760°C steam. In the process, metal surface temperature of the key components such as superheaters and reheaters may reach as high temperature as 800°C [2]. The materials used for superheaters and reheaters in coal-fired boiler environments always suffer coal ash hot corrosion at elevated temperatures [3, 4]. Coal ash hot corrosion is the result of competition between oxidation and sulfidation. Sulfidation comes into picture as the materials get exposed to high-temperature combustion gases containing sulfate coal ash [5]. Superalloys, in particular, nickel-base superalloys, have been the candidate materials for application in boilers for ultra-supercritical power plants based on firing coal. Compared to different types of high-temperature steels, nickel-based superalloys are well known for their superior resistance to coal ash hot corrosion [6, 7]. While there have been several publications on use of high-temperature materials in advanced power plants, a systematic review of application of superalloys for critical components facing hot corrosion and high temperature creep loading conditions in advanced coal-based power plants has not been carried out in the recent years. This chapter proposes to bridge this gap.

2. What are ultra-supercritical power plants?

Because of the abundant availability of coal reserves in the world, the use of coal for electricity generation has been done extensively. Coal has thus dominated as fuel for electricity generation, even though many modern technologies have emerged for power generation. Use of coal for power production is, however, beset with serious problems. Coal-based power plants emit pollutants and CO_2 at high levels. Further, the efficiency of the conventional coal-based power plants has been very low, 35–40%. The efficiency of the power plant can be increased by increasing the operating steam temperature and pressure. Development studies were undertaken worldwide to build power plants with increased values of these two operating parameters. In addition to increased thermal efficiency, an increase in these two parameters would lead to a reduction in greenhouse gases, an issue where the public is becoming increasingly conscious of.

Several of the existing coal-based power plants belong to the category of subcritical power plants operating at a steam pressure of ~22 MPa and a steam temperature of ~550°C; the thermal efficiency of these plants is in the range of 35–37%. The plants operating in the temperature range of 540–580°C with steam pressure extending up to 25 MPa are termed supercritical power plants; their efficiency is of the order of 45%. Ultra-supercritical power plants operate

	Main steam pressure, MPa	**Main steam temperature, °C**	**Reheat steam temperature, °C**	**Average efficiency**	**CO_2 emissions (g/KWh)**
Subcritical	<22.1	Up to 565	Up to 565	36	766–789
Supercritical	22.1–25	540–580	540–580	45	722
Ultra-supercritical	>25	>580	>580	>45	<722

Table 1. Classification of power plant conditions [8].

at temperature higher than 580°C and pressure higher than 25 MPa, leading to an efficiency level of more than 45%. All over the world, several plants have been set up conforming to ultra-supercritical technology. Recent advances in the alloy making and processing capability to produce different items of hardware from these alloys have resulted in the possibility of setting up advanced ultra-supercritical power plants, where the operating temperature would be 700°C or more and operating pressure in the range of 30–35 MPa. The associated efficiency is expected to be equal to or better than 50%. These advancements in terms of temperature and pressure parallelly result in a reduction in emitted CO_2 levels. **Table 1** gives the details.

3. Hot corrosion in coal-fired boilers

Materials that exhibited strength to withstand the higher temperatures and pressures present in the superheaters of supercritical and ultra-supercritical advanced boilers with required stress rupture strength were available, but they proved to be especially susceptible to corrosion by certain coals, most notably high sulfur-bearing varieties.

The cause of this type of corrosion, referred to as coal ash corrosion or hot corrosion or fireside corrosion in advanced power plant terminology was soon understood. It is now generally accepted to be due to the presence of liquid alkali iron trisulfates on the surface of the superheater and reheater tubes beneath an overlying ash deposit. Coal ash corrosion or hot corrosion is a widespread problem for superheater and reheater tubes, especially when high sulfur, high alkali, and high chlorine coals are used, and is a crucial problem that needs to be resolved before advanced ultra-supercritical boilers can be deployed. The loss from corrosion increased with high levels of SO_2, alkali sulfates, and temperature.

Performance of nickel superalloys in such industries as aerospace or gas or marine turbines has been well documented. However, it is important to note that the operating conditions within a coal-fired boiler are very different in terms of the service environment. Hot corrosion as it occurs in coal-fired boilers is a complex topic since it is a consequence of the combined effect of combustion gas atmosphere, fly ash deposits, and the alloy itself.

4. Components/subsystems subjected to hot corrosion in ultra-supercritical power plants

High-performance materials are required to be used for the manufacture of different sections in boilers and steam turbines of an ultra-supercritical power plant. **Table 2** summarizes the prime design requirements for the selection of materials for various critical parts in boilers and steam turbines. The superheater and reheater tubing are among the sections exposed to severe environmental conditions. The outside surface of the tubing suffers fireside coal ash corrosion, while the internal surface faces steam-side oxidation conditions. In addition, the materials used for the subject tubing have to possess adequate stress rupture strength, as they are subjected to long hours of mechanical loading at elevated temperatures.

	Design requirements
Boiler	
Headers/steam pipes	Thermal fatigue strength, weld strength
Reheater and superheater tubes	Creep rupture strength and fireside corrosion resistance
Steam turbine	
Casings/shells	Steam-side oxidation resistance
Bolting	Resistance to stress relaxation up to maximum steam temperature
Rotors/discs	Steam-side oxidation resistance, creep rupture strength, resistance to thermal fatigue cracking
Vanes/blades	Steam-side oxidation resistance, solid particle erosion resistance

Table 2. Components in ultra-supercritical power plants where superalloy grades have come into consideration.

5. When does the designer choose superalloys for these components?

Development of USC power plants requires high-performance alloys able to resist the high temperature and pressure conditions occurring in such plants. Materials for superheaters and reheaters need to possess high creep strength and fireside corrosion resistance when it comes to fulfilling the requirements of highly efficient power plants. Development of qualified alloys for boiler heat exchangers was a very important task in the last decade. At temperatures higher than about 600°C, martensitic alloys are limited by their creep strength performance [25]. Accordingly, substitution of ferritic and martensitic materials with more creep-resistant materials became necessary. Aiming at efficiencies above 40%, iron-base austenitic alloys came for consideration and design with nickel-base superalloys became essential for 700°C technology. Since the beginning of advanced ultra-supercritical power plant concept in the 1990s in Europe, different nickel-based superalloys have been evaluated for their fireside corrosion, steam-side oxidation, and resistance to creep and stress rupture. **Table 3** gives the chemical composition of nickel-based superalloys that have been the subject of studies in the context of their usage on USC power plants.

6. Overview of work done in the area by different researchers

A number of superalloy grades were studied by different researchers for their hot corrosion behavior in USC power plants. **Table 4** gives a summary of these studies. Different material characterization techniques were adopted to study the nature of corrosion products appearing on the exposed surface; **Table 5** gives a list of them. Based on the characterization, conclusions were drawn on the phases occurring in the scale resulting from hot corrosion. **Table 6** summarizes the findings of different authors for the two superalloy grades 617 and 740. Some of the studies carried out in the past also looked into the relative performance of different superalloy grades in USC power plant environments. Published information in this respect has been summarized in **Table 7**.

Sl. No.	Material	Ni	Cr	Co	Mo	W	Al	C	Fe	Mn	Si	S	Ti	Cu	B	Nb	La	P	Refs.
1	Inconel 740	49.5	25.0	20	0.5	—	0.9	0.03	0.7	0.3	0.50	<0.002	1.8	<0.1	0.002	2.0	—	<0.002	[9]
2	Inconel 740H	49.0	25.0	20	0.5	—	1.35	0.03	0.7	0.3	0.15	<0.002	1.35	<0.1	0.002	1.5	—	<0.002	[10]
3	Inconel 617	>44.5	20.0–24.0	10.0–15.0	8.0–10.0	—	0.8–1.5	0.05–0.15	<3.0	<1.0	<1.0	<0.015	<0.6	<0.5	<0.006	—	—	—	[11]
4	Haynes 230	57	22	<5.0	2.0	14	0.3	0.1	<3.0	0.5	0.4	—	<0.1	—	—	<0.5	—	—	[12]
5	Haynes 282	57	20	10	8.5	—	1.5	0.06	<1.5	<0.03	<0.15	—	2.1	—	0.005	—	—	—	[13]
6	Alloy 263	Bal.	19.0–21.0	19.2–21.0	5.6–6.1	—	1.9–2.4	0.04–0.08	<0.7	<0.60	<0.40	<0.007	2.4–2.8	<0.20	<0.005	—	—	—	[14]

Table 3. Chemical compositions of candidate superalloy grades for ultra-supercritical power plant applications.

http://dx.doi.org/10.5772/intechopen.76083

Sl. No.	Super alloy	Refs.
1	740	[5, 15–19]
2	740H	[17, 20]
3	Haynes 282	[21]
4	Alloy 263	[17, 18]
5	Alloy 617 and derivatives	[17, 18, 20, 22, 23]
6	600,601,690,602CA,214,45TM,HR160,693	[24]
7	Alloy 230	[20, 24]

Table 4. Superalloy grades studied for their hot corrosion behavior in USC power plat environments.

Sl. No.	Characterization techniques used
1	Thermogravimetric analysis (TGA)
2	Scanning electron microscopy (SEM)
3	Energy-dispersive spectroscopy (EDS)
4	X-ray diffraction (XRD)
5	Electron-probe microanalysis (EPMA)

Table 5. Techniques used by researchers to characterize the hot corrosion in simulated USC power plants.

Sl. No.	Material	Phases	Refs.
1	Alloy 740	NiO, Cr_2O_3, CrS, Ni_3S_2, (Ni, Co)Cr_2O_4, $Fe(CrAl)_2O_4$	[15]
3	Alloy 740	Co_3S_4, Ni_3S_2, (Ni, Co)Cr_2O_4, Al_2O_3, TiO_2, $NaKS_2O_7$, Cr_2O_3,	[19]
2	Alloy 740	$Cr_2(SO_4)_3$, Ni_3S_2, Co_3S_4, CrS, TiS,	[5]
4	Alloy 617	Cr_2O_3, Al_2O_3, TiO_2, CrS,$NiCr_2O_4$, $CoCr_2O_4$, $FeCr_2O_4$, Fe_2O_3, $Cr_2(SO_4)_3$, NiO	[23]

Table 6. Phases observed in the scale formed after hot corrosion of different superalloy grades in simulated USC power plant environment.

Sl. No.	Alloy grades studied	Rating based on corrosion resistance	Refs.
1	740, 263, 617	740 > 263 > 617	[18]
2	740, 740H	740H > 740	[17]
3	617, 617B	617B > 617	[22]
4	740H, 263, 617	740H > 263 > 617	[10]

Table 7. Relative rating of candidate superalloy grades from the point of view of hot corrosion in simulated USC power plants.

7. Mechanisms of hot corrosion of superalloys in USC power plants

7.1. Initiation and propagation of hot corrosion reaction

From the studies carried out in the past, it emerges that hot corrosion reaction occurs in two phases. In the first phase, referred to as initiation phase, there is essentially no weight change, and the chromium oxide layer formed on the surface is still protective in nature. In the second phase, referred to as propagation phase, the chromium oxide layer gets fluxed and loses its protective nature. Degradation of the material starts, manifesting itself as a loss in weight. It is often considered that extent of initiation phase is the safe regime for deploying the material in service facing such hot corrosion conditions. If the corrosive environment is more aggressive, the initiation phase may get reduced and propagation phase may take off earlier. For example, compared to simulated coal ash environment, (simulated coal ash + flue gas) environment is more aggressive; in the latter environment, initiation phase was found to be shorter, propagation phase taking off earlier [23]. **Figure 1** schematically illustrates these issues.

7.2. Effect of chemical composition

7.2.1. Effect of chromium level

Gagliano et al. [26] carried out studies on 19 alloys varying in chromium content from 16 to 44% and concluded that material's resistance to coal ash corrosion is primarily dependent on chromium content, with alloys containing greater than 22% chromium generally exhibiting satisfactory corrosion resistance. According to the rule of thumb in boiler construction industry, with increasing chromium content in the alloy matrix, lower corrosion rates are expected due to higher ability of sufficient diffusion barrier formation [27]. Based on hot corrosion studies carried out on a number of special steels and superalloys, it was observed that weight loss due to hot corrosion decreases with increasing chromium content. This is shown schematically in **Figure 2**. This tendency appears to be true for iron-based austenitic alloys, as confirmed within the COORETEC study [28, 29]. But for nickel-based austenitic alloys, this tendency cannot be confirmed when SO_2/SO_3-rich atmospheres were present. Both grades 617 and 263 have similar chromium content; however, they perform very differently in SO_2/SO_3-rich environment. Even though chromium content of alloy 617 is high lying at 22%, the oxide scale is apparently not capable of forming a diffusion barrier tight enough to protect metal against sulfur-induced corrosion [18].

7.2.2. Effect of cobalt

Cobalt is less resistant to hot corrosion than nickel. Nickel-based alloys are in general more resistant to low-temperature hot corrosion than cobalt-based alloys. For example, Tiwari [30] studied the relative hot corrosion behavior of a nickel-based superalloy and a cobalt-based superalloy in Na_2SO_4-60% V_2O_5 environment at 900°C and reported that the latter had inferior corrosion resistance.

Zhao et al. [15] reported the hot corrosion reaction in superalloy 740 propagated by the outward migration of Cu and the inward migration of SO_3. With the progressive formation of

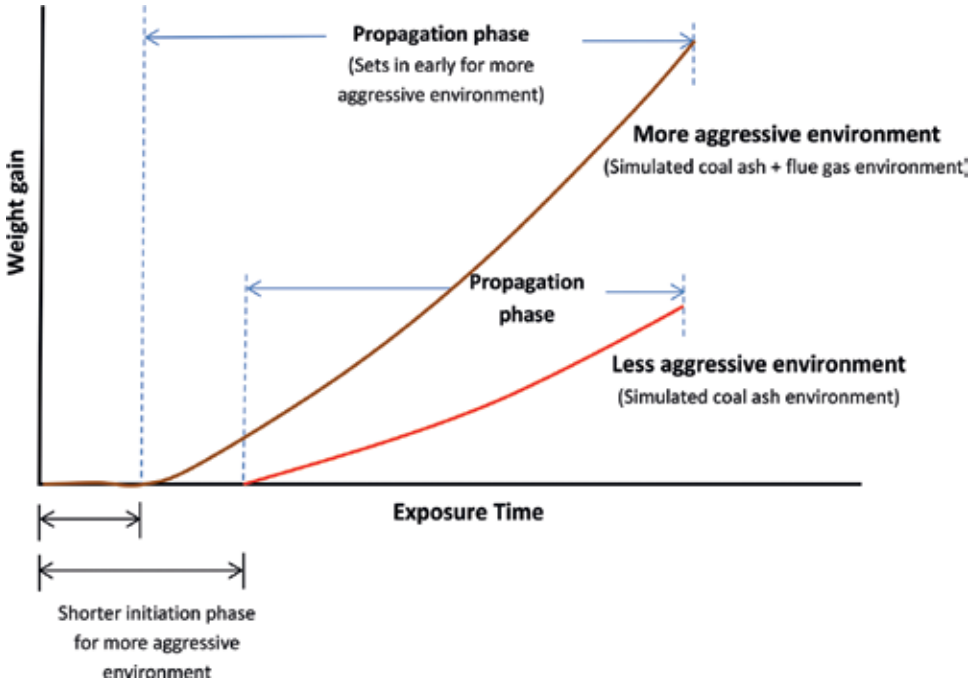

Figure 1. Schematic showing the initiation and propagation phases in the hot corrosion process.

Cr_2O_3 scale, there is an increase in Cr-depletion and enrichment of Co and Ni in the layers immediately below the scale. Due to the high diffusivity of Co in the scale, CoO forms on the exterior of the scale. CoO is surrounded by Cr_2O_3, and the solid-state reaction occurs to form $CoCr_2O_4$ spinel in the outer of the scale gradually. CoO forming on the surface layer reacts with SO_3 to form $CoSO_4$. Even though NiO may form on the surface and $NiSO_4$ formation could result through the reaction of NiO and SO_3, it is believed that $CoSO_4$ forms preferentially due to the fact that $CoSO_4$ is much more stable thermodynamically than $NiSO_4$. The dissolution of Co and CoO induces severe low-temperature hot corrosion. It may be noted in this context that some candidate superalloy grades have considerable Co level in the chemical composition. For example, superalloy 740 has as much as 19–20 wt% Co, and alloy 617 has 10–11 wt% Co. Zhao et al. [15] suggested that a decrease in Co level of the superalloy 740 will act in a beneficial way to resist coal ash/flue gas corrosion. Further studies are required to evaluate the effect of a decrease in the level of Co on the hot corrosion behavior of alloy 740.

7.2.3. Effect of molybdenum

Catastrophic or self-sustaining rapid hot corrosion can occur in superalloys, which contain molybdenum because molybdenum oxide can react with Na_2SO_4 in the salt [31]. The effect of Mo on hot corrosion of superalloys was reported [32–35]. The alloy containing Mo suffers catastrophic degradation. It is reported that MoO_2 reacts with Na_2SO_4 to produce an acid salt (SO_2-rich), leading to acidic fluxing. The MoO_3 may get incorporated into the Na_2SO_4 via the formation of complex compounds such as Na_2MoO_4, $Na_2MoO_4.MoO_3$, and $Na_2MoO_4.2MoO_4$.

All these phases are liquid and have a high solubility of Al_2O_3 and Cr_2O_3. It may be noted in this context that some of the candidate superalloys have significant levels of Mo. For example, alloy 617 has as much as ~9 wt% Mo in its chemical composition.

7.3. Effect of temperature

Operating temperature is one of the important factors that influence sulfidation tendency in coal ash hot corrosion of nickel-based superalloys [5]. A high sulfidation tendency can be observed at low temperatures due to the formation of low-melting alkali sulfate eutectic mixtures [5]. This is the reason why Ni-based superalloys suffer rapid degradation in the temperature range of the so-called Type II hot corrosion. But, the sulfidation tendency decreases at the high-temperature form of hot corrosion, in the temperature of the so-called Type I hot corrosion. Extent of hot corrosion of Inconel 740 was found to be an important function of the temperature in the temperature range of 700–800°C studied by the authors. The corrosion rate was well in the acceptable range at 700°C. There was a 10-fold increase in the rate on increasing the temperature to 750°C, and this was associated with large-scale internal sulfidation and TiS formation. The corrosion rate at 800°C was lower than at 750°C, and the extent of TiS formation was also lower than at 750°C.

The course of corrosion reaction can change with operating temperature. For Ni-XCr-10Al alloy, corrosion follows a multistage parabolic rate law at 700°C, but it changes to a quasiparabolic rate at 800°C [36].

Zhao et al. [15] studied the hot corrosion of alloy 740 at 550 and 700°C. Molten sulfate-induced hot corrosion did not occur at 550°C since the sulfates on the coal ash do not melt at this

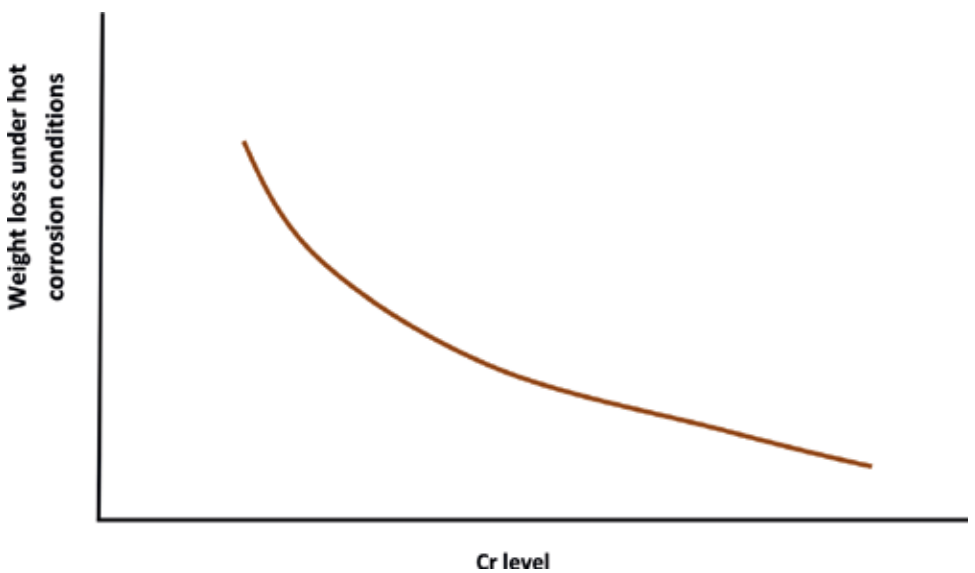

Figure 2. Schematic of the dependence of weight loss due to hot corrosion at 650°C on Cr content based on data obtained for various special steels and superalloys.

temperature. At 700°C, due to the formation of low-melting point eutectic, molten sulfates form and cause accelerated attack after about 1000 h of exposure. No internal sulfidation occurred at 550°C, while sulfides precipitated at scale/alloy interface and in Cr-depletion zone at 700°C. The spinel phases occur in corrosion product at 700°C, while at 550°C that was not the case.

7.4. Effect of aggressive species in the environment

The type and extent of hot corrosion are a function of the composition of flue gas, particularly its SO_2 content [19]. It has been demonstrated that the extent of hot corrosion of Inconel 740 in the flue gas with SO_2 was higher than that in the flue gas without SO_2 [19]. The extent of sulfidation attack was much higher in the flue gas with SO_2. SO_2 in flue gas accelerated the corrosion damage of the alloy in coal ash environment. The metal loss was found to be doubled after 123 h of exposure on switching over from flue gas without SO_2 to flue gas with 1% SO_2. The sulfidation was predominant in the propagation stage.

8. Conclusion

The subject of hot corrosion of superalloys in coal-fired boilers in advanced power plants is a highly complex phenomenon, with a large multiplicity of variables coming into picture. The chemical composition of the alloy plays an important role in this context. High levels of cobalt and molybdenum may have a detrimental effect. While high levels of chromium were found to be useful in combating hot corrosion, a simple relationship between chromium level and resistance to hot corrosion does not seem to hold good when environments contain sulfur-bearing species. Clearly, further work is warranted to optimize the chemical composition to combat hot corrosion while maintaining the stress rupture strength and microstructural stability over long periods of power plant operation. Increasing levels of sulfur-bearing species in the environment increase the extent of sulfidation and susceptibility to hot corrosion. Temperature is also an important parameter in influencing the hot corrosion process; the progress of corrosion reaction and the phases present in the corrosion product could be very different, depending on the reaction temperatures.

Author details

Nageswara Rao Muktinutalapati[1], Arivazhagan Natarajan[1] and Moganraj Arivarasu[2]

*Address all correspondence to: m.nageswararao@vit.ac.in

1 School of Mechanical Engineering, Vellore Institute of Technology, Vellore, India

2 Center for Innovative Manufacturing Research, Vellore Institute of Technology, Vellore, India

References

[1] Natesan K, Park JH. Fireside and steamside corrosion of alloys for USC plants. International Journal of Hydrogen Energy. 2007;**32**:3689-3697

[2] Viswanathan R, Henry JF, Tanzosh J, Stanko G, Shingledecker J, Vitalis B, Purgert R. US program on materials technology for ultra-supercritical coal power plants. Journal of Materials Engineering and Performance. 2005;**14**:281-292

[3] Alcock CB, Hocking MG, Zador S. The corrosion of Ni in O^{2+} SO_2 atmospheres in the temperature range 500-750°C. Corrosion Science. 1969;**9**:111IN7121-120IN9122

[4] Sivakumar R, Sagar PK, Bhatia ML. On the electrochemical nature of hot-corrosion attack in Ni-Cr alloys. Oxidation of Metals. 1985;**24**:315-330

[5] Aung NN, Liu X. Effect of temperature on coal ash hot corrosion resistance of Inconel 740 superalloy. Corrosion Science. 2014;**82**:227-238

[6] Smith GD, Sizek HW. Corrosion 2000. Houston: NACE International; 2000. p. 256

[7] Castello P. Laboratory-simulated fuel-ash corrosion of superheater tubes in coal-fired ultra-supercritical-boilers. Materials and Corrosion. 2000;**51**:786-790

[8] Tan X et al. Supercritical and ultra-supercritical coal-fired power generation. Washington Institute of China Studies, Spring; 2012;**6**(1):53-72

[9] Technical Data Sheet of Special Metals. Available from: http://www.specialmetalswiggin.co.uk/products/inconel-alloy-740 [Accessed: Aug 1, 2017]

[10] Technical Data Sheet of Special Metals. Available from: http://www.specialmetals.com/assets/smc/documents/alloys/inconel/inconel-alloy-740-h.pdf [Accessed: Aug 1, 2017]

[11] Technical Data Sheet of Special Metals. Available from: http://www.specialmetalswiggin.co.uk/products/inconel-alloy-617 [Accessed: Aug 1, 2017]

[12] Technical Data Sheet of Haynes International. Available from: http://haynesintl.com/docs/default-source/pdfs/new-alloy-brochures/high-temperature-alloys/brochures/230-brochure.pdf [Accessed: Aug 1, 2017]

[13] Technical Data Sheet of Haynes International. Available from: http://haynesintl.com/docs/default-source/pdfs/new-alloy-brochures/high-temperature-alloys/brochures/282-brochure.pdf?sfvrsn=20 [Accessed: Aug 1, 2017]

[14] Technical Data Sheet of Special Metals. Available from: http://www.specialmetalswiggin.co.uk/pdfs/products/NIMONIC%20alloy%20263.pdf [Accessed: Aug 1, 2017]

[15] Zhao S, Xie X, Smith GD, Patel SJ. The corrosion of Inconel alloy 740 in simulated environments for pulverized coal-fired boiler. Materials Chemistry and Physics. 2005;**90**(2): 275-281

[16] Zhao S, Xie X, Smith GD, Patel SJ. Research and improvement on structure stability and corrosion resistance of nickel-base superalloy Inconel alloy 740. Materials & Design. 2006;**27**(10):1120-1127

[17] Patel SJ, Baker BA, Gollihue RD. Nickel base superalloys for next generation coal fired AUSC power plants. Procedia Engineering. 2013;**55**:246-252

[18] Stein-Brzozowska G, Flórez DM, Maier J, Scheffknecht G. Nickel-base superalloys for ultra-supercritical coal-fired power plants: Fireside corrosion. Laboratory studies and power plant exposures. Fuel. 2013;**108**:521-533

[19] Aung NN, Liu X. Effect of SO_2 in flue gas on coal ash hot corrosion of Inconel 740 alloy—A high temperature electrochemical sensor study. Corrosion Science. 2013;**76**:390-402

[20] Weitzel PS. A steam generator for 700°C to 760°C advanced ultra-supercritical design and plant arrangement: What stays the same and what needs to change. In: The Seventh International Conference on Advances in Materials Technology for Fossil Power Plants; Waikoloa, Hawaii. October 2013

[21] Kruger KL. Haynes 282 alloy. In: Gianfrancesco AD, editor. Materials for Ultra-Supercritical and Advanced Ultra-Supercritical Power Plants. Woodhead Publishing Series in Energy: Number 104, Amsterdam: Elsevier; 2017. pp. 511-546

[22] Klower J. Alloy 617 and derivatives. In: Gianfrancesco AD, editor. Materials for Ultra-Supercritical and Advanced Ultra-Supercritical Power Plants. Woodhead Publishing Series in Energy: Number 104, Amsterdam: Elsevier; 2017. pp. 547-570

[23] Hari PR, Arivazhagan N, Rao MN, Pavan AHV. Hot corrosion studies on alloy 617 OCC in the context of its use in advanced ultra-supercritical (A-USC) power plants. Transactions of the Indian Institute of Metals. 2017;**70**(3):775-781

[24] Natesan A, Purohit, Rink DL. Coal-ash corrosion of alloys for combustion power plants. A technical report for U.S. Department of Energy, under Contract W–31-109–Eng–38; 2003

[25] Masuyama F. History of power plants and progress in heat resistant steels. ISIJ International. 2001;**41**:612-625

[26] Gagliano M, Hack H, Stanko G. Update on the fireside corrosion resistance of proposed advanced ultrasupercritical superheater and reheater materials: laboratory and field test results. In: The 34th clear conference on coal utilization and fuel systems, Clearwater, FL, USA; 31.05-04.06.2009

[27] Khanna AS. Introduction to High Temperature Oxidation and Corrosion. Materials Park, OH: ASM international. 2002

[28] Stein-Brzozowska G, Flórez DM, Maier J, Scheffknecht G. Fireside corrosion of dedicated austenitic steels in ultra-supercritical coal-fired power plants. In: 37th International Technical Conference on Clean Coal and Fuel Systems, Clearwater, FL, USA; June 3-8, 2012

[29] Scheffknecht G, Maier J, Stein-Brzozowska G, Lemp O, Babat S, Miller E, Schnell U, Neuwirth A. COORETEC projekt abschlussbericht IFK. Grundlegende experimentelle untersuchungen zur belagsbildung und korrosion von neuen werkstoffen im 700°C-dampfkraftwerk. Förderkennzeichen: 0327744E. Förderzeitraum: 2011

[30] Tiwari SN. Investigations on Hot Corrosion of Some Fe-, Ni- and Co-Base Superalloy in Na2SO4-V2O5 Environment under Cyclic Conditions. Ph. D. Thesis Roorkee, India: Metallurgical and Materials EngineeringDepartment, UOR; 1997

[31] Sidhu TS, Agrawal RD, Prakash S. Hot corrosion of some superalloys and role of high-velocity oxy-fuel spray coatings—A review. Surface and Coatings Technology. 2005;**198**:441-446

[32] Pettit FS. Oxidation and Hot Corrosion of Superalloys. Warrendale, PA: The Metal Society AIME; 1984. p. 651

[33] Misra AK. Mechanism of Na_2SO_4-induced corrosion of molybdenum containing nickel-base superalloys at high temperatures I. Corrosion in atmospheres containing only. Journal of the Electrochemical Society. 1986;**133**:1029-1038

[34] Peters KR, Whittle DP, Stringer J. Oxidation and hot corrosion of nickel-based alloys containing molybdenum. Corrosion Science. 1976;**16**:791IN1797-796IN11804

[35] Fryburg GC, Kohl FJ, Stearns CA. Chemical reactions involved in the initiation of hot corrosion of IN-738. Journal of the Electrochemical Society. 1984;**131**:2985-2997

[36] Lanying LU, Taijun PAN, Yan NIU. Oxidizing–sulfidizing corrosion of Ni–xCr–10Al alloys at 700-800°C. Acta Metallurgica Sinica. 2011;**47**:1026-1031

Chapter 4

Ultrasonic Assisted Machining of Nickel-Based Superalloy Inconel 718

Yongbo Wu, Qiang Wang, Sisi Li and Dong Lu

Additional information is available at the end of the chapter

http://dx.doi.org/10.5772/intechopen.76085

Abstract

Inconel 718 has been widely used in industries because of its excellent mechanical properties. However, the machining process, particularly the turning/grinding, of Inconel 718 is still costly due to high cutting force and heavy tool damage. Fortunately, a promising material removal technique, that is, ultrasonic-assisted turning/grinding (called UAT/UAG for simplicity), could potentially play a great role in the high efficiency precision machining of Inconel 718 due to its excellent features such as smaller turning/grinding force, better surface quality, longer tool working life and lower heat generation. However, few attempts have been done on UAT/UAG of Inconel 718. Therefore, in this work, in order to confirm the feasibility of machining Inconel 718 by UAT/UAG, experimental apparatus/equipment has at first been constructed by installing an ultrasonic cutting-unit/spindle on a NC lathe/surface grinder for UAT/UAG operations, and then experimental investigations have been performed to elucidate the fundamental machining characteristics involving Inconel 718 workpiece including the effects of the ultrasonic vibration and the cutting/grinding speed on the work-surface finish, the machining force and temperature, the chip formation, the tool/wheel wears and so on. The obtained results show that grinding forces and surface roughness were decreased in UAT/UAG.

Keywords: Inconel 718, machining, turning, grinding, ultrasonic vibration, surface roughness, material removal, chip formation

1. Introduction

Inconel 718, a nickel-based superalloy, exhibits desirable properties over a wide temperature range and is widely used in aerospace, petroleum and nuclear industries because of

its excellent mechanical properties such as high fatigue strength, good corrosion resistance and strong creep resistance [1]. In power generation equipment manufacturing industries including gas turbine engines, most of Inconel 718-made products are commonly machined by turning, cutting, milling and grinding. However, the excellent mechanical properties of Inconel 718 are leading to high cutting force, severe work-surface damage and heavy tool wear in conventional machining/finishing processes [2]. Especially, the turning/grinding process (hereinafter called CT/CG for simplicity) of Inconel 718 is still costly due to the heavy and rapid wear of tools.

As a promising material removal technique, ultrasonic-assisted turning/grinding (hereinafter called UAT/UAG for simplicity) has attracted great attention for decades for the sake of its excellent features such as smaller turning/grinding force, higher material removal rate, better surface quality, longer tool working life and lower heat generation compared with those in CT/CG [3–7]. However, in the most of conventional UAT processes, a linear ultrasonic vibration is applied only in a single direction [8–12], which leads to the difficulty in the obtainment of a reasonable material removal rate especially for difficult-machine metal such as Inconel 718. On the other hand, in conventional UAG processes, most of researches have ever focused mainly on the hard-brittle materials such as crystal silicon and ceramics [13–19], and few attempts have been done involving Inconel 718.

Therefore, the present authors proposed a novel UAT technique in which an elliptical ultrasonic vibration generated by the synthesis of two orthogonal linear ultrasonic vibrations is applied on the tool in the base plane and experimentally confirmed its performance in the turning of Inconel 718 [20, 21]. This new method is hereafter called as EUAT. In addition, the UAG of Inconel 718 in which a linear ultrasonic vibration is imposed to the grinding wheel along the wheel axis was also attempted, and some significant results were attained [22, 23]. In this chapter, the processing principles of EUAT/UAG and the respective corresponding apparatuses are described. Then, the fundamental machining characteristics obtained are detailed.

2. Elliptical ultrasonic-assisted turning of Inconel 718

2.1. Processing principle and apparatus

The processing principle of elliptical ultrasonic-assisted turning (EUAT) is as illustrated in **Figure 1**; an elliptical ultrasonic vibration is imposed on the cutting tool in the base plane (XOY plane) and the workpiece is rotated at a speed n_w around its own axis (X-axis) in addition to a feed motion of the cutting tool in X-direction at a feed rate v_f and a depth of cut a_p. The elliptical ultrasonic vibration is achieved by the synthesis of two vibrations in X- and Y-directions with the respective amplitudes of A_x and A_y generated simultaneously by the ultrasonic vibration unit.

For realizing the processing principle, an experimental apparatus was constructed by installing a commercial ultrasonic vibration unit (UL40-A1 by Takesho Co., Ltd.) onto the

http://dx.doi.org/10.5772/intechopen.76085

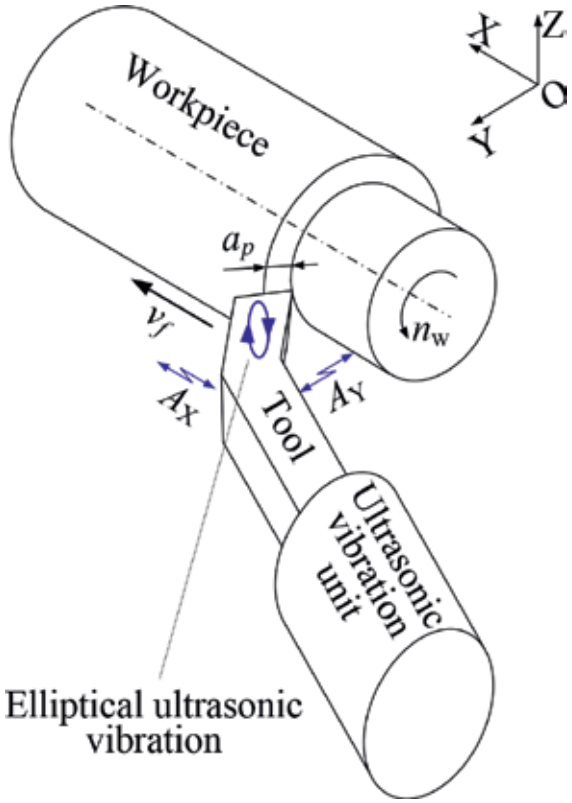

Figure 1. Processing principle of EUAT.

tool post of a commercial CNC lathe (TAC-360 by Takizawa Co., Ltd.) as shown in **Figure 2**. A power supplier was used to apply an AC voltage into the ultrasonic unit for inducing the ultrasonic vibration. A commercial dynamometer was fixed below the ultrasonic unit to measure the cutting forces. As the tool, a coated carbide insert, which is installed at the tip of the ultrasonic unit, was employed. The cutting temperature was measured using an infrared camera.

For quantitatively confirming the generation of elliptical vibration, the vibrations of tool cutting edge in *X*- and *Y*-directions were simultaneously measured by two laser Doppler vibrometers (LV-1610; Ono Sokki Co., Ltd.). The frequency of the AC voltage was set at 40.9 kHz, based on the given specification of the ultrasonic unit. **Figure 3** plots the vibration amplitudes of the tool cutting edge, A_x in X-direction and A_y in Y-direction, at different power supplying levels. It is evident that as the power supplying increases, the values of A_x and A_y increase linearly to 2.35 and 2.05 μm, respectively, at the power level of 40%. Using the vibrations measured in both directions, the trajectory of the tool cutting edge was captured by an oscilloscope (WaveJet 314; LeCroy Co., Ltd), and the obtained trajectories for different power supplying levels were also exhibited in **Figure 3**. Clearly, the tool cutting edge follows a clockwise elliptic motion, and the

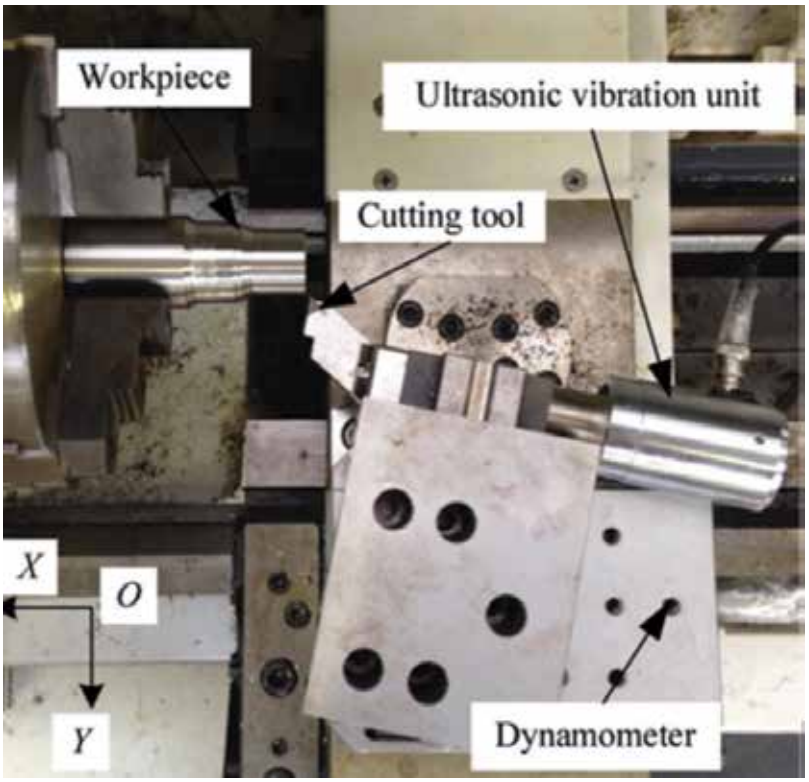

Figure 2. Apparatus for EUAT.

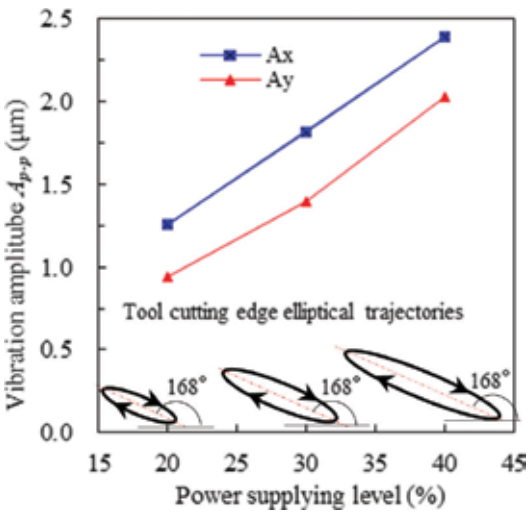

Figure 3. Effect of power supplying level on vibration amplitude.

shape of ellipse remains essentially unchanged with a declined angle of 168° even the power supplying level varied, but the size of trajectory increased as the power supplying level escalated.

2.2. Machining conditions and procedure

Table 1 summarizes the machining conditions in experiments. As the workpiece, an Inconel 718 rod with the dimension of 40 mm in diameter and 100 mm in length was used. The cutting speed v_c was hence changed from 75 m/min to 125 m/min when the workpiece rotational speed n_w was adjusted from 600 to 1000 rpm. During machining, the cutting forces and the cutting temperature were measured using the three-component dynamometer and the infrared camera, respectively. After machining, the work-surface roughness was evaluated by using a surface profiler (Talysurf Intra by Taylor Hobson Inc.), and the surface morphology of workpiece was captured by using a laser microscope (VK-8710 by Keyence Co., Ltd). In addition, for comparison, the conventional turning (CT) operations were also conducted on the same experimental apparatus but turned off the power supplier to set the power supplying level at 0%, that is, $A_x = A_y = 0$.

2.3. Fundamental machining characteristics

Cutting force and temperature. In order to confirm that the ultrasonic vibration-reducing effect of cutting force (UREF) still exists in the high speed cutting of Inconel 718 when EUAT is performed in the base plane, the effect of cutting speed on cutting force in CT and EUAT was studied by experiments. The results are presented in **Figure 4**, demonstrating that in comparison with CT with EUAT, when the cutting speed was 75 m/min, the feed force F_x, the radial force F_y and the cutting force F_z were reduced by 38%, 46% and 25%, respectively. Similarly, even the cutting speed was increased to 87.5 m/min, then 100 m/min, further 112.5 m/min and finally 125 m/min, similar reduction percentages were observed on the F_x, F_y and F_z with those at 75 m/min.

In other words, even when the cutting speed goes beyond the maximum ultrasonic vibration velocity of $\pi f A_{p\text{-}p}$, UREF is barely affected by the increase in the cutting speed. This may be

Workpiece	Inconel 718 (φ 40 mm × L 100 mm)
Cutting tool	Coated carbide
	Normal rake angle $\alpha = 0$ (°)
	Normal clearance angle $\gamma = 11$ (°)
	Nose radius $r_n = 0.4$ rn(mm)
Cutting parameters	$n_w = 600$–1000 (rpm) ($v_c = 75$–125 m/min), $v_f = 0.05$ (mm/rev), $a_p = 0.05$ (mm)
Ultrasonic vibration	In CT: $A_x = A_y = 0$
	In EUAT: $f = 40.9$ kHz, $A_x = 2.07$ μm, $A_y = 2.81$ μm, declined angle: 168°
Coolant	Dry cutting

Table 1. Machining conditions in EUAT of Inconel 718.

because the ultrasonic separation exists between the tool nose and the workpiece in X- and Y-directions in the base plane, respectively, in EUAT. In addition, in both CT and EUAT, the largest force was F_y, followed by F_x and F_z in descending order [24].

The cutting temperatures at different cutting speeds in CT and EUAT were also obtained as shown in **Figure 5**. The results demonstrated that either in CT or in EUAT, as the cutting speed increased, the cutting temperature rose monotonously; however, the increase rate in EUAT seemed consistently lower than that in CT, indicating the ultrasonic vibration significantly contributed to the reduction of cutting temperature in turning Inconel 718.

Chip morphology. Figure 6 shows that the chip width in EUAT is smaller than that in CT, indicating that the chip morphology is affected by the cutting forces; the increase in cutting force adds the transverse flow of the material, leading to an increase in the chip width [25]. Moreover, the adhesion of microchips can be observed evidently on the chip surface in CT, which can hardly be seen in EUAT. These phenomena may be connected to the formation of BUE (built-up edge) during cutting, which will be discussed in the "Tool Wear" section.

Work-surface finish. The surface morphologies of workpieces machined by CT and EUAT at three different cutting speeds of 75, 100 and 125 m/min were captured by the laser microscope. From the microscopic images shown in **Figure 7(a)**, it is found that regardless of the cutting speed, obvious parallel cutting traces and randomly distributed pits can be observed on the work-surface in CT; the phenomena may be attributed to the formation of BUE on the cutting tool and chip winding during cutting. By contrast, in EUAT (**Figure 7(b)**), knitted work-like texture was formed on the work-surface owing to the tool vibration, and the work-surface integrity became better. This is probably attributed to the fact that the chips were no longer wrapped around workpiece and easily broken for the sake of the elliptical vibration of cutting tool in the base plane.

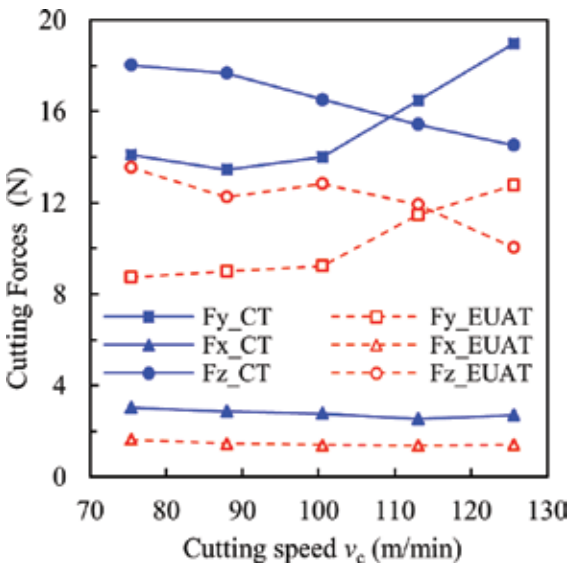

Figure 4. Effect of cutting speed on cutting forces.

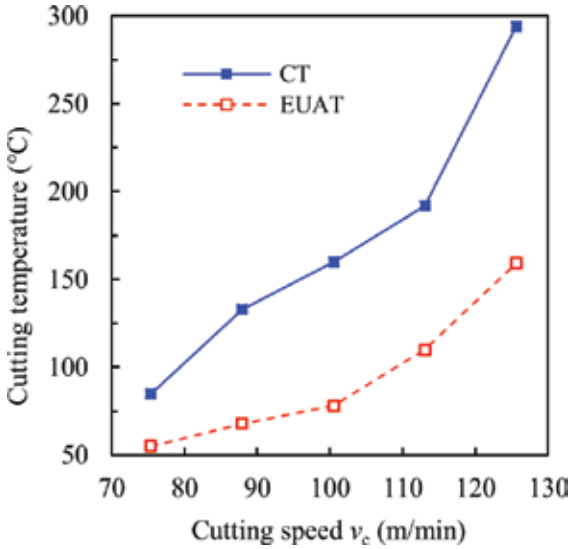

Figure 5. Effect of cutting speed on cutting temperatures.

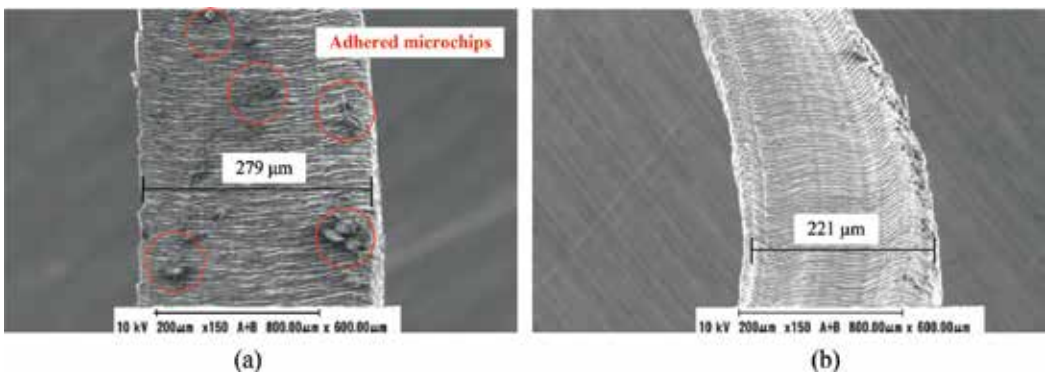

Figure 6. SEM micrographs of chips developed in CT and EUAT methods: (a) in CT and (b) in EUAT.

The work-surface roughness was measured in the feed direction using the surface profiler for both CT and EUAT. The evaluation length was set to 5 mm. In each test, the surface roughness parameters R_a and R_z were measured eight times, and their average values were calculated and regarded as the roughness. **Figure 8** shows the effect of the cutting speed on the work-surface roughness in CT and EUAT at three different cutting speeds of 75, 100 and 125 m/min. The surface roughness R_a and R_z in EUAT seemed both larger than those in CT. In EUAT with the increase of cutting speed, the R_a and R_z slightly decreased, while in CT, the R_a and R_z tended to increase slightly which is caused by the formation of built-up edge (BUE) on tool cutting edge [20].

Tool wear. Figure 9(a) and **(b)** shows the SEM images of the cutting edge of tool employed for 4.2 min in CT and EUAT, respectively. Evidently, in CT, the BUE appeared on the cutting

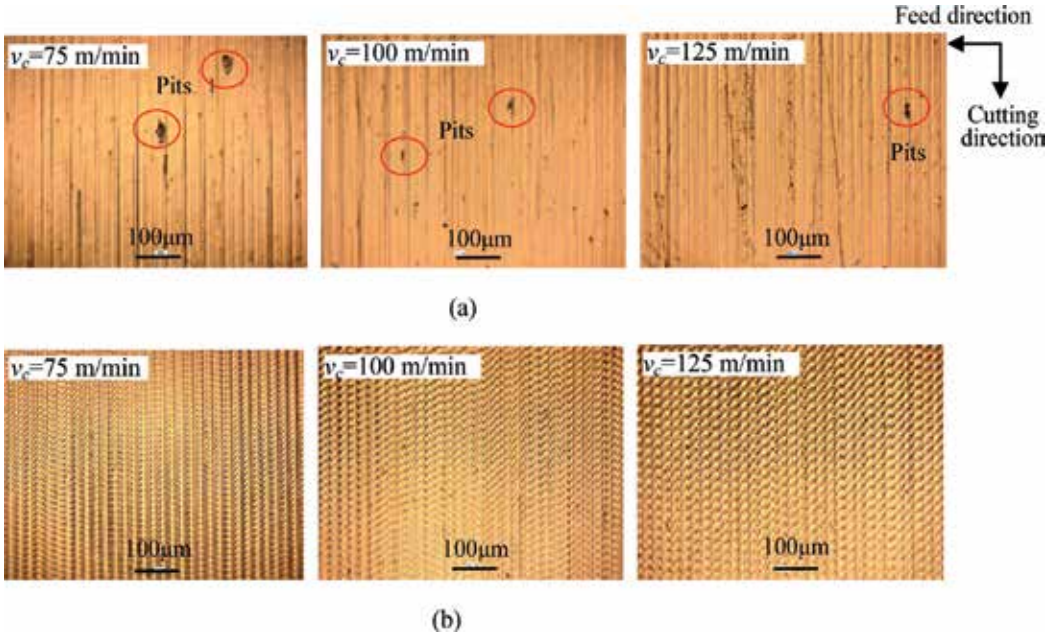

Figure 7. 2D laser microscopic images of the work-surfaces machined: (a) in CT and (b) in EUAT.

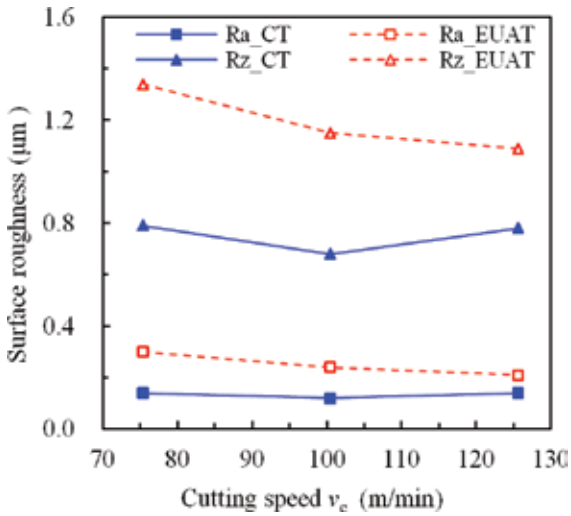

Figure 8. Effect of cutting speed on work-surface roughness.

tool, whereas in EUAT, it was absent. Comparing **Figure 9(a)** with **Figure 9(b)** shows that the cutting tool adopted in CT experienced considerably heavier flank wear than that adopted in EUAT. The maximum flank wears in CT and EUAT were 0.23 and 0.19 mm, respectively. This indicates that the cutting tool was worn down more rapidly in CT than in EUAT, possibly because the tool vibration in EUAT reduces the friction between the tool and the workpiece. In EUAT, the ultrasonic vibration of tool occurs simultaneously in X- and Y-directions and

http://dx.doi.org/10.5772/intechopen.76085

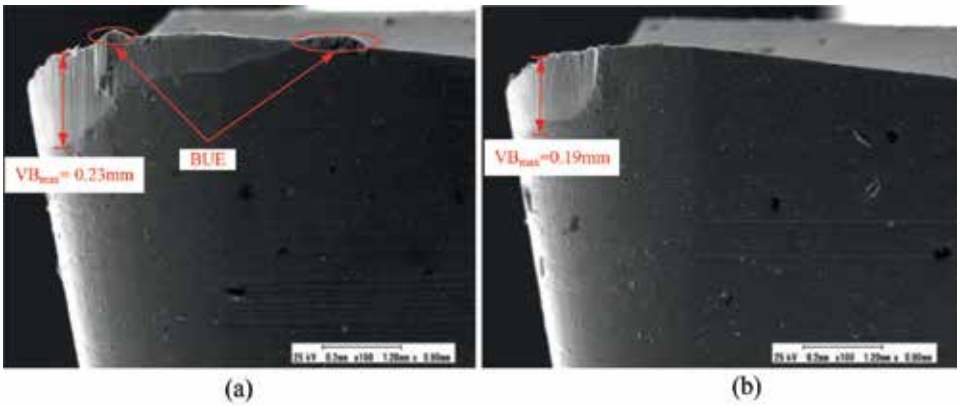

Figure 9. SEM images of cutting tools used in (a) CT and (b) EUAT for 4.2 min (power supply level = 20%).

results in a clockwise elliptical motion in the base plane (see **Figure 1**). During cutting, owing to the elliptic vibration the tool repeats the cutting-in and cutting-out action periodically. This action reduces the formation of BUE and eventually retains the sharpness of the tool cutting edge. Therefore, the chips and the work-surface in EUAT are almost free of chip particles.

3. Ultrasonic-assisted grinding of Inconel 718

3.1. Processing principle and equipment

The processing principle of UAG is illustrated in **Figure 10**; an axial ultrasonic vibration is imposed on the grinding wheel in x-direction and the workpiece is fixed on a work-holder under which a z-stage is located for determining the wheel depth of cut Δ. The peripheral speed of grinding wheel is V_c and a feed motion is given to the workpiece in y-direction. For comparison, a conventional grinding (CG) was also performed by releasing spindle from ultrasonic vibration (**Figure 11**).

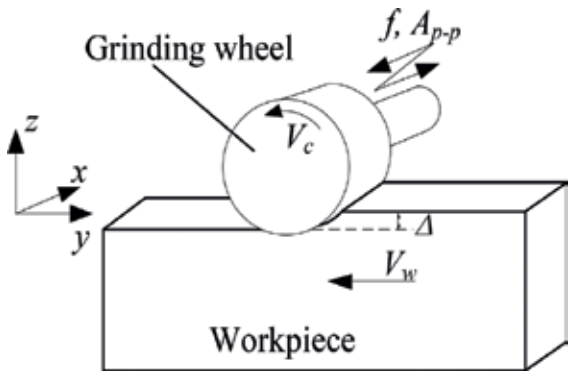

Figure 10. Processing principle of ultrasonic-assisted grinding.

For realizing the processing principle, an experimental apparatus was constructed by installing a commercial ultrasonic vibration spindle (URT40 by Takesho Co., Ltd., Japan) onto a commercial NC grinder (GRIND-X IGM15EX by Okamoto Machine Tool Co., Ltd., Japan). A commercial dynamometer (9256A by Kistler Co., Ltd., Switzerland) was positioned under the ultrasonic spindle. On the lower end of the spindle, a metal-bonded #140 cBN grinding wheel with a diameter of d_s = 8 mm was fixed and an Inconel 718 specimen (L48 mm×W36 mm×T3 mm) was used as the workpiece. The abrasive grains on the working surface of the wheel employed were observed by a three-dimensional (3D) SEM (ERA-8900 by ELIONIX. Co., Ltd., Japan), showing that most of the grains were cone shaped and their vertical angles and average diameter were around 120° and 105 μm, respectively.

3.2. Grinding conditions and procedure

Table 2 exhibits the grinding conditions. As the purpose of this work is predominantly to reveal the fundamental machining characteristics in UAG of Inconel 718 including the effects of the ultrasonic vibration and the wheel peripheral speed on the grinding force and specific

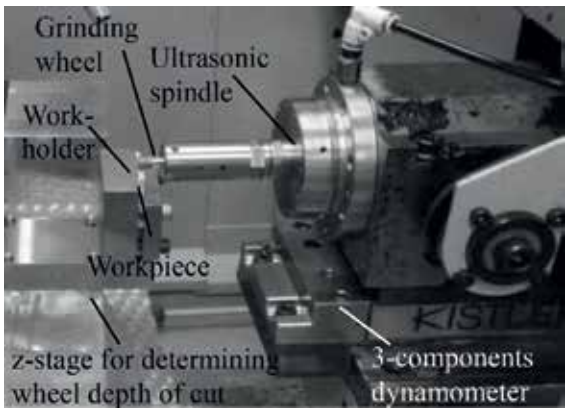

Figure 11. Photo of equipment for ultrasonic-assisted grinding.

Workpiece	Inconel 718, L48 mm × W36 mm × T3 mm
Grinding wheel	Electroplated cBN#140, φ8 × L8 mm (FSK 140)
Ultrasonic vibration	Frequency f = 40 kHz
	Amplitude $A_{P\text{-}P}$ = 0–9.4 μm
Process parameters	Workpiece feed rate V_w = 15 mm/min
	Wheel peripheral speed V_c = 100.5–138.2 m/min (wheel rotational speed n_g = 4000–5500 rpm)
	Grinding width b = 3 mm
	Wheel depth of cut Δ = 80 μm
Coolant	Without (dry grinding)

Table 2. Grinding conditions.

grinding energy, the work-surface finish, the chip formation (chip size and geometry), the material removal rate and the grinding wheel wear, the grinding operations were performed at different ultrasonic vibration amplitudes and wheel peripheral speeds but the constant workpiece feed rate and wheel depth of cut.

Typically, cBN abrasives require a cutting speed of over 50 m/min for grinding Inconel 718 [16]. Therefore, the value of wheel peripheral speed V_c was set at 100.5–138.2 m/min (wheel rotational speed n_g = 4000–5500 rpm). In order to ascertain the benefits from application of the ultrasonic vibration to precision grinding, the workpiece feed rate was set at a low value of 5 mm/min. Correspondingly, a large value of depth of cut is required to ensure material removal rate; hence, the value of Δ was set at 80 μm. The actual vibration amplitude A_{p-p} of the wheel was measured using the Laser Doppler vibrometer (LV-1610 by On Sokki Co., Ltd., Japan), revealing that the value of A_{p-p} was varied in a range of 0–9.4 μm as the power supplying level rises. In addition, dry grinding operations were performed without coolant supplying.

The material removal rate Q was also experimentally obtained using the relationship of $Q = b\Delta_r V_w$, where Δ_r is the actually measured work-depth removed. Furthermore, the ground work-surface roughness was measured with the surface profiler (Talysurf Intra by Taylor Hobson Inc.) to indicate the work-surface finish. For further investigation, the chips used for the SEM observation were those escaped out of the grinding zone during dry grinding and collected by a piece of conductive plastic (4×4 mm), which was located nearby the grinding zone. The working surface condition of grinding wheel, that is, the chips adhesion, the wheel wear behavior like grain releasing/fracture were also examined by SEM observation.

3.3. Fundamental grinding characteristics

Grinding force, specific grinding energy and material removal rate. Figure 12(a) and **(b)** shows the grinding forces measured under various values of A_{p-p} and V_c, respectively. Evidently, either the tangential force F_y or the normal one F_z monotonously decreased as the A_{p-p} increased (**Figure 12(a)**), and almost linearly decreased with the increasing V_c (**Figure 12(b)**). It should be noticed, for example, that at V_c = 138.2 m/min, once the ultrasonic vibration at A_{p-p} = 9.4 μm has been applied, the values of F_y and F_z were dropped by 51.9% and 38.6%, respectively, compared with that without ultrasonic vibration (A_{p-p} = 0 μm). Additionally, considered that the F_z affects tremendously, the formation of micro fracture defects on chip which is characterized by the knife chip, a lower F_z in UAG might lead to a smaller number of knife chips (see **Figures 18** and **19**) compared with that in CG.

In addition, the grinding force ratio of F_z/F_y was obtained as exhibited in **Figure 12**, showing that the ratio increased with the increasing A_{p-p} (**Figure 12(a)**), whereas little effect of the V_c can be observed on the ratio (**Figure 12(b)**) either in CG or in UAG. As revealed by Dong Kun Zhang [26], the lower friction ploughing and smaller chip deformation lead to the increase of grinding force ratio. Therefore, the results demonstrated that ultrasonic vibration contributed to the reduction of friction ploughing and chip deformation. Further, a larger vibration amplitude seemed to increase the material removal ratae, as shown in **Figure 13**. This confirmed that the ultrasonic vibration can enhance the material removal owing to the decrease in grinding forces.

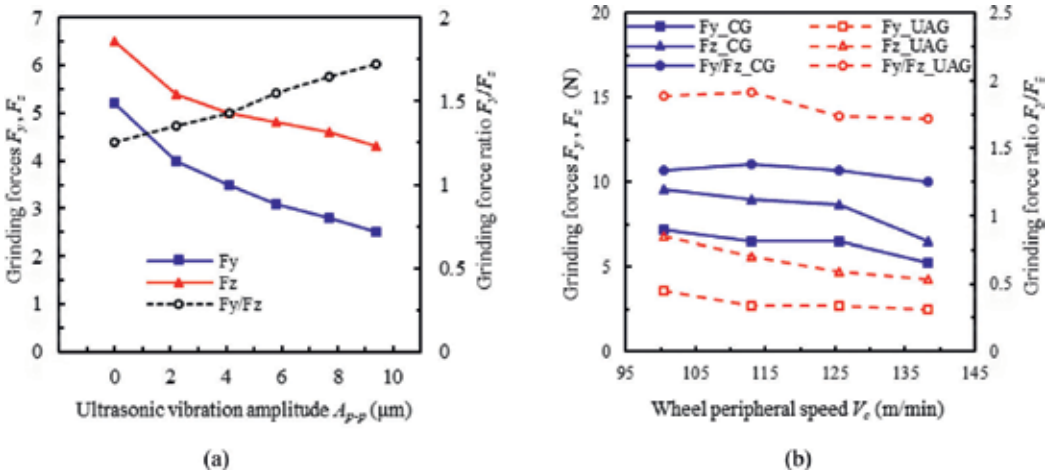

Figure 12. Effects of (a) vibration amplitude and (b) wheel peripheral speed on grinding forces.

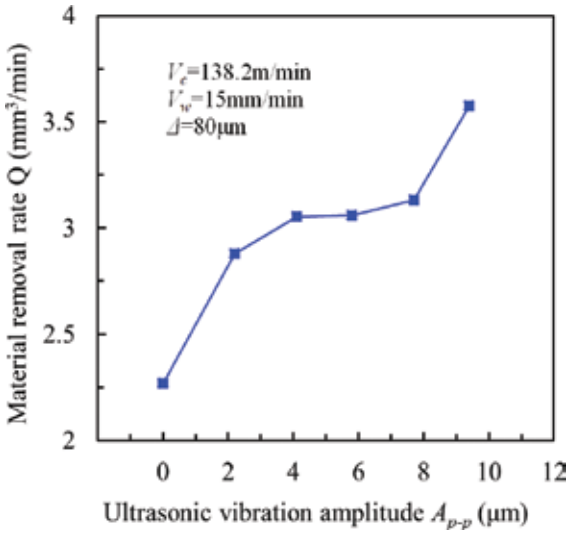

Figure 13. Effects of vibration amplitude on material removal rate.

Furthermore, the specific grinding energy, u, in UAG was compared with that in CG. As the u is defined as the energy per unit volume of material removed [27], it can be expressed in Eq. (1) in CG and Eq. (2) in UAG, respectively.

$$u = F_y V_c / 1000 b \Delta V_w \tag{1}$$

$$u = \left(F_y V_c + F_x V_x\right) / 1000 b \Delta V_w \tag{2}$$

where F_x (N) is the grinding force in x-direction due to the wheel ultrasonic vibration and V_x (m/min) is the wheel ultrasonic vibration speed determined by the equation of

$$V_x(t) = 2\pi f A_{p-p} \cos(2\pi f t) \tag{3}$$

Both of them are varied periodically at the frequency of f during grinding.

In the current work, the values of V_c, b, Δ and V_w have been already known as exhibited in **Table 2** and that of F_y is also the already known one as shown in **Figure 12**. The measured results of F_x and the calculated value of V_x are given in **Table 3**. The F_xV_x changed from 0 to the respective peek values for different A_{p-p}, while the F_yV_c decreased with the increase of A_{p-p}.

Figure 14 shows the relation between u and A_{p-p}. It can be seen from this figure that although the u varied between u_L and u_H at the given A_{p-p} for the sake of the ultrasonic vibration, the u intended to decrease as the A_{p-p} increases, confirming that the ultrasonic vibration benefits the reduction in the specific grinding energy significantly.

Work-surface finish. Given that the effective cutting edge distribution density affects the work-surface roughness in grinding processes and that this density is affected by the ultrasonic vibration [22], it was also investigated how the work-surface finish varied with vibration amplitude A_{p-p}. **Figure 15** shows the obtained results, demonstrating that the ultrasonic

A_{p-p} (mm)	0	2.2×10^{-3}	4.1×10^{-3}	5.8×10^{-3}	7.7×10^{-3}	9.4×10^{-3}
V_x (m/min)	0	−16.6–16.6	−30.9–30.9	−43.7–43.7	−58–58	−71–71
F_x (N)	0	−0.1–0.1	−0.1–0.1	−0.1–0.1	−0.1–0.1	−0.1–0.1
F_xV_x	0	0–1.7	0–3.1	0–4.4	0–5.8	0–7.1
F_yV_c	718.6	552.8	483.7	428.4	387.0	345.5

Table 3. V_x, F_x, F_xV_x and F_yV_c typically obtained at V_c = 138.2 m/min for various values of A_{p-p}.

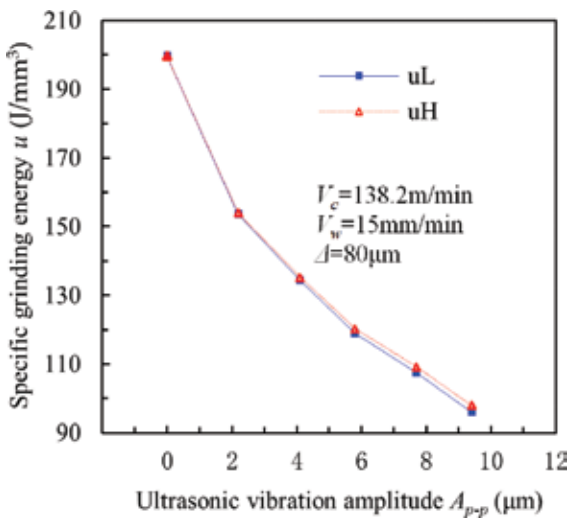

Figure 14. Effect of ultrasonic vibration on specific grinding energy.

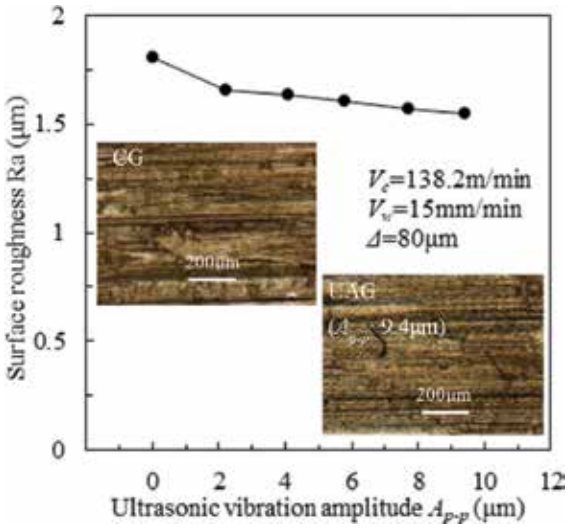

Figure 15. Effect of ultrasonic vibration amplitude on work-surface finish.

vibration indeed contributed to the work-surface finish improvement; the larger the A_{p-p} was, the smaller the work-surface roughness became. The optical microscopic images of work-surfaces in CG and UAG were also compared in the same figure, showing that on the work-surface by CG only parallel grain cutting marks were formed, whereas on that by UAG, many ultrasonic-induced knitting-patterned cutting marks overlap with the parallel ones.

Chips formed. An electron scanning microscope (SEM) with 3D measurement/observation functions (ERA-8900 by ELIONIX Co., Ltd.) was employed to measure the 3D chip size and observe the chip geometry. **Figure 16(a)** and **(b)** shows the 3D SEM images of chips formed in UAG (A_{p-p} = 9.4 μm) and CG at V_c = 138.2 m/min, respectively. The measured results of mean length and cross section area of chips are shown in **Figure 16 (c)** and **(d)**. It is evident in **Figure 16(c)** that the ultrasonic vibration leaded to the reduction of mean length and mean cross section area of chips. Especially, when the amplitude was A_{p-p} = 9.4 μm, the mean length was reduced by 36.3% and the cross section area was reduced by 64.3%. **Figure 16 (d)** shows the effect of the wheel peripheral speed V_c, demonstrating that as the V_c increases the cross section area intends to reduce either with or without ultrasonic vibration, but the effect on the chip length was not obvious.

In conventional grinding of Inconel 718, the formed chip could be classified into six types: flow, shear, rip, knife, slice and melt [28]. In this study, all the six types occurred; however, dominant types were shear, knife and flow either in CG or UAG as shown in **Figure 17**. Further, the number percentages of each type under different conditions were experimentally investigated, and the obtained results (**Figure 18**) show that the majority of chips in CG were shear type, whereas most of them in UAG were flow type especially at larger vibration amplitude ($A_{p-p} \geq 4.1$ μm). This indicates that the UAG of Inconel 718 is potentially avoiding the formation of shear chips and prefers the flow chips especially at larger amplitude.

As for the effect of the wheel peripheral speed V_c, it can be found from **Figure 19** that in CG when the V_c changed from 100.5 m/min to 113 m/min, the percentage of the flow chip

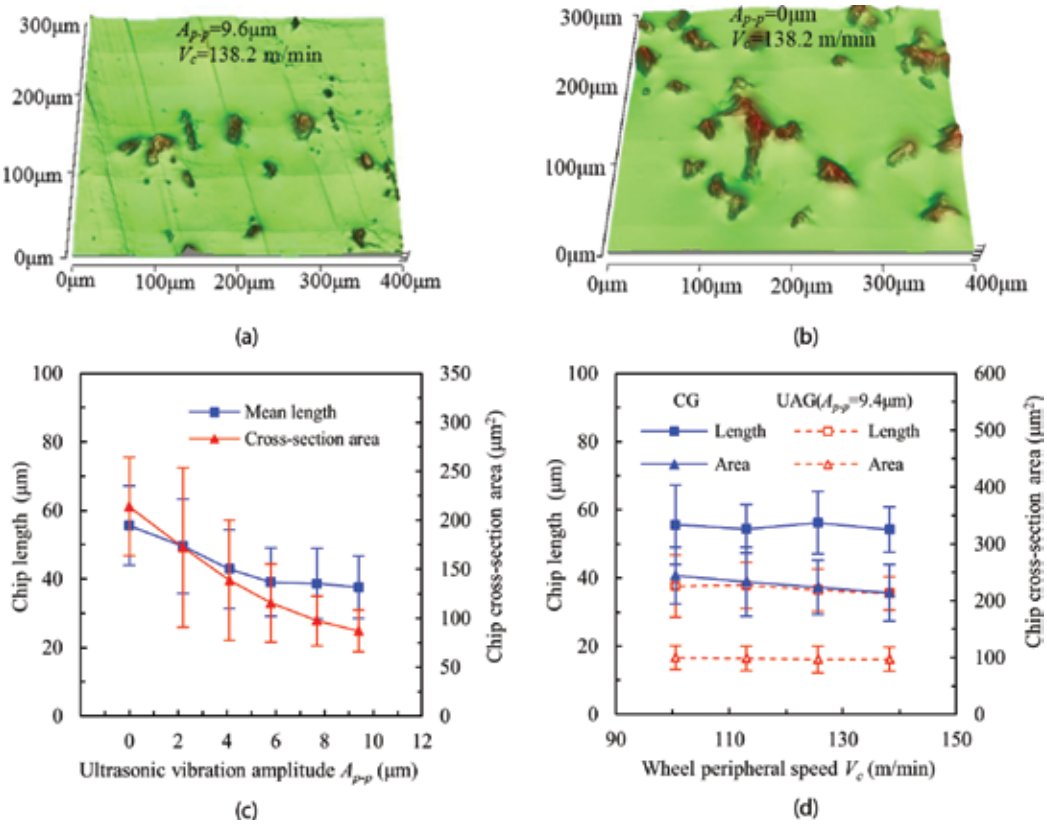

Figure 16. Effects of ultrasonic vibration and wheel peripheral speed on chip size: (a) 3D SEM images of chips in UAG at A_{p-p} = 9.4 μm, (b) 3D SEM images of chips in CG, (c) chip length and cross section area vs. vibration amplitude and (d) chip length and cross section area vs. wheel peripheral speed.

increased from 4 to 63% and the change in the percentage of knife chip was very small, while that of the shear chips reduced from 86 to 30%. As the increase of V_c the number percentage of three types of chips were not obvious. In UAG, the increase of V_c was not main effect to the change of number percentage of chips.

Working surface condition of grinding wheel. Through SEM observation, the working surface morphologies of wheel with/without ultrasonic vibration were captured. From the SEM images shown in **Figure 20**, it is found that both chips adhesion and grains releasing/fracture occurred during grinding. Comparing the right sides of **Figure 20(a)** and **(b)** revealed distinctly that the ultrasonic vibration reduced both the chips adhesion and grains releasing/fracture significantly.

Furthermore, the chips adhesion area was filtered, extracted and binarized by using Image-Pro Plus for quantitative analysis [22]. For this purpose, an observation zone with size of 1.13 mm × 6 mm on grinding wheel working surface was selected to measure the percentage of chips adhesion area in the total wheel working surface area, as shown in **Figure 21**. Obviously, increasing the ultrasonic amplitude leads to the reduction of the percentage of chips adhesion area. Especially, at A_{p-p} = 9.4 μm, a decrease by 72.4% was observed.

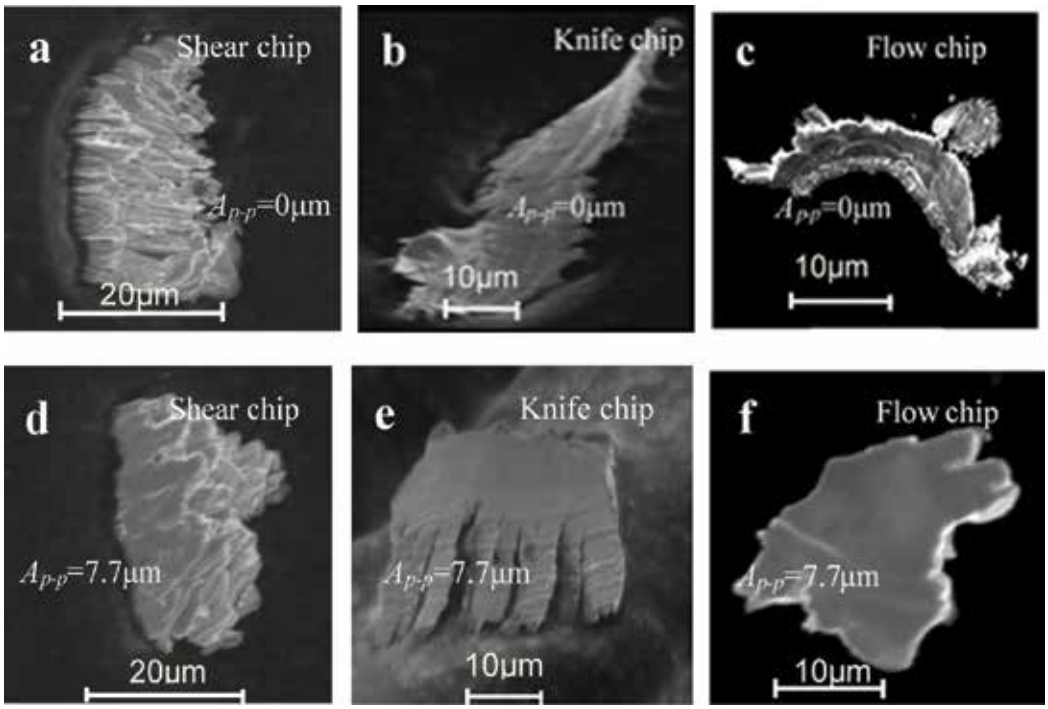

Figure 17. Chips type: (a) shear chip in CG; (b) knife chip in CG; (c) flow chip in CG; (d) shear chip in UAG; (e) knife chip in UAG and (f) flow chip in UAG, at Δ = 80 μm and V_c = 138.2 m/min.

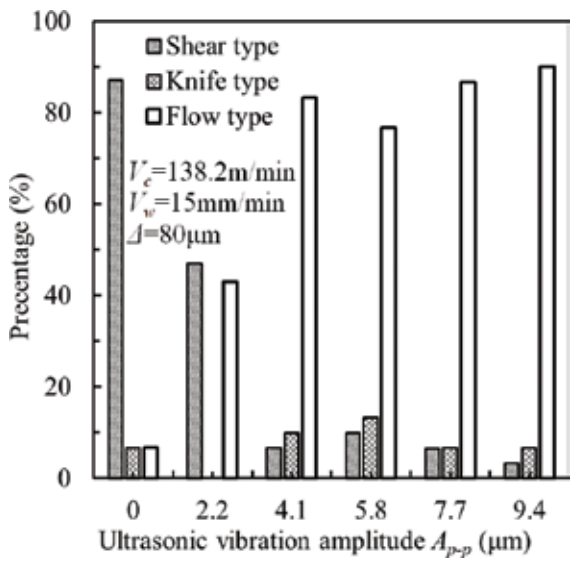

Figure 18. Effect of vibration amplitude on chip type.

http://dx.doi.org/10.5772/intechopen.76085

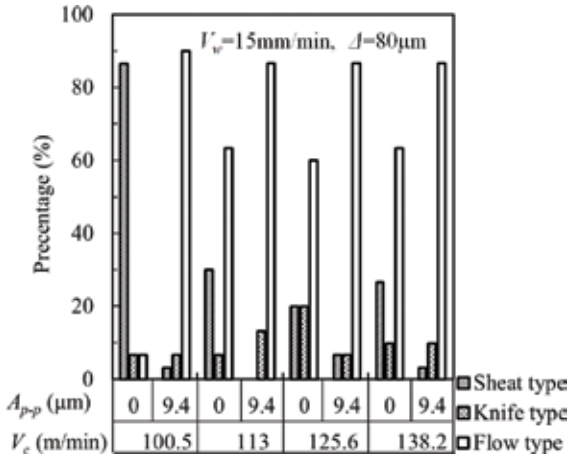

Figure 19. Effect of wheel peripheral speed on chip type.

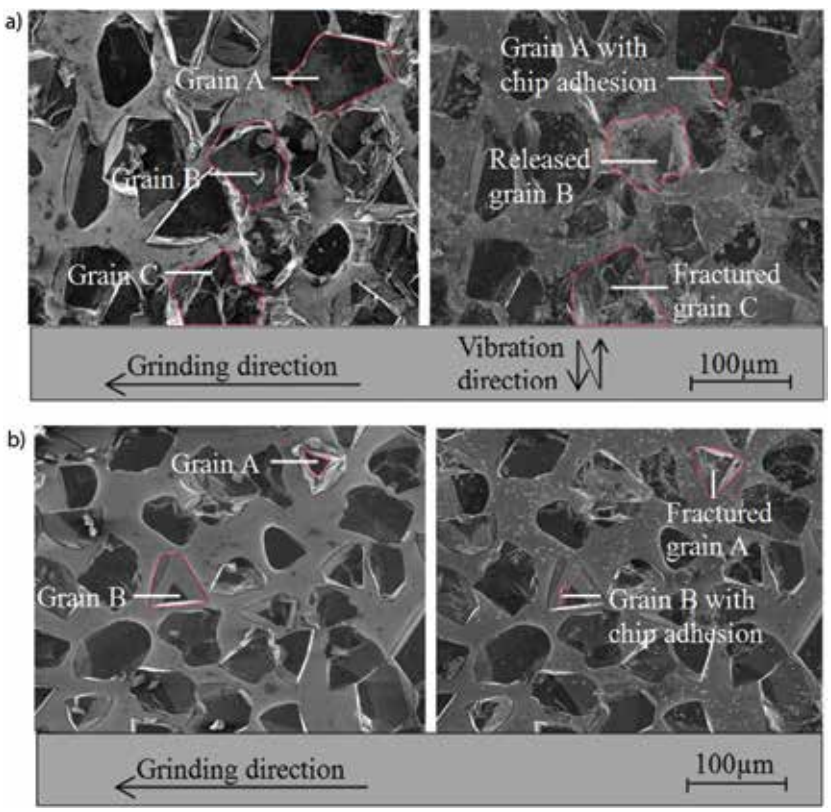

Figure 20. SEM images of the grinding wheel working surfaces before (left sides) /after (right sides) grinding of Inconel 718 (a) without and (b) with ultrasonic vibration: (a) in CG at $A_{p\text{-}p}$ = 0 μm and V_c = 138.2 m/min and (b) in UAG at $A_{p\text{-}p}$ = 9.4 μm and V_c = 138.2 m/min.

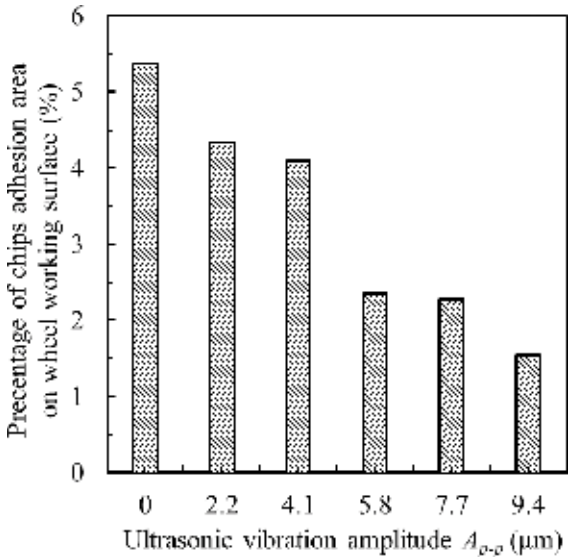

Figure 21. Effects of vibration amplitude on the percentage of chips adhesion area.

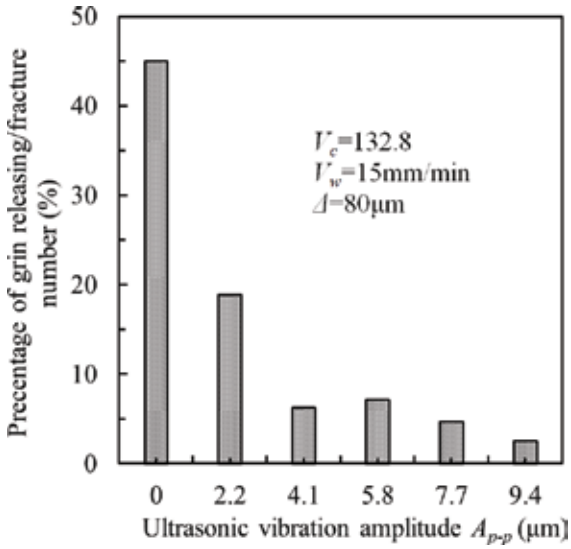

Figure 22. Effect of vibration amplitude on the percentage of grain releasing/fracture number.

At last, the releasing/fracture of abrasive grains was investigated by comparing the percentages of grain releasing/fracture number in total wheel working surface in CG and UAG, as shown in **Figure 22**. It is noticed that in CG (A_{p-p} = 0 μm), the percentage reached 44%. Once an ultrasonic vibration with a small amplitude of A_{p-p} = 2.2 μm has been imposed, the percentage turned to be less than 20%, demonstrating that the presence of ultrasonic vibration restraints

the grain releasing/fracture phenomenon considerably. In addition, when compared the CG result with the UAG one at $A_{p\text{-}p}$ = 9.4 μm, it is figured out that the percentage decreased by 40%. This phenomenon is attributed to the ultrasonic vibration-induced vertical inertia force which acts on chips. This vertical inertia force encourages chips to leave cutting edge and hence increases cutting capacity of grain.

4. Summary

As a step toward the development of a novel technique for the machining of superalloy Inconel 718, at first the elliptic ultrasonic-assisted turning (EUAT) method was proposed and its fundamental performance was experimentally confirmed, then the ultrasonic-assisted grinding of Inconel 718 was attempted and successfully elucidated the fundamental grinding characteristics. The obtained results can be summarized as following.

In EUAT, (1) the cutting force was considerably smaller than that in conventional turning (CT) and strengthening the ultrasonic vibration decreased the cutting force; (2) although ultrasonic vibration marks were formed on the work-surface along the cutting direction, the surface finish was improved, whereas scratches and pits obviously existed on the work-surface in CT and (3) the ultrasonic vibration significantly restrained the formation of built-up edge on cutting tool and decreased the flank wear of tool.

In UAG, (1) imposing the ultrasonic vibration to the grinding wheel decreased the grinding forces and increased the material removal rate significantly. Strengthening the wheel ultrasonic vibration decreased the specific grinding energy, demonstrating that the ultrasonic vibration benefits the reduction in the energy consumption. (2) The ultrasonic vibration contributed to the work-surface finish improvement; the larger the $A_{p\text{-}p}$ was, the work-surface roughness became better. (3) The chip size, that is, cross-section area and length, was distinctly affected by the ultrasonic vibration but little effect of wheel peripheral speed is observed. (4) The ultrasonic vibration in grinding is avoiding the formation of shear chips and prefers the flow chips especially at larger amplitude. (5) The grinding wheel wear was dominantly attributed to chips adhesion, grains releasing/fracture which are reduced significantly by the ultrasonic vibration. The percentage of chips adhesion area and the number percentage of grains released/fractured decreased as the vibration amplitude increased.

Author details

Yongbo Wu[1,2]*, Qiang Wang[1,2], Sisi Li[1,2] and Dong Lu[2]

*Address all correspondence to: wuyb@akita-pu.ac.jp

1 Akita Prefectural University, Akita, Japan

2 Southern University of Science and Technology, Shenzhen, China

References

[1] Thakur D, Ramamoorthy B, Vijayaraghavan L. A study on the parameters in high-speed turning of superalloy Inconel 718. Materials and Manufacturing Processes. 2009; **24**(4):497-503

[2] Zhou J, Bushlya V, Avdovic P, Ståhl JE. Study of surface quality in high speed turning of Inconel 718 with uncoated and coated CBN tools. The International Journal of Advanced Manufacturing Technology. 2012;**58**(1-4):141-151

[3] Lin S, Chung C, Cheng Y. Combination of ultrasonic vibration and cryogenic cooling for cutting performance improvement of Inconel 718 turning. AIP Conf. Proc. 2011; **1163**(1):1163-1168

[4] Nath C, Rahman M. Effect of machining parameters in ultrasonic vibration cutting. International Journal of Machine Tools & Manufacture. 2008;**48**:965-974

[5] Salje E, Mohlgan H. Fundamental dependencies upon contact lengths and results in grinding. CIRP Annals—Manufacturing Technology. 1986;**35**(1):249-253

[6] Cao J, Wu Y, Lu D, Fujimoto M, Nomura M. Material removal behavior in ultrasonic-assisted scratching of SiC ceramics with a single diamond tool. International Journal of Machine Tools and Manufacture. 2014;**79**:49-61

[7] Subramanian K, Ramanath S, Tricard M. Mechanism of material removal in the precision grinding of ceramic. ASME Journal of Manufacturing Science and Engineering. 1997;**119**(4A):1-19. DOI: 10.1115/1.2831181

[8] Muhammad R, Ahmed N, Roy A, Silberschmidt VV. Turning of advanced alloys with vibrating cutting tool. Solid State Phenomena. 2012;**188**:277-284

[9] Tsao CC, Chen CC, Chen GC, Chueh CA, Qiu YX, Hsu CY. Ultrasonic-assisted on the turning of Inconel 718 by Taguchi method. Advanced Materials Research. 2012;**579**:160-173

[10] Babitsky V, Kalashnikov A, Meadows A, Wijesundara A. Ultrasonically assisted turning of aviation materials. Journal of Materials Processing Technology. 2003;**132**(1):157-167

[11] Silberschmidt VV, Mahdy SMA, Gouda MA, Naseer A, Maurotto A, Roy A. Surface-roughness improvement in ultrasonically assisted turning. Procedia CIRP. 2014;**13**: 49-54

[12] Hsu C, Lin Y, Lee W, Lo S. Machining characteristics of Inconel 718 using ultrasonic and high temperature-aided cutting. Journal of Materials Processing Technology. 2008; **198**(1):359-365

[13] Wang Y, Lin B, Wang S, Cao X. Study on the system matching of ultrasonic vibration assisted grinding for hard and brittle materials processing. International Journal of Machine Tools and Manufacture. 2014;**77**:66-73

[14] Liang Z, Wu Y, Wang X, Zhao W. A new two-dimensional ultrasonic assisted grinding (2D-UAG) method and its fundamental performance in monocrystal silicon machining. International Journal of Machine Tools and Manufacture. 2010;**50**(8):728-736

[15] Mult HC, Spur IG, Holl SE. Ultrasonic assisted grinding of ceramics. Journal of Materials Processing Technology. 1996;**62**(4):287-293

[16] Pei ZJ, Ferreira PM, Kapoor SG, Haselkorn M. Rotary ultrasonic machining for face milling of ceramics. International Journal of Machine Tools and Manufacture. 1995; **35**(7):1033-1046

[17] Liu DF, Cong WL, Pei ZJ, Tang YJ. A cutting force model for rotary ultrasonic machining of brittle materials. International Journal of Machine Tools and Manufacture. 2012; **52**(1):77-84

[18] Zahedi A, Tawakoli T, Akbari J. Energy aspects and workpiece surface characteristics in ultrasonic assisted cylindrical grinding of alumina-zirconia ceramics. Archives of Civil and Mechanical Engineering. 2015;**90**:16-28

[19] Bhaduri D, Soo SL, Aspinwall DK, Novovic D, Harden P, Bohr S, Martin D. A study on ultrasonic assisted creep feed grinding of nickel based superalloys. Proceedings of the CIRP. 2012;**1**:359-364

[20] Lu D, Q Wang YW, Cao J, Guo H. Fundamental turning characteristics of Inconel 718 by applying ultrasonic elliptical vibration on the base plane. Materials and Manufacturing Processes. 2015;**30**(8):1010-1017

[21] Q Wang YW, J Gu DL, Ji Y, Nomura M. Fundamental machining characteristics of the in-base-plane ultrasonic elliptic vibration assisted turning of Inconel 718. Procedia CIRP. 2016;**42**:858-862

[22] S Li, Y Wu, M Fujimoto, M Nomura. Improving the working surface condition of electroplated cubic boron nitride grinding quill in surface grinding of Inconel 718 by the assistance of ultrasonic vibration. Journal of Manufacturing Science and Engineering. 2016;**138**:071008-071001-8

[23] Li S, Wu Y, Nomura M. Effect of grinding wheel ultrasonic vibration on chip formation in surface grinding of Inconel 718. International Journal of Advanced Manufacturing Technology. 2016;**86**:1113-1125

[24] Mitrofanov A, Ahmed N, Babitsky V, Silberschmidt V. Finite element analysis of ltrasonically assisted turning of Inconel 718. Journal of Materials Processing Technology. 2004;**153**:233-239. DOI: 10.1016/j.jmatprotec.2004.04.299

[25] Zhang X, Senthil Kumar A, Rahman M, Nath C, Liu K. Experimental study on ultrasonic elliptical vibration cutting of hardened steel using PCD tools. Journal of Materials Processing Technology. 2011;**211**(11):1701-1709

[26] Zhang DK, Li C, Jia D, Zhang Y. Investigation into engineering ceramics grinding mechanism and the influential factors of the grinding force. International Journal of Control and Automation. 2014;**7**(4):19-34

[27] Shaw MC. Principles of Abrasive Processing. Australia: Mech Chem Engng. Inst. Engrs; 1996

[28] Tso P-L. An investigation of chip types in grinding. Journal of Materials Processing Technology. 1995;**53**:521-532

Chapter 5

Dry High Speed Orthogonal Turning of Titanium Alloy Wear Evolution and Chip Morphology

Mohieddine Benghersallah, Lakhdar Boulanouar, Gautier List and Guy Sutter

Additional information is available at the end of the chapter

http://dx.doi.org/10.5772/intechopen.78669

Abstract

The present work is an experimental study on the dry high-speed turning of Ti-6Al-4 V titanium alloy. The objective of this study is to see for high cutting speeds, how wear occurs on the face of insert and how to evolve cutting forces and chip formation. Cutting speeds tested is 600, 800, 1000 and 1200 m/min in orthogonal turning with a carbide insert tool H13A uncoated and coated TiN on a cylindrical titanium alloy part. Investigation on the wear inserts with 3D microscope scanning revered the crater formation is instantaneous and a chip adhesion. Welded chip causes detachment of carbide particles. In these experiments the chip shape was systematically investigated at each cutting conditions using optical microscopy. The chips produced were collected and polished to measure the thicknesses t_{2max} and t_{2min}. The distance between each segments d_{ch} and ϕseg inclination angle as described in the introduction part, the shear angle ϕ and the inclination angle of a segment ϕseg are differentiated. ϕseg angle is actually measured on the collected chips while the shear angle ϕ cannot be. The angle ϕ represents the initial shear similar to the one that describes the formation of a continuous chip in the primary shear zone. Cutting forces increase and stabilize before removing the tool. The chip reaches a very high temperature.

Keywords: titanium alloys, dry high-speed machining, chip formation, cutting zone, confocal imaging

1. Introduction

Titanium alloys such as Ti–6Al–4 V, Ti-555, Ti6242S, and Ti-LCB, are used extensively in the aerospace industry for structural components (compressor blades, disks, castings, and gas

turbine engines) due to their superior properties such as excellent strength-to-weight ratio, strong corrosion resistance and ability to retain high strength at high temperatures [1–3]. Light-weight materials such as titanium alloys are now used in modern aerospace structure due to their best combination of metallurgical and physical properties. Each class of titanium alloy has their advantages and disadvantages. Titanium's advantages are high strength-to-weight ratio, low density, excellent corrosion resistance, excellent erosion resistance and low modulus of elasticity.

Ti-6Al-4 V may be considered in any application where a combination of high strength at low to moderate temperatures, light weight and excellent corrosion resistance are required. Some of the many applications where this alloy has been used include aircraft turbine engine components, aircraft structural components, aerospace fasteners; high-performance automotive parts, marine applications, medical devices, and sports equipment [1–4].

Titanium and its alloy have poor machinability, this may be due to their high chemical reactivity with most cutting tools and therefore, have a tendency to weld to the cutting tool during machining, thus leading to chipping and premature tool failure. Its low thermal conductivity increases the temperature at the tool/work piece interface, which affects the tool life [2, 3, 5].

Minimum quantity lubrication (MQL) is widely applied for titanium alloy machining, meanwhile, in the machining process of titanium alloy, there are several problems regarding tool wear, poor surface damage, and machining deformation. Moreover, surface damage usually appears during high-speed machining. Therefore, the contradiction between increasing machining demand and machining performance has become a bottleneck in actual industry.

On the other hand, there are critical needs to reduce the usage of cutting fluid in machining process in order to reduce the environmental burden and economic cost [3]. Dry and minimum quantity lubrication (MQL) machining which are two types of green manufacturing processes have vast potentials for machining of titanium alloys [4–6]. Additionally, the tool coating is a key factor to realize high-speed machining and green manufacturing. Coating materials is widely employed to extend tool life and cutting performance of cutting tools due to their advanced wear resistance and superior performance under corrosive or high temperature conditions. However, the tool coatings used presently in machining of titanium alloys cannot meet with the need of high-speed machining and green manufacturing. Simultaneously, as one of an effective green manufacturing technology, the combination of MQL and novel cutting tools is also growing.

1.1. Topographic tool wear characterization

In recent years, many microscopy techniques were commonly used for characterizing the surface topography in many scientific fields (**Figure 1**) [7, 14, 20].

The atomic force microscopy (AFM), stylus profilometry, stereo microscopy (SM), scanning electron microscopy (SEM), reflected light interference microscopy (RLIM), and confocal laser scanning microscopy (CLSM). The first two are touch instruments, while others are non-contact instruments. AFM, the state of the art profiler, has excellent depth and transverse resolution.

http://dx.doi.org/10.5772/intechopen.78669

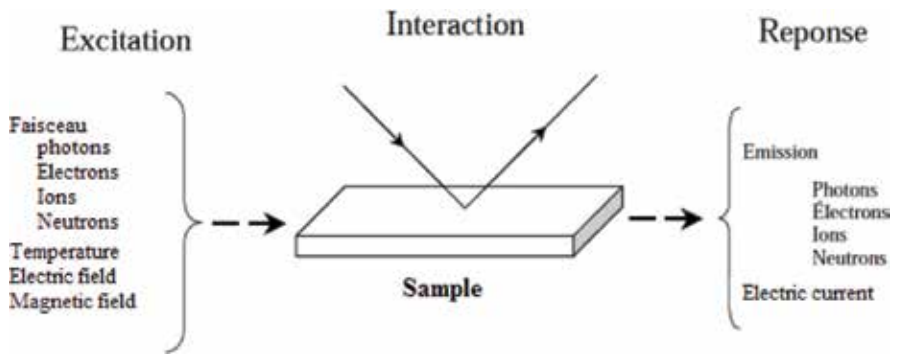

Figure 1. General principle of surface characterization methods [7].

However, its disadvantages such as slow scan very small field sample (usually 70 × 70 um), restricted depth range (about 5 μm), its inability to scan deep holes, and the extreme fragility of the tip prevented its immediate application to tool wear analysis [8–11].

In the conventional optical microscope, the image is "flat", providing lateral dimensional information (X and Y), but not axial (Z). The image contrast is derived generally in variations of surface reflectivity. Confocal microscopy provides quantitative information on the optical axis (Z). The principle of the confocal microscope is to focus, through a goal, a laser beam will illuminate a point of the sample, then recovering on a photomultiplier, the light signal emitted at this point [12, 13].

Confocal microscopy is a non-destructive optical technique to obtain optical sections not only in the plane (X, Y), but also along a plane (X, Z) parallel to the optical axis which can be obtained a three-dimensional reconstructions [14]. These optical sections "virtual" do not affect the entire sample unlike physical cuts necessary in electron microscopy. The latest developments in fluorescent confocal microscopy allow, for marking means based on the use of fluorescent products, observe remarkable 3D structures.

One of the drawbacks of confocal microscopy is its slow action. Indeed, the measurement of a 3D structure requires up to a few hours.

The principle of the operation of the confocal microscope is shown in **Figure 2**. Light emitted from the source after passing through the optical path is focused on the analyzed surface. The reflected beam reaches to a diaphragm which transmits only focused light and to a photodetector. A vertical scanning system is moving the lens, which allows to analyze different height areas of roughness. That ability to distinguish height improves significantly the contrast and the lateral resolution in comparison with the classic optical microscope. Scanning confocal microscopes took advantage of the differentiation of depth and generating of surface image and reception of reflected beam is done by the same optical system. Like in the scanning method, the optical system generates a spot on a surface, and a reflected light beam is recorded by a point detector. In the construction of a diaphragm of a modern confocal microscope a Nipkow disk with a series of spiral splitting small holes is used. In connection with a

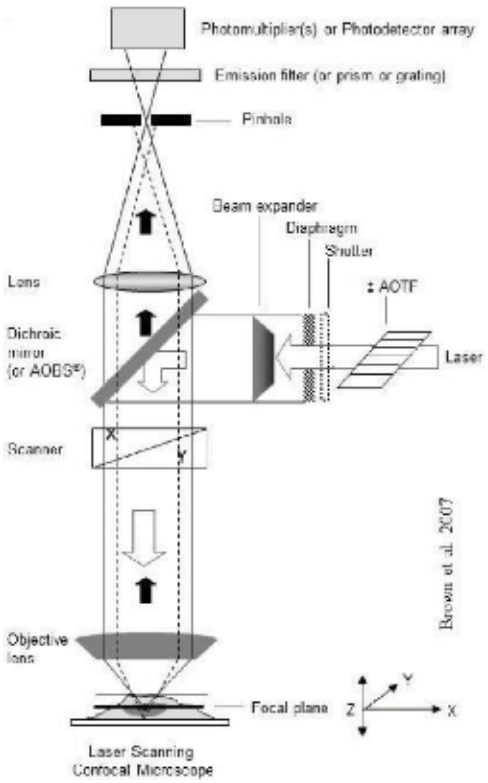

Figure 2. Confocal microscopic principle [7, 15–17].

suitably prepared light beam (after passing through another Nipkow disk with microlenses) it allows a scan of the surface topography effectively.

The scanning microscope in recent years has been generally accepted. It is a tested and approved technique on the nano scale, which allowed to obtain very good vertical resolution. Serious problems appear only in the case of very rough surfaces and the necessity to use a larger vertical range. Microscope application can cause a little difficulty in the interpretation of results of measurement, especially when samples have inclusions or impurities on the surface, which characteristics are variable or can have an influence on response of instrument [14].

The cutting edge shape and the cutting edge condition are of crucial importance for machining operations. During the cutting process the impact of high thermal and mechanical loads on the cutting edge result in wear. Moreover, the quality of the machined surface is affected by the cutting edge shape. The demands of modern production are high productivity and high process reliability. One place these demands can be met is in cutting edge preparation [13, 14, 18].

Tool wear is one of the most complex problems in machining because it is affected by various factors such as the behavior of the work material, the interaction of the work material with the cutting tool, machining condition, dynamics, and the stability of machining tools. This makes the identification of the dominating wear mechanisms very difficult. The development of wear models based on these wear mechanisms, the interfacial stress and temperature fields

determination, and the topography characterization of tool wear stand out among the most urgent issues in this area of research. If these issues can be resolved, tool life can be easily predicted and the effectiveness of cutting tools improved.

Tool life is dictated by catastrophic failure, plastic deformation, and gradual wear. The first two imply premature failures of a tool and, therefore, should be avoided at all times. Gradual wear is the main interest because it limits tool life in a typical machining condition. The most common forms of gradual tool wear are flank wear and crater wear. Flank wear limits the service life of a tool directly because it affects dimensional accuracy, forces generated, and power consumption. Crater wear can reduce the cutting forces. However, the weakening of the cutting edge ultimately leads to failure. Crater wear represents a greater challenge than flank wear due to many competing wear mechanisms, such as abrasion, dissolution, and/or diffusion [14, 18].

1.2. Tool wear mechanisms

For many years, the study of tool wear has been limited to empirical approaches. The well-known empirical Taylor's equation, for example, is convenient when dealing with few work materials and cutting tools. However, it is unable to predict the performance of new work and tool materials without a substantial amount of machining experiments. Therefore, such an empirical equation cannot be used in the development of new cutting tools. On the other hand, some researchers [13, 14, 19–24] have approached tool wear from physics-based models.

The main wear mechanisms involved in tool wear have been proposed to be adhesion, abrasion, diffusion, and dissolution. Flank wear is caused mainly by abrasion of the hard second phase in a work material. Crater wear is controlled by a combination of adhesion, abrasion, dissolution, and/or diffusion [15, 17, 25, 27, 29, 30]. At present, it is not clear exactly which mechanisms dominate crater wear in relation to the cutting condition. In high-speed machining, crater wear is believed to be dominated by dissolution wear and subsequent diffusion [15–17, 25–27]. The aim of this paper is to explain qualitatively the high crater wear resistance of multilayer coated carbides through the observation and analysis of their confocal topography.

2. Experimental work

The workpiece is a Ti–6Al–4 V alloy bar with a length of 300 mm and a diameter of 110 mm. **Tables 1** and **2** show the chemical composition and physical properties of the titanium alloy, respectively.

The machining trials were carried out on a CNC lathe, with a 22 kW motor drive with a maximum torque of 2000 Nm. The spindle rotation speed ranges from 18 to 4500 rpm.

All cutting tests were carried out with uncoated carbide inserts (H13A-P15, 6% Co and 94% WC) without chip-breaker, with a rake angle $\gamma = 0°$ and a clearance angle of 7° [21].

The cutting forces were measured at the early stages of machining up to 1 minute, when the inserts have not suffered appreciated wear, with a piezoelectric Kistler dynamometer (**model 9441B**), connected to a charge amplifier.

Al	V	Fe	O_2	H_2	N_2	Ti
6	4	0.03	0.01	0.01	0.25	Balance

Table 1. Nominal composition of Ti-6Al-4 V (wt.%).

Tensile strength (MPa)	0.2% Proof stress (MPa)	Density (g/cm^3)	Elongation 5D (%)
960 ± 1270	885	4.42	8
Reduction of area (%)	Modulus of elasticity tension (GPa)	Hardness (Hv)	Thermal conductivity (W/mK)
25	100–130	330–370	7

Table 2. Mechanical and thermal properties of Ti–6Al–4 V.

The tool inserts were used to machine the titanium alloy at the following conditions:

- Cutting speeds (m/min): 600, 800, 1000, 1200 m/min
- Feed rate (f): 0.1 mm/rev.
- Depth of cut: 3 mm

The test is to be machined orthogonally the workpiece on a depth ap = 0.3 mm and feed rate f = 0.1 mm/rev. with five cutting speed values according (600, 800, 1000, 1200 m/min) (**Figure 3**).

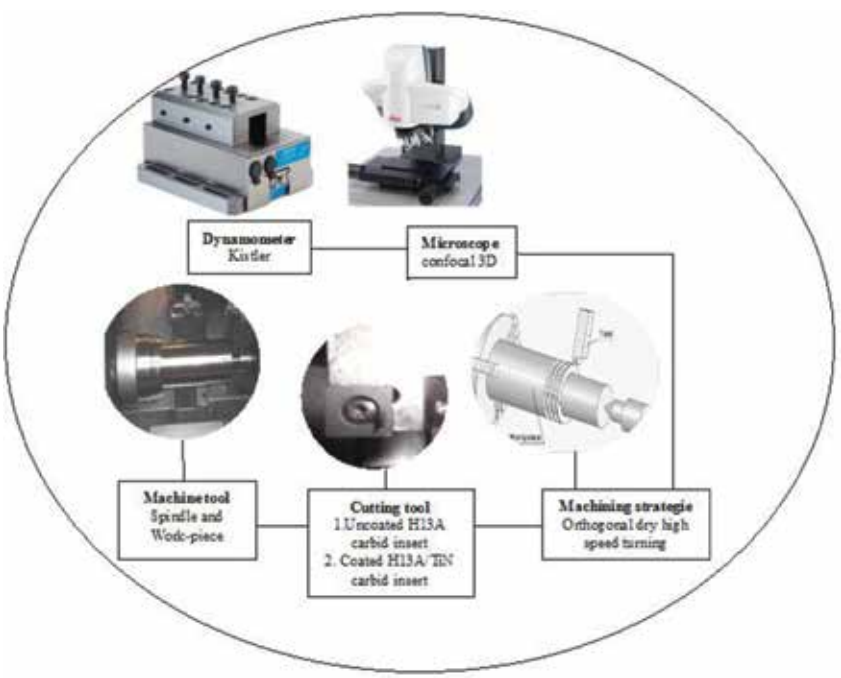

Figure 3. Schematic diagram of experimental setup.

http://dx.doi.org/10.5772/intechopen.78669

3. Results and discussion

A. Wear investigations

First investigations concerning the wear inserts to know if the H13A [28] tool material resists wear for very high cutting speeds.

The microscope photography shows a welding chip on the rake face. The temperature in the cutting zone reaches values near to the melting temperature of the material being machined. Instantly the chip stands and removed with him the substrate material of the tool which causes the crater wear.

Figure 4 shows the confocal image obtained by the microscope DCM3D of the cutting insert for the machining conditions (V c = 600 m/min, f = 0.1 mm, ap = 3 mm) on this picture we can see the welded chip on the rake face. **Figure 4c**), shows the profile diagram of the cutting insert obtained by skew right A. A on unworn cutting edge and the profile of crater obtained between welding chip zone by skew right B.B.

Figure 5a is a microscope photography of the cutting zone on the insert according the cutting parameters (800 m/min, f = 0.1 mm/rev, ap = 3 mm) on the rake face we can see the crater wear formation. **Figure 5b** shows 3D image of cutting insert according the cutting parameters, we can see the crater wear formation in rake face and collapse of cutting edge. **Figure 5c** shows the profile of crater wear obtained by skew right A.A.

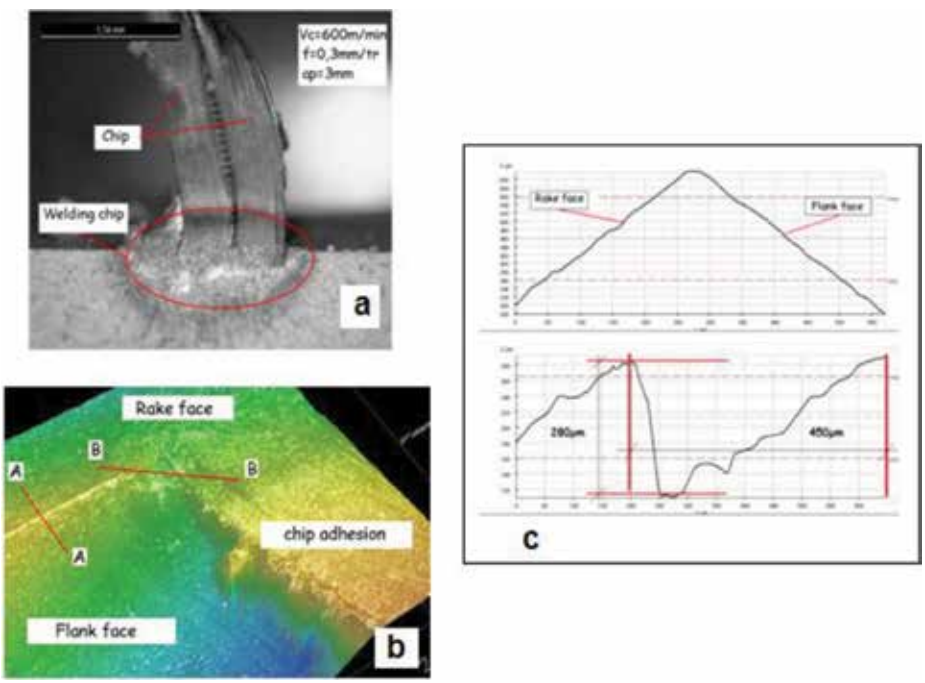

Figure 4. (a) Photography of chip welding on rake face, (b) 3D confocal image of the cutting insert (600 m/min, f = 0.1 mm/rev, ap = 3 mm), (c) profile diagram obtained by skew right unworn cutting edge and profile of crater failure under chip welding.

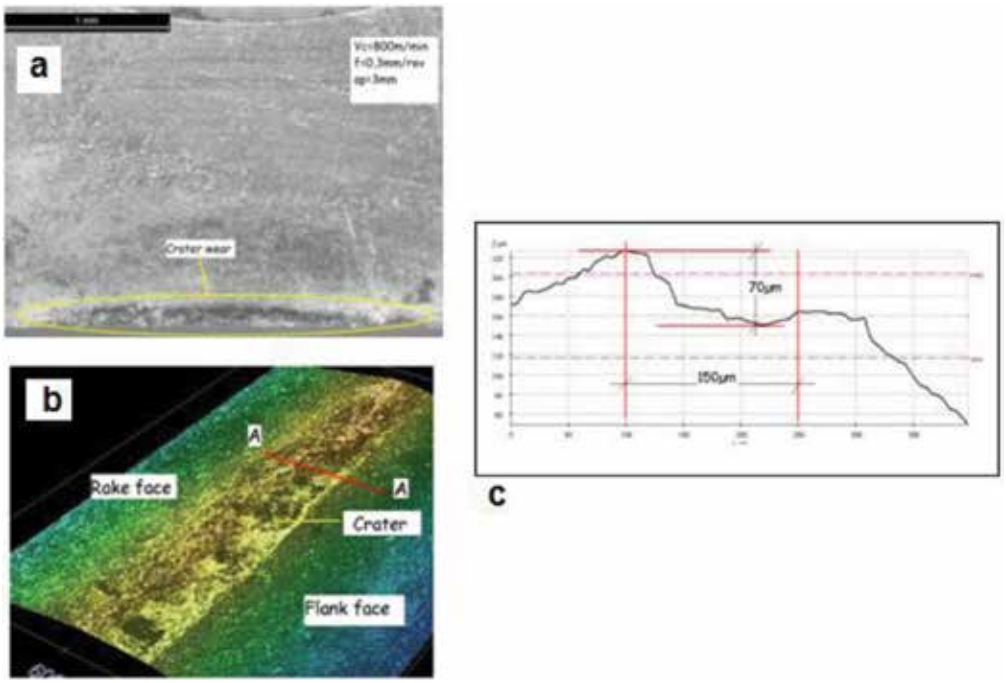

Figure 5. (a) Photography of cutting edge insert (b) 3D confocal image of the cutting insert according the cutting parameters (800 m/min, f = 0.1 mm/rev, ap = 3 mm), (c) crater profile by skew right A.A.

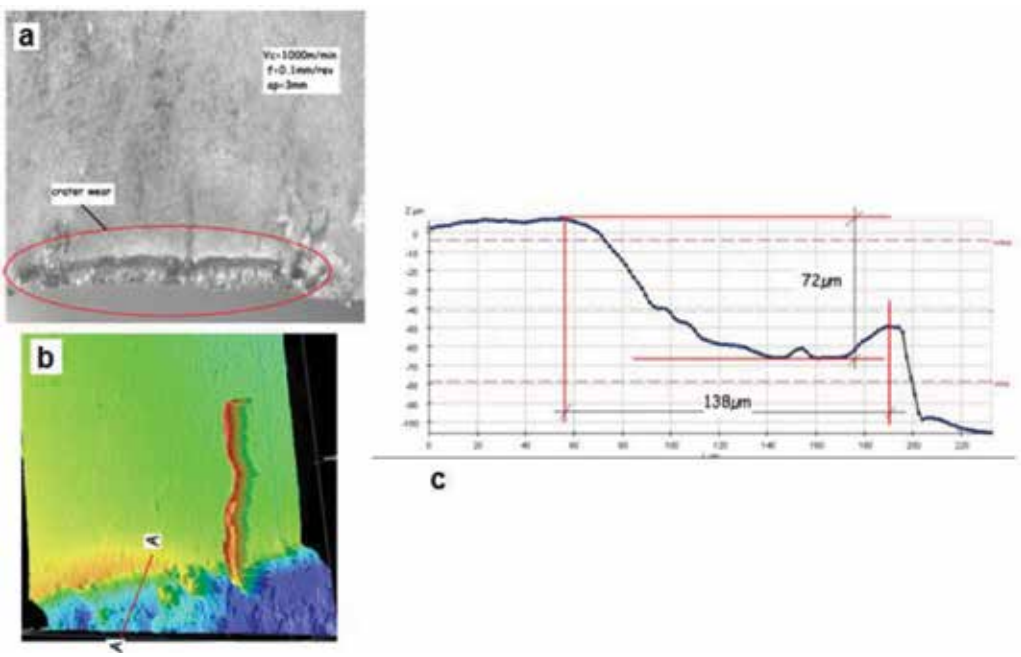

Figure 6. (a) Photography of cutting zone of insert according the cutting parameters (1000 m/min, f = 0.1 mm/rev, ap = 3 mm), (b) 3D confocal image, (c) profile 2D of crater wear.

The photography of optical microscope (**Figure 6a**) show the insert according the cutting parameters (Vc = 1000 m/min, f = 0.1 mm/rev, ap = 3 mm). We can see the crater wear and chip adhesion in different area. **Figure 6b** show in 3D image confocal the chip welded and crater wear and the collapse at the sharp ridge. In **Figure 6c**, the crater wear values are defined with the 2D profile.

The photography of optical microscope (**Figure 7a**) show the insert according the cutting parameters (Vc = 1200 m/min, f = 0.1 mm/rev, ap = 3 mm). We can see the crater wear formation on rake face. **Figure 7b**, show in 3D image confocal the crater wear and the collapse at the sharp ridge. In **Figure 7c**, the crater wear values are defined with the 2D profile.

Early investigations clearly show that for very high cutting speeds, the plate wears quickly. This is due to excessive heating of the cutting area. The temperature in the cutting zone reaches superior to the melting temperature of Ti-6Al-4 V values. This material known for its poor thermal conductivity welds.

3.1. Confocal imaging of coated TiN insert

The confocal image of the **Figure 8a** shows a portion of the H13A TiN coating insert during the cutting parameters (Vc = 600 m / min, f = 0.1 mm / rev, ap = 3 mm). On the flank face we observed a welding chip of Ti6Al4V titanium alloy. The temperature in the cutting zone is very high, the chip is welded, it causes wear in crater on the rake face. This crater is born after the posting of the substrate particles forming the insert. The predominant wear is by adhesion. The confocal image of the **Figure 8b** shows the wear on the H13A TiN coating insert

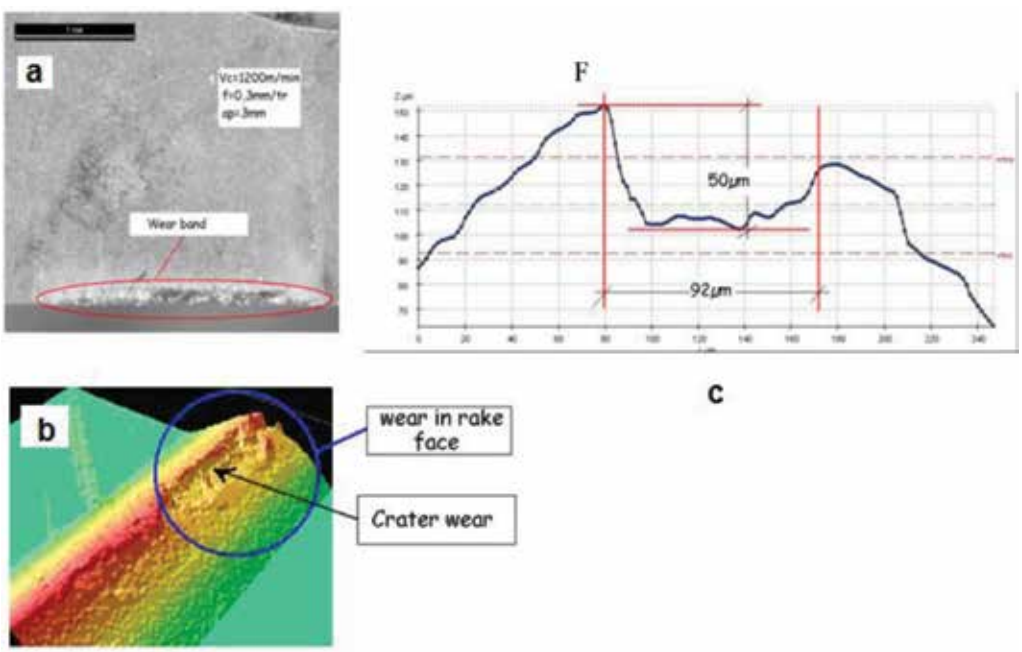

Figure 7. (a) Photography of cutting edge according (Vc = 1200 m/min, f = 0.1 mm/rev, ap = 3 mm). (b) 3Dconfocal image, (c) profile 2D of crater wear.

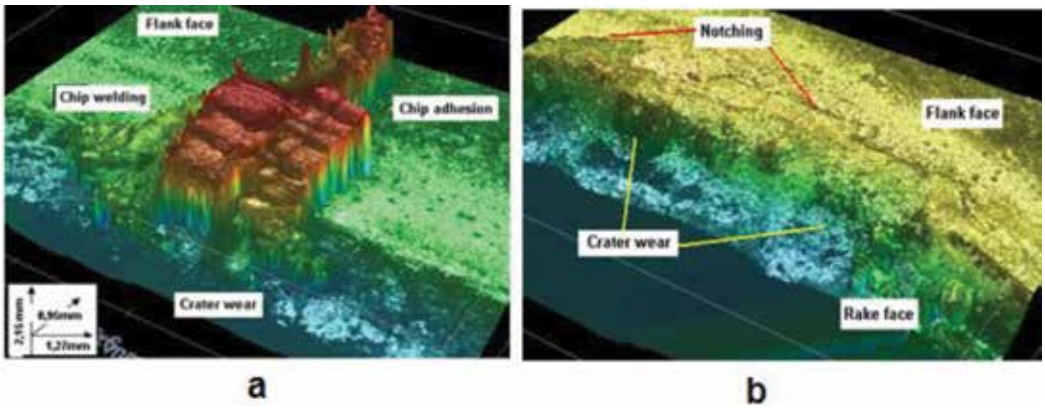

Figure 8. (a) 3D confocal image according (600 m/min, f = 0.1 mm/rev, ap = 3 mm) for coating TiN insert, (b) 3D confocal image according (Vc = 800 m/min, f = 0.1 mm/rev, ap = 3 mm) for coating TiN insert.

for the cutting parameters (Vc = 800 m/min, f = 0.1 mm/rev, ap = 3 mm). On the rake face we observed the crater wear formation caused by the adhesion of the titanium alloy chip. The chip is welded and then migrates under the high-speed action of next chip. On the rake face coating stands served and the increase in flank wear by abrasion to the total damage of the cutting edge.

The confocal image of the **Figure 9a** shows the wear on the insert for the cutting speed (Vc = 1000 m/min, f = 0.1 mm/rev, ap = 3 mm). The particles of the welding chip are observed. Tearing of these chips causes a crater by wear adhesion. The chip welded titanium migrate under the effect of the high-speed thrust next chip. On the flank face we observed the formation of the band of the flank wear and the effect of the temperature with the detachment of the coating. The confocal image of the **Figure 9b** shows the wear on the coating insert for the cutting parameters (Vc = 1200 m /min, f = 0.1 mm/rev, ap = 3 mm). On the rake face there is a

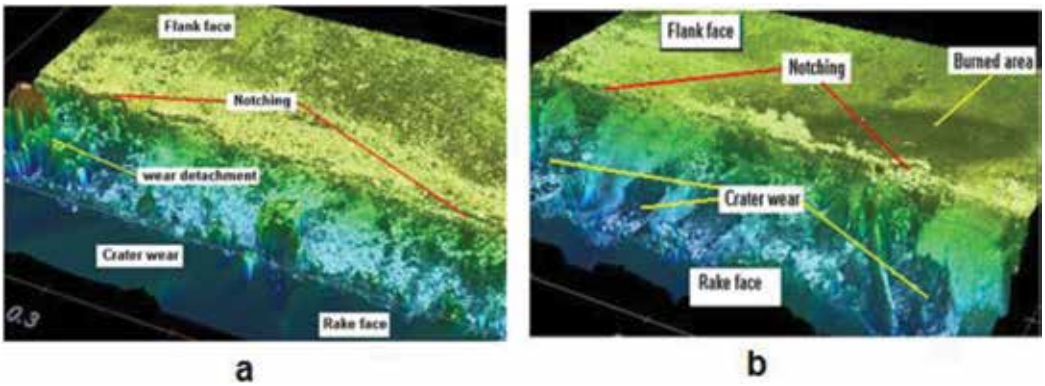

Figure 9. (a) 3D confocal image according (Vc = 1000 m/min, f = 0.1 mm/rev, ap = 3 mm) for coating TiN insert, (b) 3D confocal image according (Vc = 1200 m/min, f = 0.1 mm/rev, ap = 3 mm) for coating TiN insert.

very pronounced crater wear caused by tearing of the chip that forces the particles from the substrate to detach. The next chip and forms a crater wear. On the flank face we observed the formation of the band of the flank wear and the effect of the temperature of the chip in combustion phase leaving burn marks.

The overall analysis of 3D confocal images shows that the dominant wear for orthogonal turning high-speed titanium is the main crater wear caused by adhesion.

3.2. 2D profiles of crater wear measurements

Figure 10 shows the profiles of the craters of each insert under different cutting conditions, we can give the depth of each crater.

3.3. Diagram of crater wear evolution

Figure 11 shows the evolution of the depth of rake face crater for different parameters of cutting regime and for the two types of inserts. With uncoated insert the largest depth of the crater is recorded for 600 m/min testing. The depth of KT has decreased for 800 m/min cutting speed, it increases significantly for 1000 m/min. At 1200 m/min we noticed a sharp decrease in crater depth. For TiN coated insert, the value of the crater depth is substantially the same. This is due to the coating which is a barrier against crater wear.

B. Flank wear characterization

In **Figure 12** confocal image is observed from the flank face of the H13A TiN coating insert following conditions:

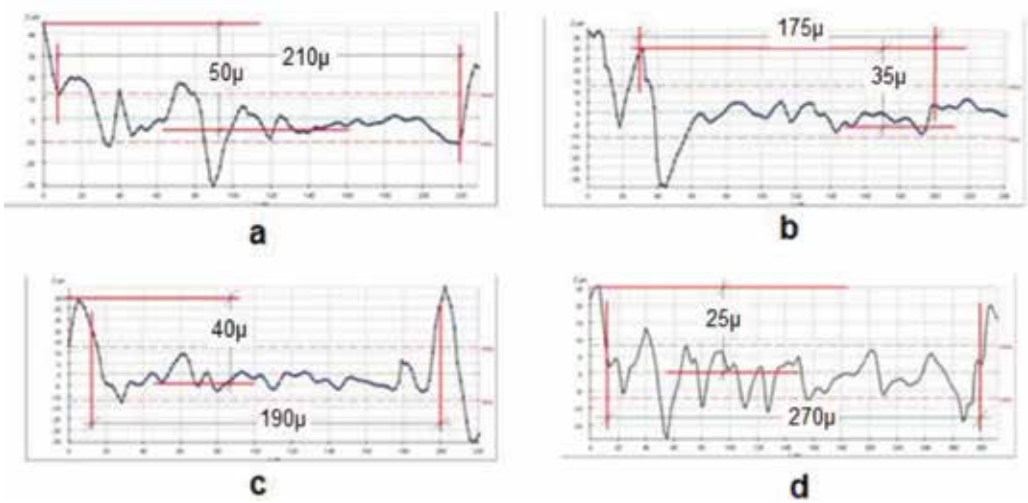

Figure 10. (a) 2D profile of crater wear according the following conditions (Vc = 600 m/min, f = 0.1 mm/tr, ap = 3 mm). (b) 2D profile of crater wear according the following conditions (Vc = 800 m/min, f = 0.1 mm/tr, ap = 3 mm). (c) 2D profile of crater wear according the following conditions (Vc = 1000 m/min, f = 0.1 mm/tr, ap = 3 mm). (d) 2D profile of crater wear according the following conditions (Vc = 1200 m/min, f = 0.1 mm/tr, ap = 3 mm).

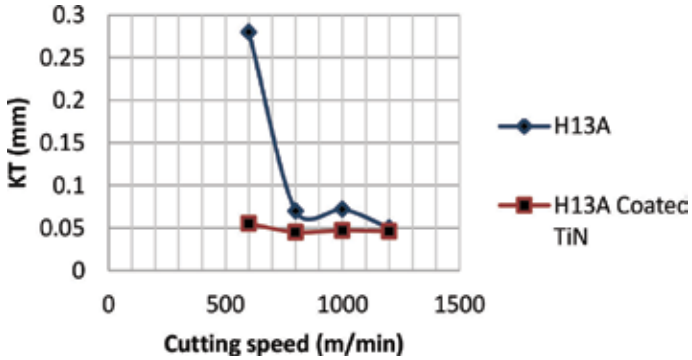

Figure 11. Crater wear evolution for two carbides inserts according the cutting parameters.

(a) (Vc = 600 m/min, f = 0.1 mm/rev, ap = 3 mm). Wear is caused by the friction of the workpiece on the flank face, the predominant wear is obtained under the effect of abrasion accompanied by the wear caused by the migration of the substrate particles removed by the adherent chip. **Figure 12b** shows for the conditions (Vc = 800 m/min, f = 0.1 mm/rev, ap = 3 mm), the chip welding on the rake face has been abraded by rubbing on the workpiece surface. The chip detachment will generate a catastrophic wear caused by the detachment of the substrate. **Figure 9c** shows the conditions (Vc = 1000 m/min, f = 0.1 mm/rev, ap = 3 mm), we observe a

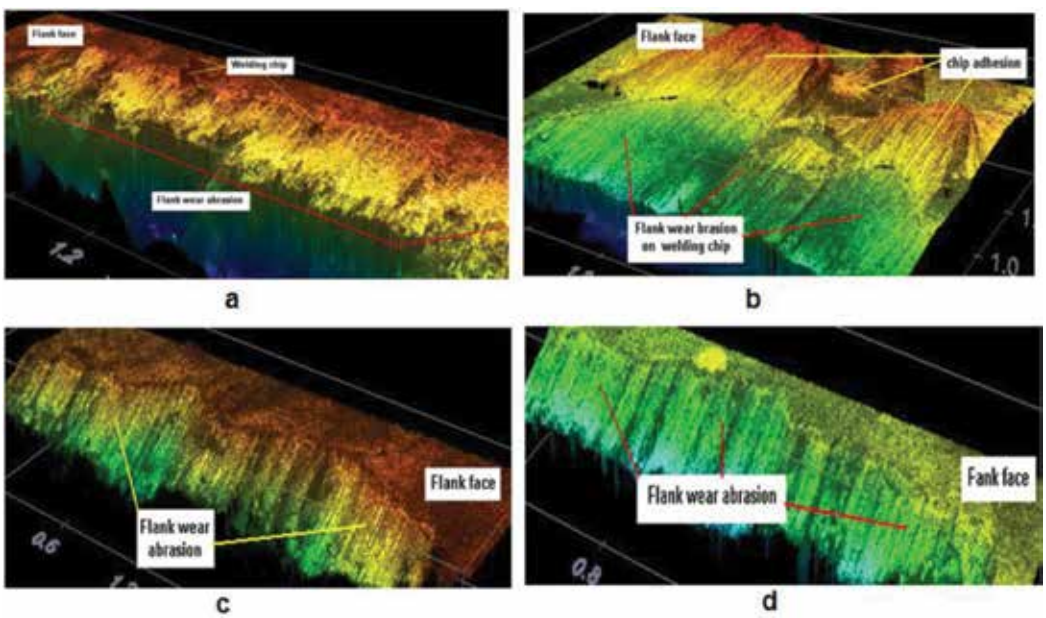

Figure 12. (a) 3D confocal image of the flank wear according (Vc = 600 m/min, f = 0.1 mm/rev, ap = 3 mm) for coating TiN insert. (b) Confocal image of the flank wear according (Vc = 800 m/min, f = 0.1 mm/rev, ap = 3 mm) for coating TiN insert. (c) 3D confocal image of the flank wear according (Vc = 1000 m/min, f = 0.1 mm/rev, ap = 3 mm) for coating TiN insert. (d) 3D confocal image of the flank wear according (Vc = 1200 m/min, f = 0.1 mm/rev, ap = 3 mm) for coating TiN insert.

http://dx.doi.org/10.5772/intechopen.78669

Figure 13. Orthogonal cutting zone. Zone 1 Primary shearing zone. Zone 2 Secondary shearing zone (interface friction tool/chip). Zone 3 Tertiary friction (interface tool/workpiece zone).

flank wear caused by abrasion. **Figure 9c** shows a flank wear caused by high abrasion under (Vc = 1000 m /min, f = 0.1 mm/rev, ap = 3 mm), conditions.

C. Chip morphology investigation

First investigations concerning the chip morphology obtained in very high speed orthogonal turning by H13A uncoated and coated inserts tool material.

Using the optical microscope with high definition the Serrated chip obtained from experiments is showing in **Figure 13**.

Geometry of the chip shape in these experiments was systematically investigated at each cutting conditions using optical microscopy. The chips produced were collected and polished to

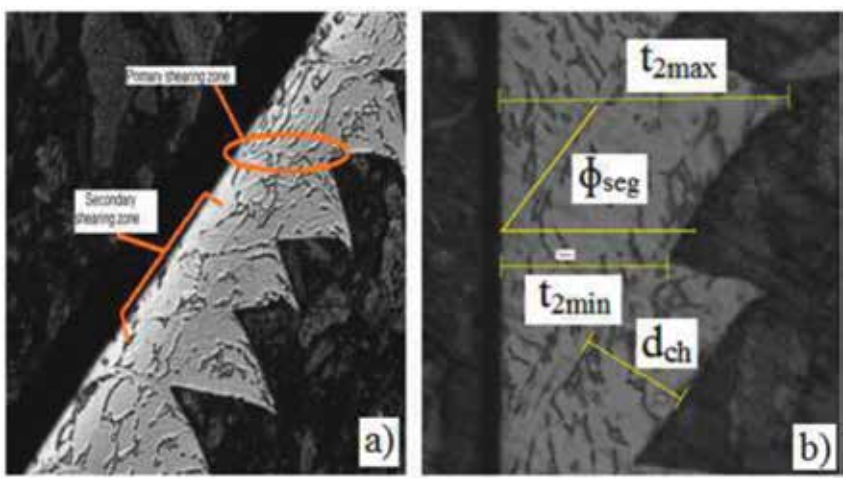

Figure 14. Serrated chip shape from experiments showing (a) shear zones, (b) the measured parameters [12].

measure the thicknesses t_{2max} and t_{2min}, d_{ch} the distance between each segments and ϕseg the inclination angle, see **Figure 14**. From t_{2max} and t_{2min} values, the degree of segmentation G was evaluated by:

$$G = \frac{t_{2max} - t_{2min}}{t_{2max}} \quad (1)$$

In high-speed machining the chip is segmented. The degree of segmentation gives an idea of the shear rate. This quantity indicates whether or not the chip is forming well and that the machining conditions are good.

Some pictures of serrated chips obtained for different cutting speeds, uncoated and coated TiN carbide inserts are presented in **Table 3** with 600 m/min cutting speed, and uncoated insert we see the chip is segmented, but it is not uniform. For the cutting speed 800 m/min, the chip is almost continuous, it is poorly segmented despite.

Significant strain in the shear zone. At the speed of 1000 m/min, the chip is uniform and well segmented, machining conditions are favorable a 1200 m/min, the chip is segmented at the beginning of machining, it is no longer uniform end machining (**Figure 15**).

As described in the introduction part, the shear angle ϕ and the inclination angle of a segment ϕ_{seg} are differentiated as shown in (**Figure 15**). The angle ϕ_{seg} is actually measured on the collected chips while the shear angle ϕ cannot be. The angle ϕ represents the initial shear similar to the one

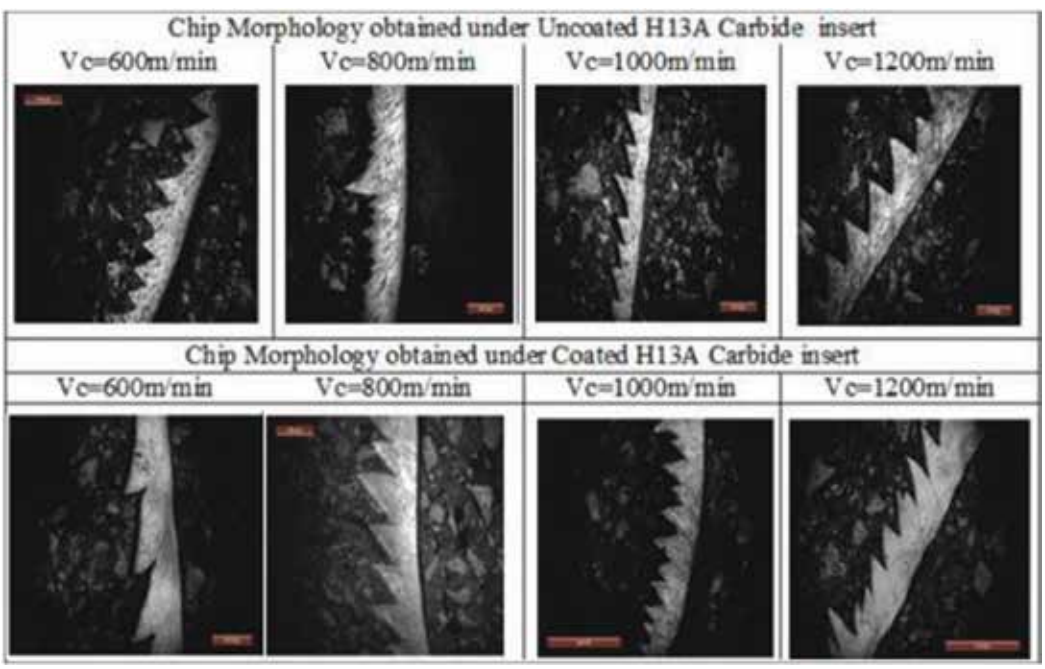

Table 3. Photography of chip morphology.

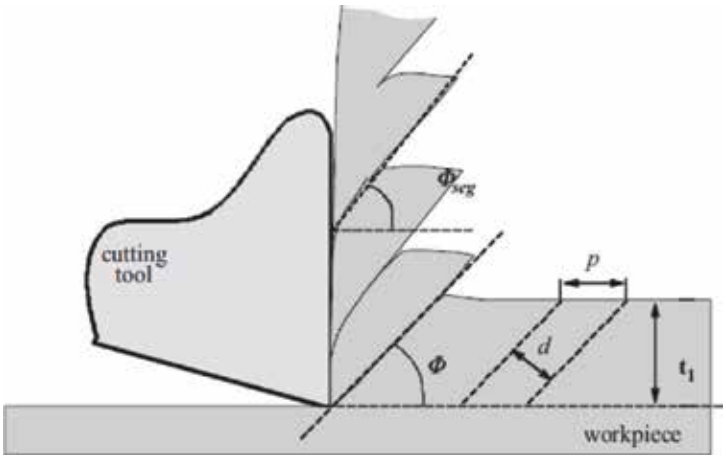

Figure 15. Schematic diagram of the serrated chip [12].

that describes the formation of a continuous chip in the primary shear zone. Considering that an element of volume, characterized by the angle ϕ, the length p and the width d is the source of a segment with the inclination ϕ_{seg} and the width d_{ch}, by applying the condition of incompressibility in plastic deformation, we obtain the balance equation Finally, with the assumption that the values of d and d_{ch} are close ($d = d_{ch}$), the initial shear angle f may be estimated by the following equation:

$$\varnothing = arc\ 0\sin\left(\frac{t_1}{(t_{2max}/\cos\varnothing\ seg) - d_{ch}\tan\varnothing\ seg}\right) \quad (2)$$

D. Analysis of the chip segmentation (Table 4)

Figure 16 shows that the degree of segmentation varies with the cutting speed. The largest value is recorded for the speed Vc = 1000 m/min. as speed increases, the degree of segmentation decreases. The variation of the degree of segmentation is more important for the TiN coated insert.

Figure 17 shows that the shear angle of the chip is larger for the coated insert. This value decreases substantially at 1000 m/min cutting speed and then increases towards 1200 m/min.

Cutting speed m/min								
	Uncoated	Coated	Uncoated	Coated	Uncoated	Coated	Uncoated	Coated
t_{2max}	0.298	0.231	0.320	0.209	0.139	0.384	0.302	0.222
t_{2min}	0.154	0.147	0.173	0.141	0.053	0.125	0.121	0.106
G	0.483	0.360	0.460	0.320	0.610	0.640	0.600	0.520
ϕseg	44°	73°	41°	37°	40°	59°	53°	59°
d_{ch}	0.111	0.088	0.111	0.078	0.056	0.181	0.112	0.070

Table 4. Parameters value of chip morphology.

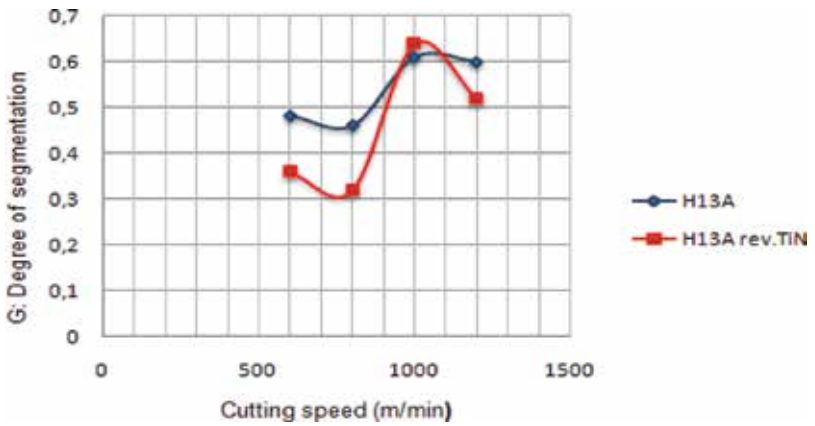

Figure 16. Degree of chip segmentation G evolution.

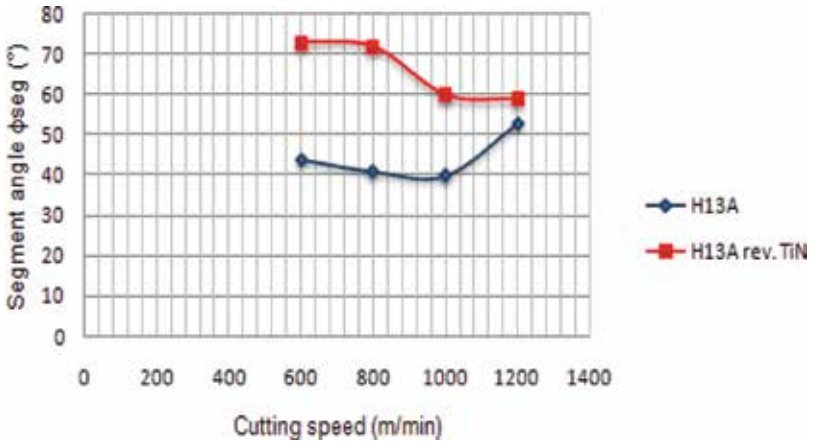

Figure 17. Evolution of shear angle ϕ.

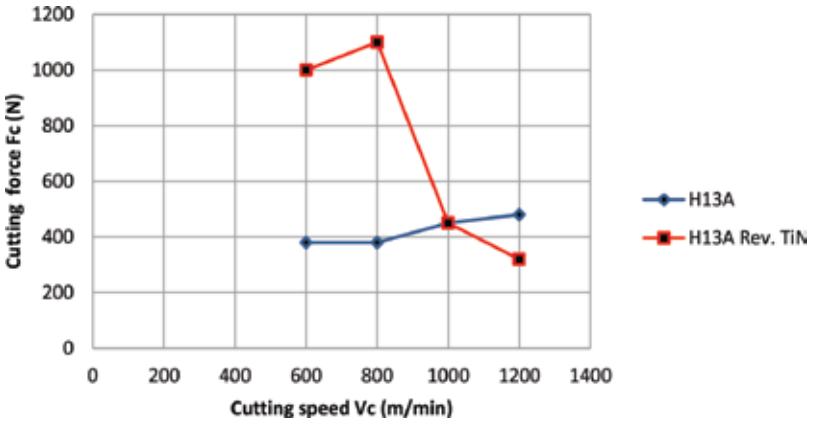

Figure 18. Cutting force evolution according cutting speed for uncoating and TiN coating inserts.

E. Cutting force evolution

The cutting forces measured at the beginning of the cut for each condition are given in **Figure 18**. Since the forces were measured at the beginning of the cut (first 5 s), it can be assumed that tool wear is negligible and therefore, the observed cutting forces are a function of the workpiece shear strength, chip shear angle and friction between the workpiece and tool.

Figure 18 shows the evolution of the cutting force Fc according to different cutting speeds. For H13A insert the cutting force Fc did not increase significantly. For TiN coated insert the cutting force Fc is important for cutting speeds (600 and 800 m/min), it greatly decreases in the speeds range (1000/1200 m/min). We explained this by the fact for the uncoated H13A plate there is no strong adhesion of the chip. For H13A coating TiN in cutting speed range (600/800 m/min). There was a strong adhesion of the chip with the cutting face which generates a large friction. The high cutting speed facilitates the removal of the chip and reduces adhesion. The cutting force is reduced.

4. Conclusion

Preliminary conclusion that can be given are:

At very high-speed machining of titanium alloy is possible. The detachment of the chip causes it to migrate carbide grains.

The goal of this work was to propose a detailed analysis of geometry of the chip alloy Ti–6Al–4 V.

The originality of this approach lies in the speed range explored varying between 600 and 1200 m/min that corresponds for carbide tools to the field of high speed (500 m/min) and very high speed (upper 600 m/min). This analysis helps to and proposes a hypothesis of their generation during high-speed machining. The ability to save snapshots of the cut in progress has complemented the postmortem micrographic analysis of chips and strengthens the hypotheses.

Almost instantaneous increase temperature in the cutting area of the chip causes the welding of the titanium alloy. The detachment of the chip causes it to migrate carbide grains.

In speed machining wear crater is the dominant wear on rake face and the final result is collapse in cutting edge.

Microgeometry analysis of cutting edges is very important in the understanding of the chip removal process. The interactions between the tool parameters, cutting parameters and the effects on the machining procedure are all influenced and therefore determined by the peak microgeometry. The evolution of the topography of crater wear using a confocal laser scanning microscopy is a valuable tool for crater imaging. It provides more details than conventional profilometers.

The chip formation of Ti-6Al-4 V alloy section is strongly influenced by crack initiation and propagation, resulting in discontinuous or fragmentary morphology. When machining Ti-6Al-4 V alloy at low cutting speed, the resulting chip is discontinuous, while at high cutting speed, chip is serrated.

Adhesion of the workpiece material occurs during titanium alloy machining, forming a BUE along the cutting edge. This BUE modifies the geometry of cutting edge and, consequently, the cutting forces. A better understanding of the relationship between cutting forces and both the shape and the size of the BUE must be realized in the future. It might be interesting to carry out tests with higher feed rates (by example 0.2 mm^{-1}). In terms of chip formation we notice adiabatic shear even at the lowest cutting speeds. This phenomenon is typical of titanium alloys.

To reduce wear, we must develop a system of lubrication located using the MQL technique.

Find a hard coating that will oppose the chip welding titanium alloy with the substrate of the insert. Why you should test other types of diamond coating for example.

Develop cryogenic lubrication to prevent heating in the cutting area.

Author details

Mohieddine Benghersallah[1]*, Lakhdar Boulanouar[1], Gautier List[2] and Guy Sutter[2]

*Address all correspondence to: bengher_moh@yahoo.fr

1 Research Laboratory in Advanced Technology and Mechanical Production, Department of Mechanical Engineering, Badji Mokhtar Annaba University, Annaba, Algeria

2 LEM3, UMR 7239, Université de Lorraine – Ile du Saulcy, Metz Cedex, France

References

[1] Boyer RR. An overview on the use of titanium in the aerospace industry. Materials Science and Engineering. 1996;**213A**:103-114

[2] Ezugwu EO, Wang ZM. Titanium alloys and their machinability, a review. Journal of Materials Processing Technology. 1997;**68**:262-274

[3] Nouari M, Makich H. Experimental investigation on the effect of the material microstructure on tool wear when machining hard titanium alloys: Ti–6Al–4V and Ti-555. International Journal of Refractory Metals and Hard Materials. 2013:259-269

[4] Ozel T, Ulutan D. Prediction of machining induced residual stresses in turning of titanium and nickel based alloys with experiments and finite element simulations. CIRP Annals-Manufacturing Technology. 2012;**61**:547-550

[5] Sutter G, List G. Very high speed cutting of Ti–6Al–4V titanium alloy – Change in morphology and mechanism of chip formation. International Journal of Machine Tools & Manufacture. 2013;**66**:37-43

[6] Nouari M, Calamaz M, Girot F. Mécanismes d'usure des outils coupants en usinage à sec de l'alliage de titane aéronautique Ti–6Al–4V. Comptes Rendus Mecanique. 2008;**336**: 772-781

[7] Olortegui-Yume JA, Kwon PY. Crater wear evolution in multilayer coated carbides during machining using confocal microscopy. Journal of Manufacturing Processes. 2007;**9**(1):107-110

[8] Liu Z, An Q, Xu J, Han MCS. Wear performance of (AlTiN)/(Si3N4) coating and (AlCrN)/(Si3N4) coating in high-speed machining of titanium alloys under dry and minimum quantity lubrication (MQL) conditions. Wear. 2013;**305**:249-259

[9] Zuo JH, Wang ZG, Han EH. Effect of microstructure on ultra-high cycle fatigue behavior of Ti–6Al–4V. Master Science Engineering A. 2008;**473**:147-152

[10] Sharman ARC, Aspinwall DK, Dewes RC, Bowen P. Work piece surface integrity considerations when finish turning gamma titanium aluminide. Wear. 2001;**249**:473

[11] Niu W, Berminghama MJ, Baburamani PS, Palanisamy S, Dargusch MS, Turk S, Grigson B, Sharp PK. The effect of cutting speed and heat treatment on the fatigue life of Grade 5 and Grade 23Ti–6Al–4V alloys. Materials & Design; April 2013;**46**:640-644

[12] Sharif S, Rahim EA. Performance of coated- and uncoated-carbide tools when drilling titanium alloy—Ti– 6Al4V. Journal of Materials Processing Technology. 2007;**185**:72-76

[13] Mathia T, Zahouani H, Rousseau J, Le Bosse JC. Functional significance of different techniques for surface morphology measurements. International Journal of Machine Tools and Manufacture. 1995;**35**:195-202

[14] Corle T, Kino G. Confocal Scanning Optical Microscopy and Related Imaging Systems. San Diego: Academic Press; 1996

[15] Bennett JM. Overview: Sensitive techniques for surface measurement and characterization. In: Proceedings of SPIE 1573. 1991. pp. 152-158

[16] Hamilton DK, Wilson T. Surface profile measurement using the confocal microscope. Journal of Applied Physics. 1982;**53**:5320-5322

[17] Devillez A, Lesko S, Mozer W. Cutting tool crater wear measurement with white light interferometry. Wear. 2004;**256**:56-65

[18] Dawson TG, Kurfess TR. Quantification of tool wear using white light interferometry and three-dimensional computational metrology. International Journal of Machine Tools and Manufacture. 2005;**45**:591-596

[19] HK T, Denkena B. Basics of Cutting and Abrasive Processes. Berlin: Springer; 2013

[20] Lichtman J. la microscopie confocale pour la science. octobre 1994. p. 204

[21] Zhu D, Xiaoming Z, Ding H. Tool wear characteristics in machining of nickel-based superalloys. International Journal of Machine Tools & Manufacture. 2013;**64**:60-77

[22] Sun S, Brandt M, Dargusch MS. Characteristics of cutting forces and chip formation in machining of titanium alloys. International Journal of Machine Tools & Manufacture. 2009;**49**:561-568

[23] Mathia TG, Pawlusb P, Wieczorowskic M. Recent trends in surface metrology. Wear. 2011;**271**:494-508

[24] Bassett E, Köhler J, Denkena B. On the honed cutting edge and its side effects during orthogonal turning operations of AISI1045 with coated WC-co inserts. CIRP Journal of Manufacturing Science and Technology. 2012;**5**:108-126

[25] Winogrodzka A, Valefi M, de Rooij MB, Schipper DJ. Measurement of chemical and geometrical surface changes in a wear track by a confocal height sensor and confocal Raman spectroscopy. Archives of Civil And Mechanical Engineering. 2014;**14**:1-5

[26] Denkena B, Biermann D. Cutting edge geometries. CIRP Annals-Manufacturing Technology. 2014;**63**:631-653

[27] Al-Zkeri I, Rech J, Altan T, Hamdi H, Valiorgue F. Optimization of the cutting edge geometry of coated carbide tools in dry turning of steels using a finite element analysis. Machining Science and Technology. 2009;**13**(1):36-51

[28] Revue sandvik coromant. Trametal-Janvier/Fevrier. 2010. p. 134

[29] Wong T, Kim W, Know P. Experimental support for a model-based prediction of tool wear. Wear. October 2004;**257**(7-8):790-798

[30] Olortegui-Yume JA, Kwon PY. Tool wear mechanisms in machining. International Journal of Machining and Machinability of Materials. 2007. Inderscience

Chapter 6

Laser Welding of Different Dental Alloys

Lavinia Cosmina Ardelean, Lucien Reclaru,
Cristina Maria Bortun and Brandusa Ghiban

Additional information is available at the end of the chapter

http://dx.doi.org/10.5772/intechopen.76347

Abstract

Laser welding permits joining various types of pieces, made of similar or different alloys, as titanium-based alloys, CoCr alloys, and even AuPd alloys. Laser welding is best suited to weld titanium alloys because they have higher rates of laser beam absorption and lower thermal conductivity compared to other dental casting alloys. Compared to micro pulse welding, laser welding is superior, obtaining the welding cord being faster and easier. The success of the welding procedure depends on the operator's dexterity and the choice of the welding parameters. Selecting the best combination of pulse energy, pulse duration, and peak power for each welding step is decisive.

Keywords: laser welding, micro pulse welding, dental alloys, welding assessment, welding cord

1. Introduction

Welding in dentistry involves small metallic areas, often in the proximity of resin or ceramic structures, which may be damaged by heat (**Figure 1**). The fracture of a metallic frame usually happens in an area of minimum resistance. This type of damage could not be repaired 15–20 years ago, using welding systems available at that time.

Nowadays, two types of welding are suitable for use in dental technique: laser and micro pulse [1].

After Nd:YAG lasers appeared in Europe, in 1990, laser welding has been extended to dental technique and permits joining various types of pieces, which might have been difficult or even impossible to do with other techniques.

Figure 1. Laser welding of a fractured clasp and frame.

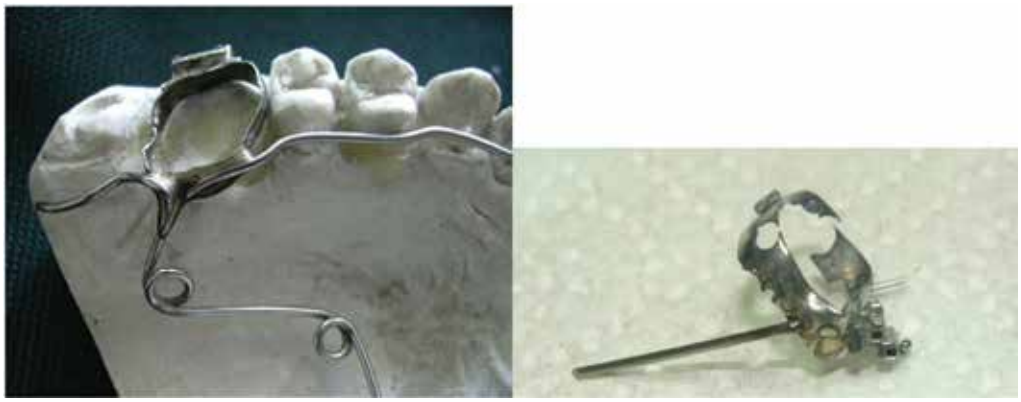

Figure 2. Welded CrNi stainless steel orthodontic ring and wire.

It permits joining similar or different alloys, as titanium-based alloys, CoCr alloys, and even AuPd or CrNi stainless steel alloys (**Figure 2**).

In laser welding, heating and melting are limited to a small area, which prevents damaging the components of the denture pieces which might deteriorate when heated (resins, ceramics) (**Figure 3**). It permits the welding of elements situated in places difficult to reach, such as the inner parts or extremely small, delicate, and sensible elements. It is very efficient in repairing the framework of removable partial dentures, being fast, economic, and very accurate [2].

It may also be used for manufacturing removable partial dentures, by joining pieces which might be difficult to cast in one piece, due to various reasons, such as high contraction at casting. One of the main advantages of the method is that of "cold" welding, on a model or even in hand. Nowadays even "in-mouth welding" is possible [3].

All laser welding devices used in dental technique are equipped with an optic enlarging system which permits perfect visualization of the fragments to be welded (**Figure 4**), the space between them, and the position of the filler metal, when used. The filler metal (special wire for laser welding) is the same type as the base material and has to be used when there is some space between the two pieces to be welded. Welding without a filler material may be carried out when the distance between the two pieces to be welded is almost imperceptible [4].

http://dx.doi.org/10.5772/intechopen.76347

Figure 3. Welding of a fractured clasp in close proximity to the saddle made of an acrylic resin.

Figure 4. XXS laser welder for dentistry (Orotig) and its enlargement system.

Laser welding in dental technique often uses a protected environment, argon 4.6 with a purity of 99.996% or argon 5.0 with a purity of 99.999%, in order to prevent the oxidation of the alloys [4].

Laser welding may be done in continuous or pulsed mode. The parameters which may be modified in case of welding with a Nd:YAG laser, in a continuous emission mode, are the radiation power, the welding speed, and the diameter of the laser beam. The radiation power variation is limited by the manufacturer and does not have a great influence on the welding depth. The diameter variation of the laser beam is also limited, in order to obtain the minimum density of the energetic wave; consequently, the only parameter which may significantly influence the morphology of the welding is the welding speed. A low welding speed does not necessarily imply a greater welding depth. In case of noble alloys, optimal welding speed is considered to be 10.1 cm/min, and it doubles in the case of base metal alloys: 20–25 cm/min. These parameters permit a welding depth of 0.8 mm for noble alloys and up to 2.0 mm for base metal alloys. Variations by 20% of these parameters may lead to incomplete welding (too high speed) or uncontrolled melting, which may compromise the entire piece [4].

In case of Nd:YAG laser welding pulsed mode, the density of the energetic flux is at least 10 billion times greater than when using the continuous mode. The exposure time is very short, so the thermal conductivity of the alloy is of less importance. In this case, the morphology of

the welding is influenced by the impulse energy, length, and frequency. In case of high energy density, the side effects which appear in the welded structure may not be generalized [4].

The action of the laser beam that leads to the formation of the welding cord can be described as follows (**Figure 5**):

- The material is first heated by conduction.
- The absorbed energy superficially penetrates the alloy, melting the impact surface.
- A metallic vapor develops in the center of the impact point. The material partly absorbs and diffuses the energy of the beam.
- The vapor pressure increases and dispels the melting alloy to the periphery of the beam and upward. This results in creating a narrow (capillary) shaft which propagates through the material. This shaft, with a diameter barely greater than the beam, is physically filled by metallic vapor plasma. Its walls are coated with a film of melting metal maintained by capillarity.
- The melting metal is finally sent backward and closes the welding cord (**Figure 6**) [5, 6].

The quality of micro pulse welding is comparable to that of laser welding. It has the advantage of a lower initial investment, but it uses electrodes that are consumed in time and have to be replaced. When compared to laser welding, micro pulse welding appears to be more visible and embossed (**Figures 7** and **8**). The probability of developing pores is higher, compared to laser welding, which is much more compact [7].

Welding in dental laboratories is made by melting small surfaces of the metallic piece. Each time, a welding cord with overlapped spots will be obtained (**Figure 6**). The area in close proximity, named thermally affected area (TAA), is very sensitive to thermal variations after welding, as sudden cooling of the material, which might lead to cracks. The TAA is usually tougher than the base material (BAA), from which the welded piece is manufactured.

The quality of the welding depends on the alloy's nature, the welding mode, and the laser's parameters [4].

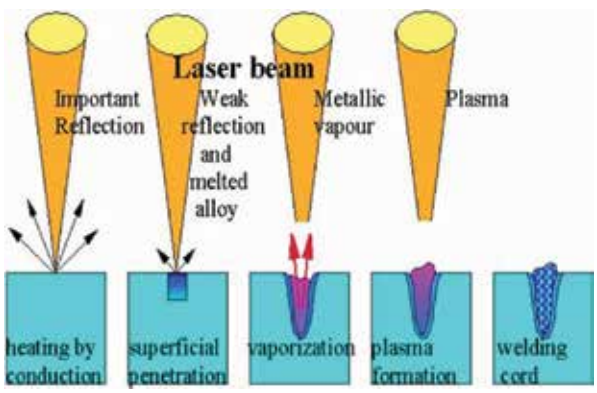

Figure 5. Stages of the welding cord formation.

Figure 6. (a) Image of the welding cord. (b) Microscopic image of the welding points.

Figure 7. Micro pulse welded piece.

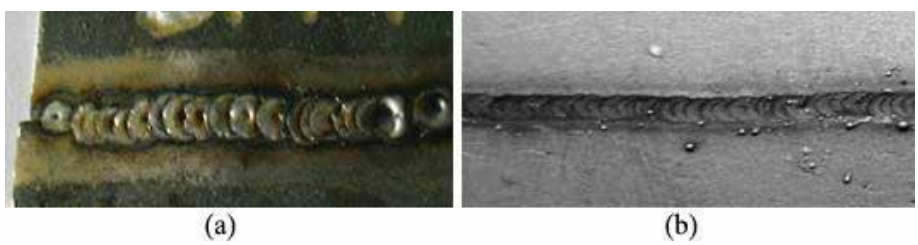

Figure 8. Appearance of micro pulse welding (a) compared to laser welding (b).

The quality of laser welded joints for different dental alloys may be evaluated by different invasive methods, metallographic analyses and microhardness testing, and noninvasive methods, dye staining, X-ray, and microscopy [8, 9].

2. Welding of TA6V4 and AuPd alloys

The TA6V4 alloy is a titanium-based alloy containing 6% aluminum and 4% vanadium, mainly used in manufacturing ready-made pieces for implantology.

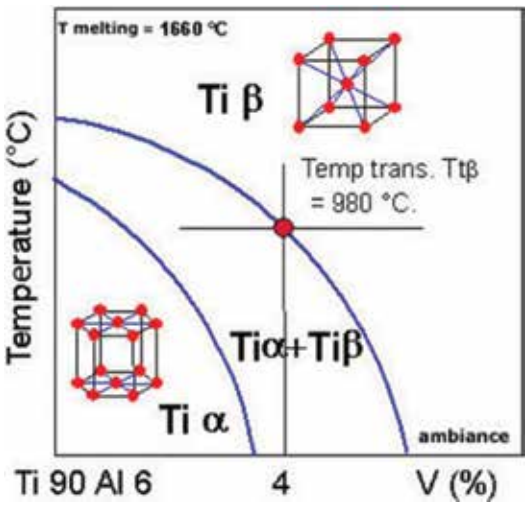

Figure 9. Schematic pseudo-binary phase diagram of TA6V4 alloy.

The alloy is biphased Tiα + Tiβ, at room temperature, with a slight phase percentage for Tiβ, as shown in the pseudo-binary phase diagram (**Figure 9**). The existence of the two phases Tiα and Tiβ, at room temperature, enables creating an alloy with a high mechanical resistance, due to the mutual interaction of the two phases. The alloy has an elasticity limit of 875 MPa.

During heating, the Tiα turns into Tiβ at approximately 980°C. During fast cooling, the Tiβ phase undergoes a so-called martensitic transformation forming a complex lamellar structure inducing significantly altered mechanical properties. These mechanical properties will be recovered by a low-temperature thermal treatment.

This alloy welds mainly to itself or to other alloys by laser welding. Metallurgic analysis, by metallography and scanning electron microscope (SEM) observation, after a single impulse

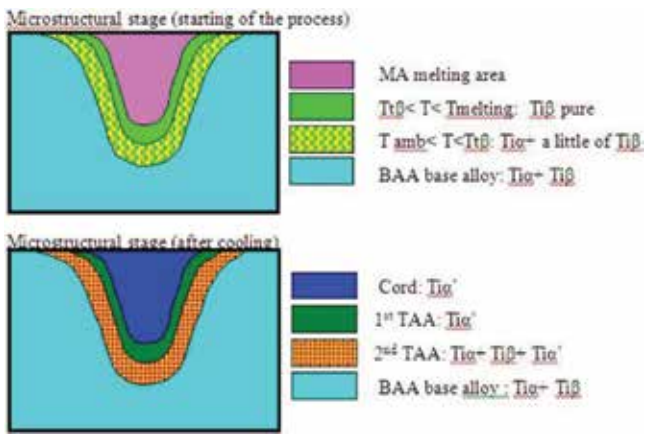

Figure 10. Schematic description of the cord during welding.

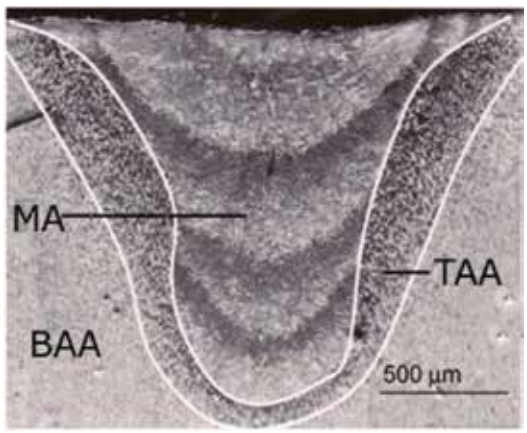

Figure 11. SEM observation of the TA6V4 cord sample after a single impulse laser impact.

laser impact, of the sample is characterized (**Figures 10** and **11**) in the following way: after cooling, there is a melting area (MA), a thermally affected area (TAA), and an area corresponding to the base alloy (BAA) [10].

- The MA is mainly formed of Tiα turned by martensitic transformation into Tiα'.
- The TAA is mainly composed of two sublayers developed in the proximity of MA, formed of a Ti" structure and, deeper down, of a complex Tiα + Tiα + Tiα' structure.
- The BAA consists of the Tiα + Tiβ structure.

The AuPd alloy welded by laser technique is the standard Qualibond 2 (PX Dental/Qualident) alloy for the metallo-ceramic technique, containing 51.2% Au, 38.6% Pd, indium, gallium, and ruthenium as additional elements.

For the AuPd alloy for the metallo-ceramic technique, **Figure 12** shows the successive impacts leading to the welding of the two pieces. Like in the case of a titanium-based alloy, there is a very perturbed TAA (**Figure 13**) and a lamellar structure of the MA (**Figure 14**).

In case of TA6V4 alloy, the cooling speed plays an important role on the mechanical characteristics due to its influence on the phase transformation structures into a solid state. The elasticity limit during high temperatures decreases, and the resistance to wear is rather unaffected by laser welding due to the fact that the cord has no porosities or other defects (cracks, snaps) [11].

In case of the AuPd alloy for the metallo-ceramic technique, it appears the fracture toughness of the laser welded area is higher than in the case of brazing. On the other hand, the wear resistance of the laser welding is lower than in the case of brazing (**Figure 15**).

The quality of the welding is mechanically satisfactory. In order to avoid problems, initially, both parts of the joined piece should be subjected to low-level energy impacts, followed by greater energy for filling. The success of the welding procedure also depends on the operator's dexterity and the choice of the welding parameters [12].

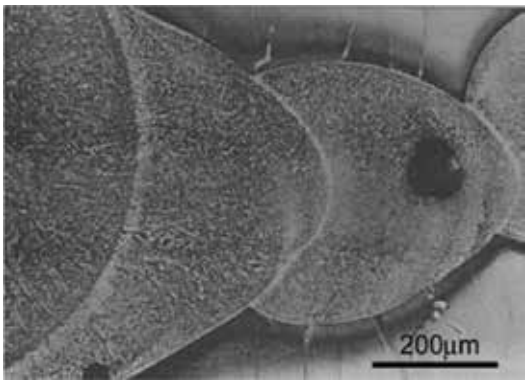

Figure 12. Welded area (SEM).

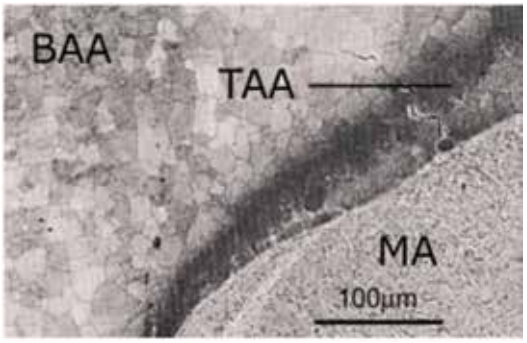

Figure 13. MA, TAA, BAA areas (metallography).

Figure 14. MA area (metallography).

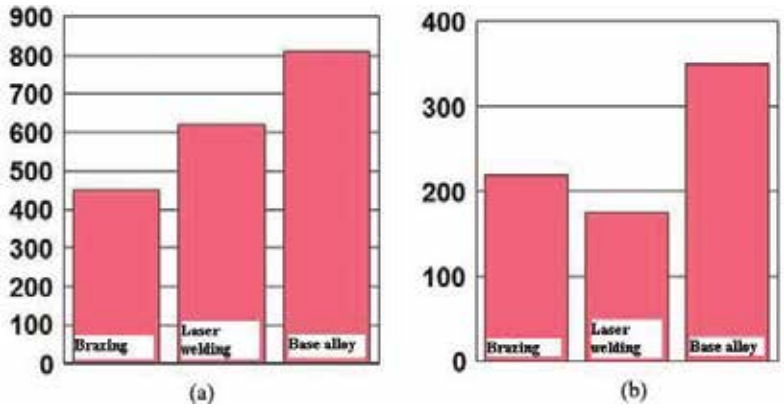

Figure 15. (a) Fracture toughness (MPa). (b) Resistance to wear (MPa).

3. Welding of three different CoCr alloys

Three different CoCr alloys, frequently used for manufacturing metallic frameworks of removable partial dentures, were tested: Heraenium CE (Heraeus Kulzer), Wironit Extra-Hard (Bego), and "C" alloy (Vaskut Kohàszati Kft). The chemical composition and mechanical properties of the alloys are shown in **Table 1**.

The alloys were analyzed both in the form of metallic frameworks of removable partial dentures (**Figure 16**) and as metallic casted plates with dimensions 10x20mm and thickness of 0.4 mm (**Figure 17**). For improving the structure of the alloy plates, heat treatments at different temperatures were applied.

In some cases, the use of a filler metal, special 0.5 mm diameter CoCr Finalloy filler (Fino), was needed (**Figures 18** and **19**).

The equipment used for welding consisted of Welder micro pulse (Schütz Dental) and Laser 65 L-Titec (**Figure 20**).

Welded joint quality was tested by radiographic, microscopic, metallographic, and microhardness tests [13].

In order to assess the quality of the welded joints and visualize possible structural defects as cracks in the base materials, X-rays and microhardness tests were carried out. The inverted

Tested alloys	Co	Cr	Mo	Si	Mn	*C*	Tensile strength R_m	Vickers hardness
Heraenium CE	63.5	27.8	6.6	1.0	0.6	—	890 N/mm^2	380 HV
Wironit Extra-Hard	63.0	30.0	5.0	1.0	1.0	<1.0	910 N/mm^2	385 HV
"C" alloy	65.0	29.0	5.0	0.35	5.0	0.4	760 N/mm^2	380 HV

Table 1. The chemical composition and mechanical properties of the three alloys.

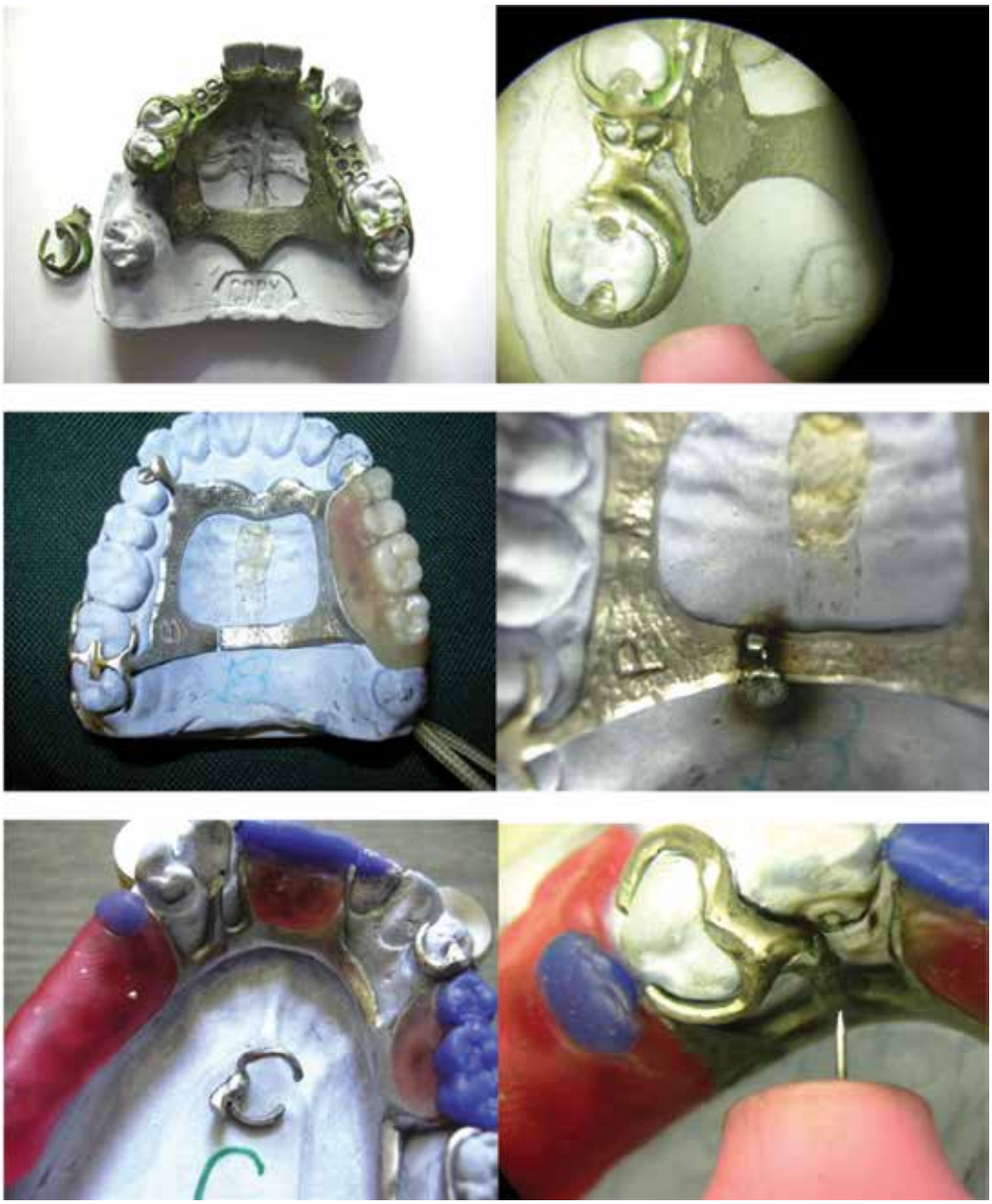

Figure 16. Some fractured metallic frameworks of removable partial dentures, before and after welding.

metallurgical microscope and the stereomicroscope enabled the observation of different processing aspects of the metallic components, relevant for the welding procedure.

Microhardness analysis was carried out using a 100 g charge, five to six impressions for each area of the welded joint being made, and shows a small increase of the hardness in TAA and

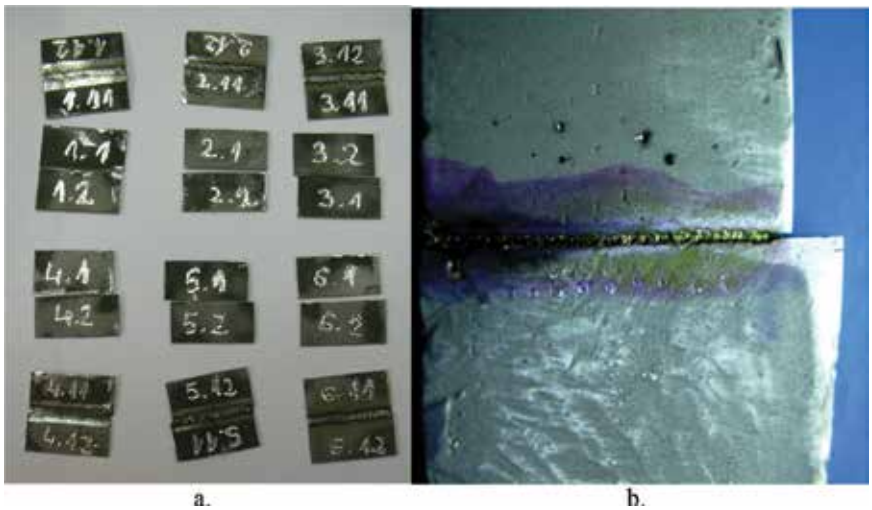

Figure 17. (a) The casted plates. (b) Plates after welding.

MA. The hardness in the MA shows values between those of the BAA and TAA. Microhardness values of the welded joints are up to 15% lower in the TAA for Wironit Extra-Hard (Bego), with no heat treatment, and higher up to 16% if heat treatment was made.

In case of Heraenium CE (Heraeus Kulzer) microhardness, part of the samples without heat treatment shows no changes in the MA and TAA; part of the samples shows decreased values up to 25%. Samples which had undergone heat treatment show no changes.

In case of "C" alloy (Vaskut Kohàszati Kft), part of the samples shows no microhardness changes; part of the samples shows decreased values up to 33%.

These values are of no great importance as microhardness variations may appear due to lack of homogeneity of the casted base alloy [14].

X-rays show casting defects, such as lack of material and cracks within the base material (BAA). A radiotransparency on the welding line and some imperfections in the clasps welding area may be observed (**Figure 21**).

For the "C" alloy (Vaskut Kohàszati Kft), the welding area, dyed in yellow, shows no fissures in the immediate vicinity of the welding, in the TAA, because the laser was used at very low temperatures and there are no contractions in the analyzed material. However, X-rays show radiotransparency in the MA, which indicates a superficial fusion which does not cover the entire thickness of the plate. (**Figure 22**) Despite the fact that the plates used are not very thick, welding does not cover the whole depth. This results in the fragility of the welding [11, 13].

Microstructural analysis presents the relative homogeneous dendritic structure specific for casted alloys, nonmetallic inclusions, and some chemical compounds. Intergranular precipitations and spherical shape compounds, consisting of alloy's elements, placed inside

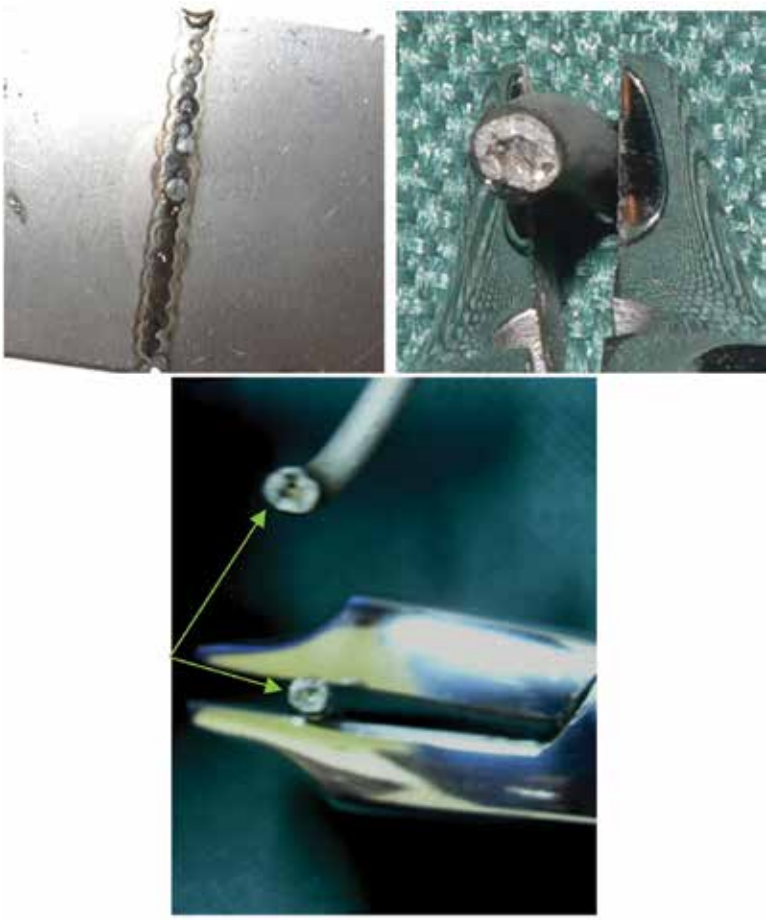

Figure 18. Laser welding without filler metal.

Figure 19. Laser welding with filler metal.

http://dx.doi.org/10.5772/intechopen.76347

Figure 20. The micro pulse welding device Welder (Schütz dental) and laser 65 L-Titec with welding parameters.

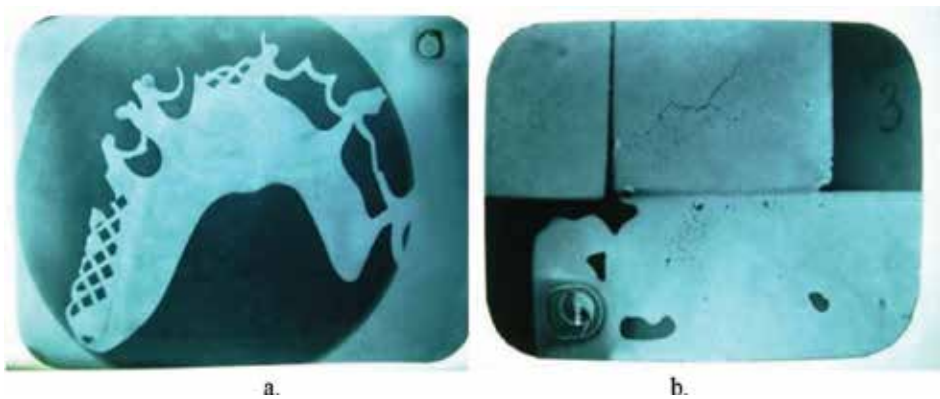

Figure 21. Radiographic images: (a) Metallic framework. (b) Welded plates.

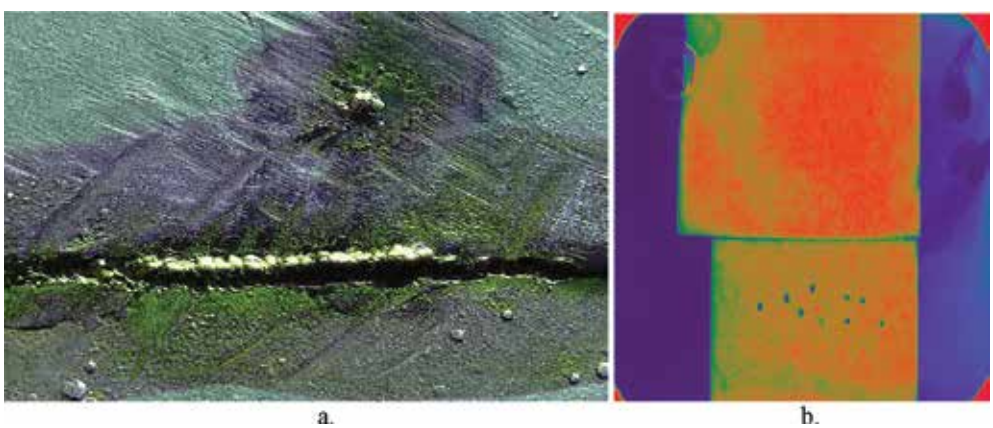

Figure 22. Assessment of the welded "C" alloy (Vaskut Kohàszati Kft) area: (a) Basic fuchsin dye staining. (b) X-ray pseudo-chromatization.

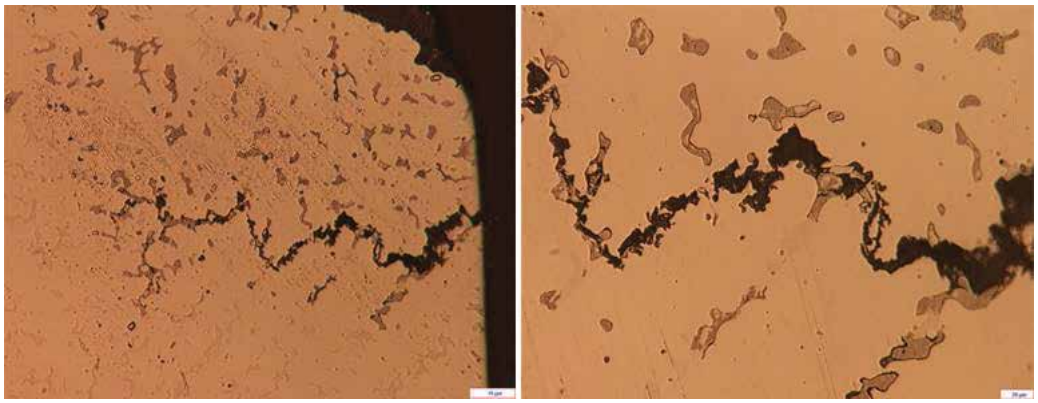

Figure 23. Microcracks in the BAA dendritic structure spread along the fragile compound precipitations, in case of fast cooling of the welded alloy.

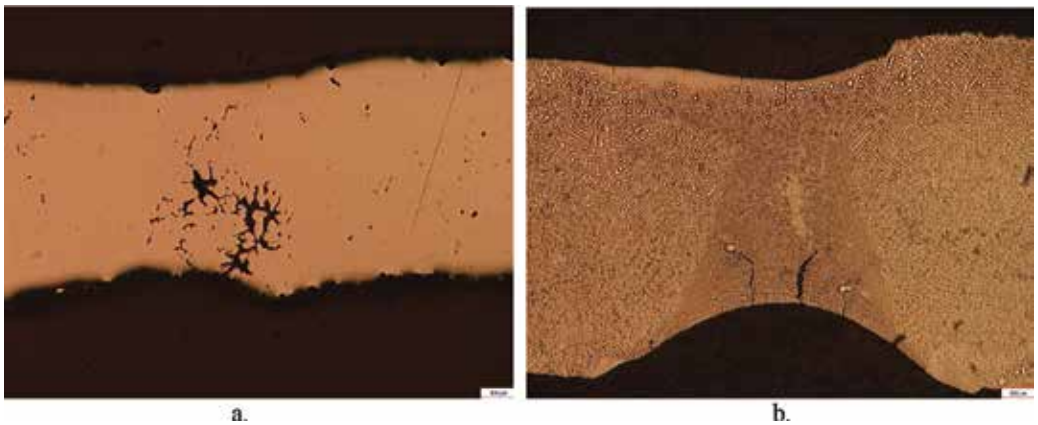

Figure 24. (a) Nonuniform dendritic structure with interdendritic cracks and microporosities. (b) Microstructural aspect of the welding cord in case of "C" alloy (Vaskut Kohàszati Kft), with cracks due to laser exposure, spreading from surface to center.

the crystalline grains with well-delimitated boundary limits, which are characteristic to the solidification process, appear in case of some welded joints (**Figures 23**, **24**, and **25**). This may often lead to alloy durification and fragile structure.

Metallographic analysis of the laser welded joints is shown in **Figures 26**, **27**, and **28**.

Figure 29 shows pellicular intergrain precipitations and spherical shape compounds, placed inside the crystalline grains.

Metallographic analysis indicates that welded CoCr alloys exhibit rather large microstructural defects, including interdendritic carbide precipitations, segregation, relatively large grains, and porosity, mainly in the BAA area. These microstructural defects may lead to crack initiation. The welded joints themselves (MA) show a rather good quality.

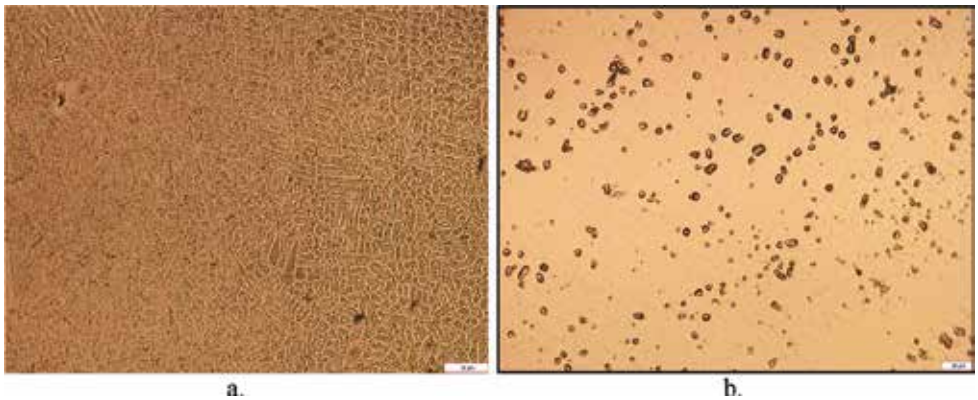

Figure 25. Wironit extra-hard (Bego) sample. (a) Welded on both sides, with nonuniform dendritic structure. (b) With thermal treatment, with nonuniform fine dendritic structure and carbide inclusions.

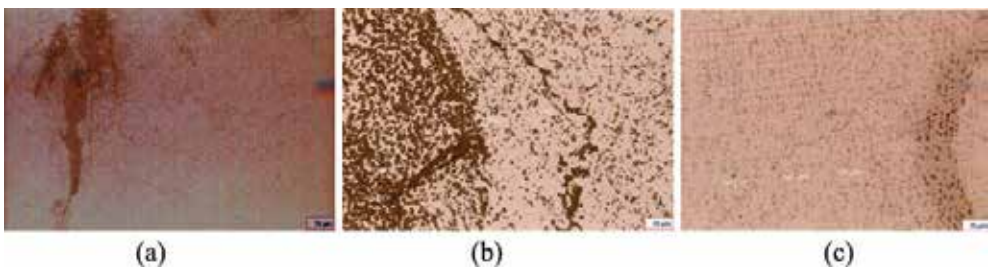

Figure 26. Microstructural aspect of Heraenium CE (Heraeus Kulzer). (a) Laser welded samples MA and TAA, microhardness values unchanged. (b) Laser welded samples without thermic treatment, MA microhardness values decreased up to 25%. (c) Micro pulse welded samples, heat treated, no microhardness changes in the TAA.

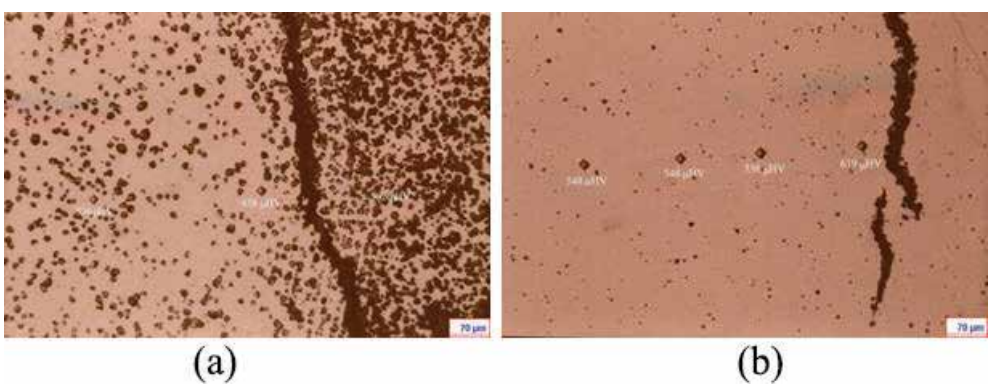

Figure 27. Microstructural aspect of Wironit extra-hard (Bego) laser welded samples. (a) TAA microhardness values lower up to 15%. (b) Samples with heat treatment, TAA microhardness values higher up to 16%.

Noninvasive analysis points out the structural defects of the three casted alloys, showing cracks which grow proportionally with the thickness of the alloy, within the BAA. These may be caused by casting, improper processing, and rapid cooling after welding [15, 16].

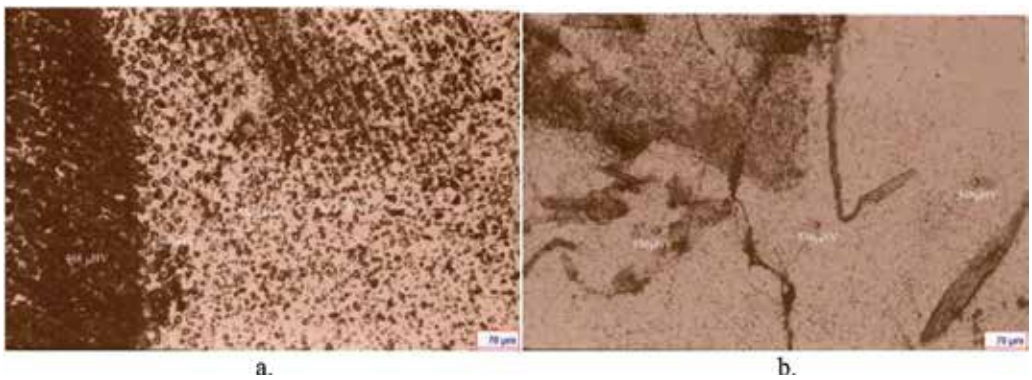

Figure 28. Microstructural aspect of "C" alloy (Vaskut Kohàszati Kft) laser welded samples. (a) TAA microhardness values lower up to 30%. (b) TAA microhardness values unchanged.

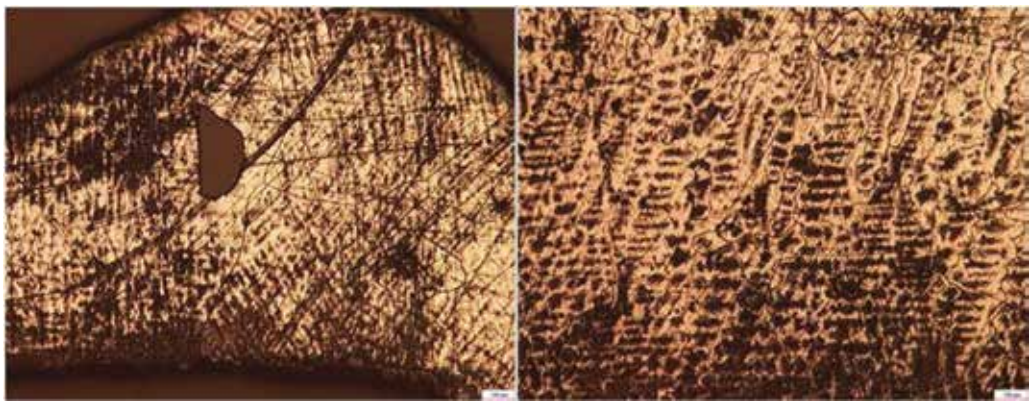

Figure 29. Metallographic aspects of pellicular intergrain precipitations, spherical shape compounds.

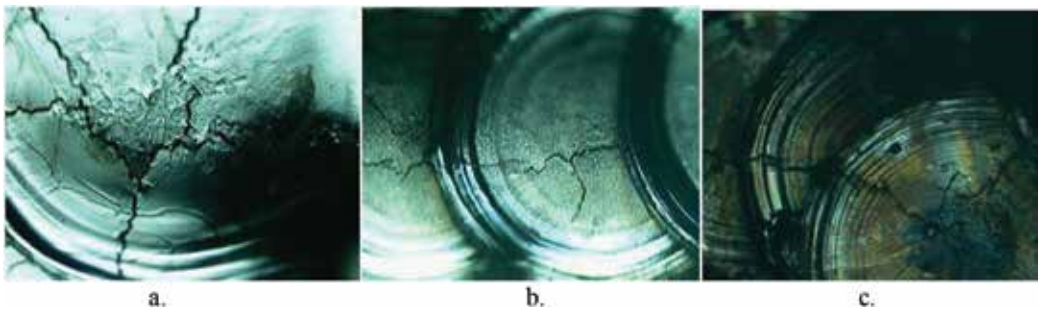

Figure 30. Microscopic aspects of Wironit extra-hard (Bego) alloy for different laser beam sizes: (a) small, (b) medium, (c) large.

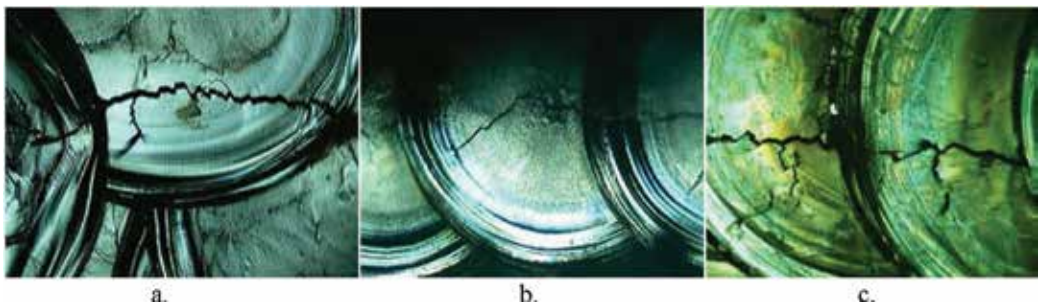

Figure 31. Microscopic aspects of "C" alloy (Vaskut Kohàszati Kft) for different laser beam sizes: (a) small, (b) medium, (c) large.

The welding defects (cracks) appear to be in connection with the laser beam size and laser power. Most of the cracks appear at big spot/ high power association, during the welding smoothing (**Figures 30** and **31**) [17].

4. Welding complex CoCrMoTi(Zr) alloys

Welding experiments on complex CoCrMoTi(Zr) alloys, CoCrMoZrTi alloy, CoCrMoTi4 alloy, and CoCrMoTi5.5 alloy [18–24], were performed by selecting three categories of parameters, a selection which was made following previous tests on cobalt alloys. For this purpose, the welding parameters were chosen, with three values of the laser spot power, namely, low power (1.9 W), average power (2.0 W), and higher power (2.3 W); the times of application of the spot, namely, short (1.1 s) or long (1.3 s); and the frequency of the spot application at two levels, respectively, 2.0 Hz and 3.0 Hz. (**Table 2**).

The macrostructural analysis carried out on the welded surfaces of the complex CoCrMoTi(Zr) alloys is shown in **Figures 32–34**. This analysis proved to be decisive in the selection of welding parameters as it allowed to highlight these parameters correlated with the macrostructural aspect. Thus, in the case of the first set of welding parameter values, all alloys presented similar macrostructural aspects, consisting of non-cracked welded cords. The second set of values resulted in partially satisfactory results, with all alloys presenting a nonconforming welded surface. Regarding the third set of welding values, it led to the most inappropriate results. Thus, in all alloys, the high value of the welding spot power generated the subsequent melting of the welding cord, due to the generation of sprays from the next step. It can be said that the welding performed with

Parameter	Power	Time	Frequency
Set 1	2.0 W	1.1 s	2.0 Hz
Set 2	1.9 W	1.3 s	3.0 Hz
Set 3	2.3 W	1.3 s	2.0 Hz

Table 2. Sets of parameters used for welding CoCrMoTi(Zr) alloys.

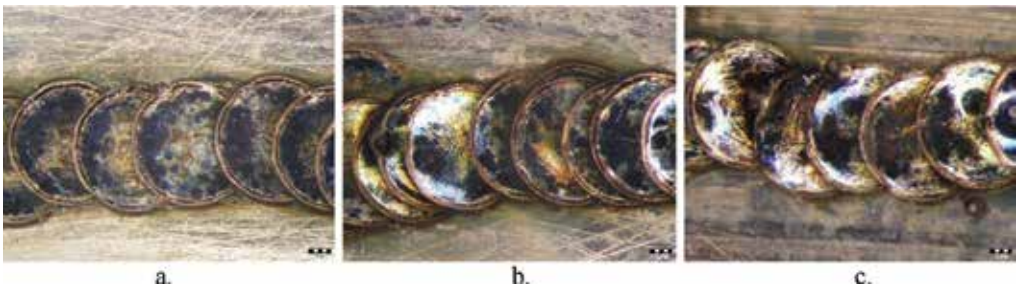

Figure 32. Macroscopic aspect of the welded CoCrMoZrTi alloy using different parameter values: (a) first set, (b) second set, (c) third set.

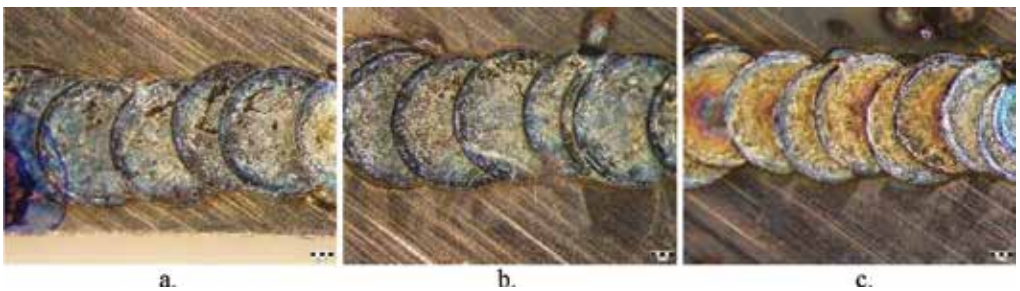

Figure 33. Macroscopic aspect of the welded CoCrMoTi4 alloy using different parameter values: (a) first set, (b) second set, (c) third set.

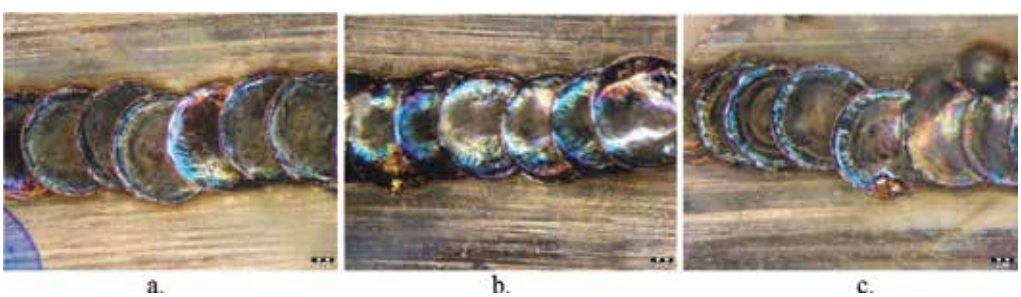

Figure 34. Macroscopic aspect of the welded CoCrMoT5.5 alloy using different parameter values: (a) first set, (b) second set, (c) third set.

the parameters corresponding to the first set of values generates the best quality welding cord, without the presence of cracks. The microstructural analysis (**Figures 35–37**) confirms the macrostructural one. In the case of the first set of welding parameters, no cracks were observed either in the welding cord or TAA in all alloys, irrespective of the thermal treatment state (**Figure 35a**, **36a**, and **37a**). In the case of the second set of values, the presence of cracks generated either on the welding cord and developed in the TAA (as for the CoCrMoZrTi alloy), or strong cracks in the center of the welding cord (CoCrMoTi4 alloy, CoCrMoTi5.5) are present. Similar observations were also recorded on

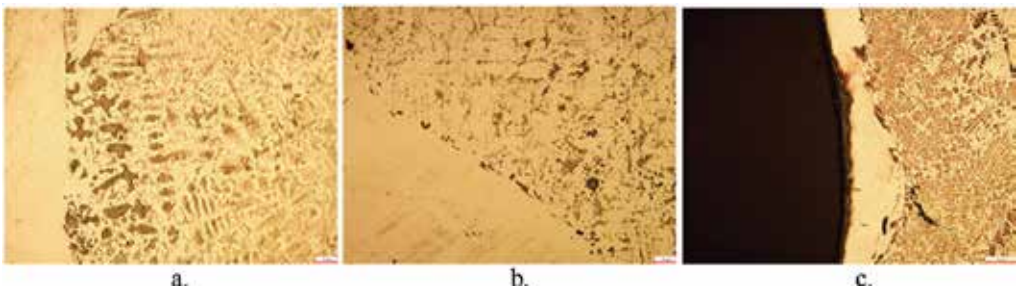

Figure 35. Microscopic aspect of the welded CoCrMoZrTi alloy using different parameter values: (a) first set, (b) second set, (c) third set.

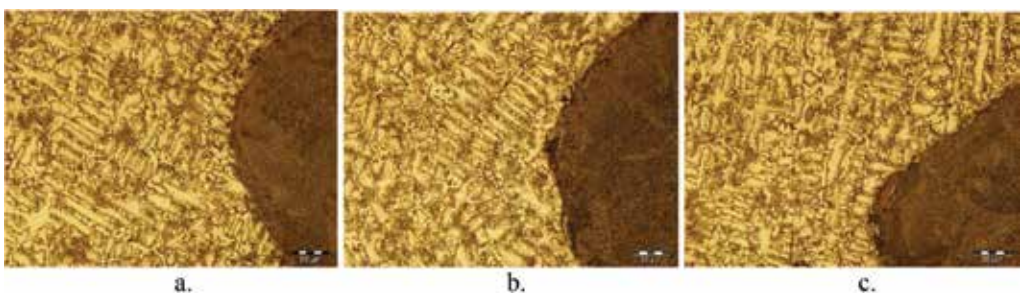

Figure 36. Microscopic aspect of the welded CoCrMoTi4 alloy using different parameter values: (a) first set, (b) second set, (c) third set.

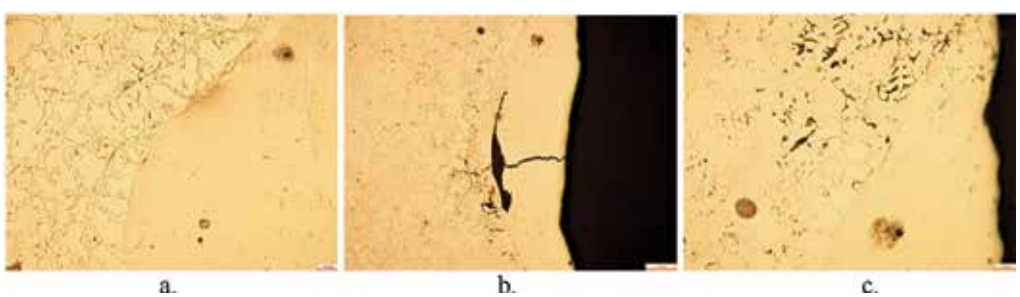

Figure 37. Microscopic aspect of the welded CoCrMoT5.5 alloy using different parameter values: (a) first set, (b) second set, (c) third set.

samples welded using the third set of parameters, the difference being the dimensions and the crack propagation. Thus, in the case of the third set of welding parameters, larger cracks with transgranular propagation may be noticed in almost all situations.

5. Discussions

Laser and micro pulse welding is mainly used in dentistry for repairing damaged metallic parts of partial dentures or orthodontic appliances [25].

If welding is used for repairing or completing damaged areas of prosthetic pieces, structural modifications are expected, especially in TAA, regardless of the welding type. In this area, due to overheating and fast cooling, precipitates of certain alloy chemical compounds may appear. These precipitates increase the hardness of the welded metal and lead to fragile areas, which could crack during functional loads. Cracks may appear not only because of the mechanical stress to which the dentures are exposed but also during manufacturing stages and may lead to fracture. Thermal treatments improve the structure and quality of the casted and welded alloys [4].

In order to obtain dentures with good resistance, it is very important to assess the quality and potential structural defects of the welded parts.

The success of the welding procedure depends on the operator's dexterity and the choice of the welding parameters. Selecting the best combination of pulse energy, pulse duration, and peak power for each welding step is decisive [20, 24].

Laser welding is best suitable to weld titanium and its alloys because they have higher rates of laser beam absorption and lower thermal conductivity compared to other dental casting alloys such as gold or CoCr alloys; however, due to the strong reactivity of molten titanium with oxygen in ambient air, the incorporation of oxygen during laser welding may affect the joint strength.

The initial welding is carried out by using a small laser beam (which better penetrates the alloy); afterward, a large beam is used for surface smoothening. Optional welding may be carried out in argon protective environment. The pulsed mode is preferred.

In the case of base metal alloys, the beam diameter must not be smaller than 1.5 mm, a 0.8 mm depth being considered enough to obtain a good breaking resistance. In case of heavy loads, both sides of the defect are welded.

Welding without filler metal is very scrupulous and implies a perfect surface processing and a uniform proximity of maximum 0.1 mm (which enables a good welding resistance), which is difficult to obtain in daily practice. Furthermore, the penetration depth and the metallographic changes in the TAA are difficult to manage. From this point of view, welding with filler metal is better, because the breaking resistance is reproducible, welding being carried out by conducting heat along the interfaces.

Welded alloys without carbon act better than those which have carbon in their composition. During welding, excess carbide precipitations may occur, which leads to hardening (fragilization) of the TAA and possible cracks.

In case of repairs, an important element is determining the initial cause of the fracture. If it's the consequence of a casting or conception mistake, the welding will not last for long.

With a proper selection of laser parameters for welding, one may obtain very good welded pieces, with no cracks (as showed in our experiments carried on CoCrMoTi(Zr) system alloys).

6. Conclusions

The advantages of laser welding in dental laboratories may be summarized as follows: it is time-saving; potentially all types of metals may be joined, particularly titanium alloys; welds are made on the model, distortions being avoided; the absence of corrosion, because no soldering alloy is needed; good resistance of the welded area; and the possibility to weld in proximity of resins or ceramic materials without damage.

Compared to micro pulse welding, which needs the use of a changeable electrode, laser welding is superior, achieving the welding cord being faster and easier in case of laser welding.

Author details

Lavinia Cosmina Ardelean[1]*, Lucien Reclaru[2], Cristina Maria Bortun[3] and Brandusa Ghiban[4]

*Address all correspondence to: lavinia_ardelean@umft.ro

1 Department of Technology of Materials and Devices in Dental Medicine, "Victor Babes" University of Medicine and Pharmacy, Timisoara, Romania

2 Consultant, Corrosion and Biocompatibility Department, VVSA, Branch of Richemont International SA Varinor Innovation, Switzerland

3 Department of Dentures Technology, "Victor Babes" University of Medicine and Pharmacy, Timisoara, Romania

4 Department of Metallic Materials Science, Physical Metallurgy, Faculty of Science and Engineering of Materials, "Politehnica" University of Bucharest, Romania

References

[1] Pop D, Negrutiu M, Sinescu C, et al. Different types of laser welding in dental technology. TMJ. 2007;**57**:184-186

[2] Ardelean L, Rusu LC. Materiale, instrumente si aparate in laboratorul de tehnica dentara. Timisoara: Eurostampa; 2013

[3] Fornaini C, Passaretti F, Villa E, Rocca JP, Merigo E, Vescovi P, Meleti M, Manfredi M, Nammour S. Intraoral laser welding: Ultrastructural and mechanical analysis to compare laboratory laser and dental laser. Lasers in Medical Science. 2011;**26**(4):415-420. DOI: 10.1007/s10103-010-0788-7

[4] Gaman S. Tehnologii de realizare, optimizare si reoptimizare a protezelor mobilizabile scheletate [thesis]. Timisoara: "Victor babes" University of Medicine and Pharmacy; 2011

[5] Reclaru L, Susz C, Ardelean L. Laser beam welding. TMJ. 2010;**60**(1):86-90

[6] Susz C, Reclaru L, Ardelean L, Ghiban B, Rusu L. Aliaje Dentare. Timisoara: Victor Babes; 2010

[7] Pop DM, Rominu M, Topala FI, Sinescu C, Dodenciu D, Rominu RO, Ardelean L, Rusu LC, Andoni M, Petrescu EL, Negrutiu ML. Laser weldings versus electrical weldings in dental technology. A a corrosion approach study. Revista de Chimie. 2011;**62**(12):1203-1205

[8] Ardelean L, Reclaru L, Bortun C, Rusu L. Assessment methods of different laser welded dental alloys. In: Katalinic B, editor. DAAAM International Scientific Book: DAAAM International Vienna. 2011. pp. 1047-1048

[9] Ardelean L, Reclaru L, Bortun CM, Rusu LC. Assessment of dental alloys by different methods. In: Mahmood Aliofkhazraei, editor. Superalloys: InTech; 2015. pp. 141-170. DOI: 10.5772/59358

[10] Ardelean L, Reclaru L, Bortun CM, Rusu LC. Investigations on Dental Alloys Using Metallographic Observation, Scanning Electron Microscopy, and Energy-Dispersive X-Ray Spectroscopy In: Stefan G. Stanciu, editor. Micro and Nanotechnologies for Biotechnology: InTech; 2016. p. 123-143. DOI: 10.5772/61530

[11] Ardelean L, Reclaru L, Bortun C, Rusu LC. Joint quality assessment of three laser welded dental alloys. Solid State Phenomena, Advanced Materials and Structures V. 2014;**216**:63-66

[12] Sandu L, Birdeanu V, Bortun C, et al. Laser welding optimizations for practical use in dental technology. TMJ. 2008;**58**(3-4):212-217

[13] Ardelean L, Bortun C, Sandu L. Non-destructive Defectoscopic tests on laser welding points in partial denture alloys. European Cells & Materials. 2005;**10**(Suppl. 1):15

[14] Bortun C, Mitelea I, Milos, Birdeanu V, Sandu L. Analysis of laser welded joints on "C" alloy in the removable partial dentures technology. European Cells & Materials 2005; **10**(Suppl. 1):31

[15] Ghiban B, Bortun C, Sandu L. Structural features in cobalt based alloys for dental applications. Bulletin of the Transilvania University of Brasov. 2007;**II**:80-86

[16] Bertrand C, Le Petitcorps Y, Albingre L, et al. The laser welding technique applied to non precious dental alloys procedure and results. British Dental Journal. 2001;**190**(5):255-257

[17] Bortun CM, Ghiban B, Ghiban G, Ardelean L, Rusu LC. Surface characterization of some CoCrMo alloys used in RPD technology. Revista de Chimie. 2012;**63**(9):906-910

[18] Ghiban B, Bortun CM. Aliaje dentare de cobalt. Structură, procesare, optimizare. Printech: Bucuresti; 2009

[19] Ghiban B, Ghiban N. Cobaltul şi aliajele de cobalt. In: Tratat de Stiinţa si Ingineria Materialelor Metalice. Vol. 3. Agir: Academia de Stiinţe Tehnice din Romania; 2009. pp. 960-970

[20] Ghiban A, Ghiban B, Bortun CM, Buzatu M. Structural investigations in CoCrMo(Ti) welded dental alloys. Revista de Chimie. 2014;**65**(11):1314-1318

[21] Peter I, Rosso M, Ioan D, Ghiban B, Castella C. Design and microstructure of innovative Cobalt base alloy, Materials Science Forum. Vol. 790-791. Trans Tech Publications Switzerland; 2014. pp. 235-240

[22] Bortun CM, Ghiban B, Ghiban A, Cernescu A, Ghiban N, Semenescu A. Comparative studies of tensile and bending behavior for some CoCrMo alloys. Metalurgia International. 2011;**16**(7):5-13

[23] Ardelean L, Reclaru L, Bortun CM, Ghiban B, Rusu LC. New aspects concerning co-Cr alloys. Metalurgia International. 2010;**15**(9):31-35

[24] Peter I, Rosso M, Toppi A, Dan I, Ghiban B. Investigation on cobalt based alloy modified by titanium for dental applications. Archives of Materials Science and Engineering. 2013;**61**(2):62-68

[25] Szuhanek C. Mechanical properties of welded orthodontic metal appliances. In: Katalinic B, editor. DAAAM International Scientific Book 2010. Vienna: DAAAM International; 2010. pp. 237-244

Edited by Sinem Cevik

In recent years, superalloys have been widespread usage in aerospace gas turbine engine parts. The main reason of it is that these materials have high yield, ultimate tensile strength, and very good corrosion/oxidation resistance, and they combine these good properties with an excellent creep resistance at elevated temperatures. In spite of their outstanding properties, superalloys can lose their mechanical strength because of wear, tear, and crack formation when they are exposed to high-service temperatures and heavy working conditions. Moreover, corrosion is another important issue for superalloys because the materials of gas turbine engine parts are exposed to harsh engine environments, which consist of many pollutants and hot gases. Therefore, special attention must be given to the corrosion behavior of superalloys.

This book provides information on the interaction between the microstructure of alloys and their mechanical properties and also the position of superalloys in the manufacturing industry. Topics cover the minimization of the formation of microsegregation and detrimental phases in the GTA welding of superalloys, oxidation kinetics of nickel-based superalloys used in the manufacture of rings for aircraft engines, a review of the work done over the last two decades to understand the hot corrosion behavior of superalloys used in advanced coal-based power plants, ultrasonic-assisted machining of Inconel 718, dry high-speed turning of Ti-6Al-4V titanium alloy, and laser welding in dentistry.

The book *"Superalloys for Industry Applications"* consists of contributions by scientists and engineers who are experienced in the production, design, and analysis of materials from all around the world. We hope that this book will be an irreplaceable source of study for manufacturing, degradation mechanisms, and reliability of superalloys.

Published in London, UK

IntechOpen

ISBN 978-1-83881-249-2